UNIVERSITY OF CALIFORNIA SAN DIEGO

Calculation and Modeling of Rigidity in Conjugated Polymers

A dissertation submitted in partial satisfaction of the
requirements for the degree
Doctor of Philosophy

in

Chemical Engineering

by

Andrew Thomas Kleinschmidt

Committee in charge:

    Professor Darren Lipomi, Chair
    Professor Tod Pascal, Co-Chair
    Professor Rommie Amaro
    Professor Michael Gilson
    Professor Nisarg Shah

2022

The dissertation of Andrew Thomas Kleinschmidt is approved, and it is acceptable in quality and form for publication on microfilm and electronically.

University of California San Diego

2022

DEDICATION

To:

To Mom and Dad. Your unwavering support made everything possible.

TABLE OF CONTENTS

LIST OF FIGURES

ACKNOWLEDGEMENTS

This work is the result of my graduate school efforts to become a computational chemist focusing on accurate modeling of conjugated polymers. I have great admiration and respect for my advisor, Prof. Darren Lipomi, who guided me tirelessly through my PhD. Despite struggles and great difficulty through the work, his support was unwavering. I hope the work accomplished here makes him proud, as I certainly am. My other advisor, Prof. Tod Pascal, was new to the department partway through my PhD, and I instantly knew I had to have him as a coadvisor. His depth of knowledge on a dizzying array of topics is staggering, and every time I meet with him I walked away more intelligent. So much of my success is due to these two titans of intellect. I would also like to thank the Lipomi Lab for the wonderful and vibrant community they have created over the past 6 years. I would particularly like to thank Laure Kayser and Charles Dhong, who helped create and foster simultaneous intellectual curiosity and emotional vivaciousness early on in the group. They always supported me early in my career, even when I was entirely unsure of my own abilities. I would additionally like to thank Alex Chen; if any sentence in Chapters 3, 4, and 5 make sense, it is his doing. I would like to thank Robert Ramji for his support in the final year of my graduate studies, and hope he gains as much joy from his research as I have. Finally, I would like to thank my family, who were a constant support and always by my side. I truly owe whatever I have been able to accomplish to the fact that I always have them behind me. Also, they had to watch me try to eat pudding while brain-damaged. That's love.

Chapter 1, in part, is a reprint of material submitted to be published in: **Kleinschmidt AT**, Pascal TA, Lipomi DJ. Computational Modeling of Molecular Materials for the Experimentally

ix

Inclined. *In Review*. The dissertation author was first author of this paper.

Chapter 2, in part, is a reprint of material as it appears in: Sugiyama F, **Kleinschmidt AT**, Kayser LV, Alkhadra MA, Wan JMH, Chiang ASC, Rodriquez D, Root SE, Savagatrup S, Lipomi DJ. Stretchable and Degradable Semiconducting Block Copolymers. Macromolecules 51, 5944-5949, doi:10.1021/acs.macromol.8b00846 (2018). The dissertation author was second author of this paper.

Chapter 3, in full, is a reprint of material submitted to be published in: **Kleinschmidt AT**, Chen AX, Pascal TA, Lipomi DJ. Decoupling Planarizing and Steric Energetics to Accurately Model the Rigidity of π-Conjugated Polymers. *In Review*. The dissertation author was first author of this paper.

Chapter 4, in full, is a reprint of material in preparation to be published in: **Kleinschmidt AT**, Chen AX, Pascal TA, Lipomi DJ. Modeling Energetics and Correlation between Improper and Dihedral Torsion in Conjugated Polymers. *In Review*. The dissertation author was first author of this paper.

Chapter 5, in full, is a reprint of material in preparation to be published in: **Kleinschmidt AT**, Ramji R, Chen AX, Pascal TA, Lipomi DJ. Correlation of Energetics in Distant Monomers of π-Conjugated Polymers. *In Review*. The dissertation author was first author of this paper.

VITA

2014	Bachelor of Science in Chemical Engineering, Stanford University
2020	Master's of Science in Chemical Engineering, University of California San Diego
2022	Doctor of Philosophy in Chemical Engineering, University of California San Diego

PUBLICATIONS

Kleinschmidt AT, Root SE, Lipomi DJ. Poly (3-hexylthiophene)(P3HT): fruit fly or outlier in organic solar cell research? Journal of Materials Chemistry A 5, 11396-11400 doi:10.1039/C6TA08317J (2017)

Sugiyama F, **Kleinschmidt AT**, Kayser LV, Rodriquez D, Finn M, Alkhadra MA, Wan JMH, Ramirez J, Chiang ASC, Root SE, Savagatrup S, Lipomi DJ. Effects of flexibility and branching of side chains on the mechanical properties of low-bandgap conjugated polymers. Polymer Chemistry 9, 4354-4363, doi:10.1039/C8PY00820E (2018)

Dhong C, Kayser LV, Arroyo R, Shin A, Finn M, **Kleinschmidt AT**, Lipomi DJ. Role of fingerprint-inspired relief structures in elastomeric slabs for detecting frictional differences arising from surface monolayers. Soft Matter 14, 7483-7491, doi:10.1039/C8SM01233D (2018)

Sugiyama F, **Kleinschmidt AT**, Kayser LV, Alkhadra MA, Wan JMH, Chiang ASC, Rodriquez D, Root SE, Savagatrup S, Lipomi DJ. Stretchable and Degradable Semiconducting Block Copolymers. Macromolecules 51, 5944-5949, doi:10.1021/acs.macromol.8b00846 (2018)

Kleinschmidt AT, Lipomi DJ. Stretchable conjugated polymers: A case study in topic selection for new research groups. Accounts of Chemical Research 51, 3134-3143, doi:10.1021/acs.accounts.8b00459 (2018)

Alkhadra M, **Kleinschmidt AT**, Root SE, Rodriquez D, Printz AD, Savagatrup S, Lipomi DJ. Mechanical Properties of Semiconducting Polymers. Conjugated Polymers: Properties, Processing, and Applications (2019)

Ramirez J*, Urbina A*, **Kleinschmidt AT**, Finn M, Edmunds SJ, Esparza GL, Lipomi DJ. Exploring the limits of sensitivity for strain gauges of graphene and hexagonal boron nitride decorated with metallic nanoislands. Nanoscale 12, 11209-11221, doi:10.1039/D0NR02270E (2020)

Chen AX, **Kleinschmidt AT**, Choudhary K, Lipomi DJ. Beyond stretchability: Strength, toughness, and elastic range in semiconducting polymers. Chemistry of Materials 32, 7582-7601 doi:10.1021/acs.chemmater.0c03019 (2020)

Kleinschmidt AT, Lipomi DJ. Unfavourable interactions enable stability. Nature Materials 20, 447-448, doi:10.1038/s41563-020-00889-x (2020)

Choudhary K*, Chen AX*, Pitch G, Runser R, Urbina A, Dunn TJ, Kodur M, **Kleinschmidt AT**, Wang BG, Bunch JA, Fenning DP, Ayzner AL, Lipomi DJ. Comparison of the Mechanical Properties of a Conjugated Polymer Deposited Using Spin Coating, Interfacial Spreading, Solution Shearing, and Spray Coating. ACS Appl Mater Interfaces 13, 51436-51446, doi:10.1021/acsami.1c13043 (2021)

Kleinschmidt AT, Pascal TA, Lipomi DJ. Computational Modeling of Molecular Materials for the Experimentally Inclined. *In Review*.

Kleinschmidt AT, Chen AX, Pascal TA, Lipomi DJ. Decoupling Planarizing and Steric Energetics to Accurately Model the Rigidity of π-Conjugated Polymers. *In Review*.

Kleinschmidt AT, Chen AX, Pascal TA, Lipomi DJ. Modeling Energetics and Correlation between Improper and Dihedral Torsion in Conjugated Polymers. *In Review*.

Kleinschmidt AT, Ramji R, Chen AX, Pascal TA, Lipomi DJ. Correlation of Energetics in Distant Monomers of π-Conjugated Polymers. *In Review*.

ABSTRACT OF THE DISSERTATION

Calculation and Modeling of Rigidity in Conjugated Polymers

by

Andrew Thomas Kleinschmidt

Doctor of Philosophy in Chemical Engineering

University of California San Diego, 2022

Professor Darren Lipomi, Chair
Professor Tod Pascal, Co-Chair

π-Conjugated polymers are an emerging class of materials for use in solar cells, transistors, LEDs, and sensors. Both the electronic and thermomechanical properties of π-conjugated polymers are governed by the fundamental rigidity of the polymer backbone. For example, we find that two highly similar compounds have radically different thermomechanical and electronic properties with only a small change in backbone structure. It would be advantageous to be able to characterize this property for use in designing novel polymeric compounds. One method to do this would be computational techniques, particularly molecular dynamics (MD). However, MD

simulations of π-conjugated polymers are often highly distorted due to nonbonded interactions, particularly steric interactions. This dissertation describes a universal method to use computationally chemically modified π-conjugated polymers to isolate the fundamental energy governing polymer rigidity. Not only does this method result in MD simulations that are significantly more accurate, it additionally allows for simple understanding of the underlying fundamental forces governing π-conjugated polymers. This improved understanding can lead to the use of this fundamental property in physical-organic chemistry experiments. Additionally, isolation of the fundamental energy governing π-conjugated polymer rigidity opened avenues to study effects that previous were entirely subsumed by nonbonded interactions. A novel type of torsion in π-conjugated polymers was characterized using this technique, resulting in yet another increase in accuracy in MD modeling of π-conjugated polymers. Additionally, the models show that this may be a significant source of torsion in the popular class of donor-acceptor polymers. An additional method was developed to quickly characterize the coupled styles of torsion in conjugated polymers. Finally, the method was used to correct for long-range interactions between monomers in π-conjugated polymers, resulting in a moderate increase in accuracy. These studies for the first time additionally allowed comparison of short-range and long-range rigidity in π-conjugated polymers. Overall, this work allows for characterization of the fundamental property governing π-conjugated polymers for rational design.

Chapter 1

Introduction

1.1 Computational Screening for Materials Science

The recent acceleration in the advancement of electronic hardware has greatly expanded the breadth of computational models and has made it commonplace to use computational simulations in nearly all research fields. Coupled with an ever-growing understanding of the fundamental physics, chemistry, and thermodynamics that govern the behavior of an atomistic system, computational models have become more sophisticated. In doing so, computational simulations have become less retrodictive and more predictive,[1–5] thus increasing their importance, ubiquity, and utility in all aspects of research. Nevertheless, the tools used by computational scientists can seem obscure to the experimentalist. Without this literacy, it is difficult to interpret or judge the merits of a computational study. A secondary benefit is to elucidate how experimentalists can use computational simulations to aid in their own work. In this Protocol, we attempt to demystify the process of computation. Our intended audience is an experimental scientist in the area of materials chemistry. We give special attention to organic materials, though the methods

are general and we address the differences in processes needed for simulations of inorganic media. This point of view reflects the idiosyncrasies of the authors. Most of our discussion is centered around classical molecular mechanics simulations—e.g., molecular dynamics and Monte Carlo simulations—which are applicable to a wide variety of molecular materials.[6,7] The methods and terminology used here are widely applicable to a range of molecular systems, even if specifics differ. Many articles describe the results of simulations. Nevertheless, it is often difficult for an experimentalist to glean the methods of designing and running one, which is critical for both evaluating computational work and for applying computational insights in experimental research. The typical workflow of performing a simulation, from start to finish, is outlined in Figure 1. In this process, three types of information are fed into a program, typically in the form of submission files. These submission files contain instructions designating the initial state of the system (i.e., a description of the system), how the program software should treat the system (i.e., what information should be calculated using what method), and how the hardware should treat the program (i.e., a definition of the computational environment). In this Protocol, we arbitrarily refer to these inputs, respectively, with the following nomenclature: "data file," "software input file," and "hardware input file". The program uses a model to. When this simulation is finished, the program outputs, which can then be analyzed by the researcher to understand (what data types). First, the initial starting condition for the simulation must be detailed (e.g., "data file"). We discuss how to determine and specify an initial condition for the system, and what pitfalls must be avoided in doing so. We then describe how the interactions between the different atoms of the system should be included in the model. This selection of all interactions in a simulated system is often referred to as the selection of a "force field."[8] Next, we describe how to create an input for the software (e.g., "software input file"). Additionally, we make suggestions

2

regarding judicious selection of a software. Likewise, we provide guidance on the running and managing the hardware ("hardware input file"). These hardware specifications are often specific to the system being simulated, and should be carefully considered to optimize the performance of the program software. Finally, we discuss several common types of computational studies that are found in literature and common types of analyses that are conducted. In doing so, we hope to better inform how experimentalists can incorporate computational simulations in their own work.

1.2 Computational Methods Used In Materials Science

A computer simulation using classical molecular mechanics is conducted by constructing a model in which all of the components (e.g., atoms, ions, and molecules) and interactions (e.g., Coulombic, covalent, van der Waals) in the system are defined independently. We center our discussion on simulations in which the motions and relative orientations of nuclei are the central focus, namely molecular dynamics (MD) and Monte Carlo (MC) simulations. While their methodology can differ significantly, the two have similar requirements. Likewise, both MD and MC simulations are often used to supplement experimental studies (e.g., in materials science). Therefore, we use both MD and MC simulations as a framework for introducing how computational simulations are conducted in this Protocol. Simulations are often purpose-made to have one central focus and to disregard other aspects of the chemical system in order to maximize computational efficiency. What one chooses to include or remove from a computational model affects the accuracy of the model, and thus one must choose to optimize between computational efficiency and accuracy. In simulations governed by classical mechanics, electronic and continuum behaviors are often simplified or ignored.[6,7,9,10] For example, one group of phenomena that

is generally excluded is the energetics and transport of electrons. Thus, formation and break-

age of bonds, energetic positions of the molecular orbitals, and electronic currents are typically

not explicitly considered.[11–15] Proxies for such phenomena are often used instead if the phe-

nomena are known to have an effect on the motion of the nuclei (e.g., polarizable and reactive

models).[16,17] However, these proxies are limited to obtaining the correct atomic configuration,

rather than modelling electron behavior (e.g., determination of the band gap of a material). On

the opposite extreme, classical molecular mechanics simulations generally lack the necessary

length and time scales to predict macroscale behavior, such as deformation of a solid sample of

macroscopic dimensions. Such behavior is typically the realm of continuum approaches. There-

fore, we see that the physical behavior that governs a model in part determines the time and

length scales it can accurately handle. The inverse is true as well; one must select a physical

model appropriate for the information they want to extract from the simulation. At the heart of

simulations based on classical molecular mechanics is the description of how the particles in-

teract. These interactions are often referred to as a "force field." The force field describes every

interparticle relationship in a system in which the relationship between particles is defined using

analytic terms (e.g., quadratic terms to describe bond stretching). The main alternative to a

classical mechanics approach is one using quantum mechanical calculations, and these quan-

tum mechanical force fields are typically referred to as ab initio simulations.[18,19] Regardless

of whether a classical or quantum mechanical force field is used to describe the interactions

between particles, the primary purpose of the force field is to move the atoms accurately in the

model. This Protocol primarily focuses on MC or MD simulations that require use of force fields,

although we will touch upon ab initio simulations where appropriate. The key characteristic of

classical molecular mechanics-style systems is that the fundamental components are single

atom-like indivisible features. This focus differentiates classical molecular mechanics simulations from simulations which explicitly model subatomic components like electrons (e.g., density functional theory, Hartree-Fock) or resolve higher length and/or time scales without explicitly modelling atoms (e.g., finite element analysis, finite-difference time-domain). However, classical mechanical simulations often differ in terms of atomic resolution. For example, hydrogen atoms are sometimes not explicitly considered, but rather grouped with the atom to which they are bonded. Going one step further, multiple similar atoms can be grouped into a "superatom" to simplify the simulation computationally. This class of simulations, in general, is described by the term "coarse-grained." On the other end of the spectrum, molecular mechanics simulations can be used to explicitly model subatomic particles to describe molecular motion (e.g., Drude oscillators). The general procedures described herein apply to any of these classes of simulation as well. Simulations using classical molecular mechanics can give insight into how the atomic configuration of a material changes naturally over time or in response to some external stimulus. This detailed picture of material properties comes at a price, in that it is typically very computationally demanding. As a necessity, modern-day simulations exploit the computing power of local clusters or, more commonly, supercomputing facilities. A supercomputer uses up to tens of thousands of processors simultaneously and automatically communicates between processors, providing the infrastructure to model more complex material systems faster than could be modelled using distributed computational systems (e.g., commercial laptops and desktops).[20] Even on a supercomputer, in conventional MD, a single nanosecond simulating a reasonably sized system—approximately 100,000 atoms—could take several hours for an unoptimized system. We do note, however, that optimizing the configuration of such a simulation could reduce this estimate by several orders of magnitude. As these time scales are substantial even on

5

specialized hardware, we will focus on describing simulations on a supercomputer. However, the general process this Protocol describes, at least for software operation, would be similar for any computational architecture (i.e., cloud resources). Simulations using classical molecular mechanics are a powerful tool, particularly when one wants detailed information about the structure or thermodynamics of a system. However, it is not without significant limitations. For an experimental researcher, one must maintain reasonable expectations for what information can be garnered and how complex the simulations can be made. Among the most popular uses for classical molecular mechanics simulations are those elucidating biological or biochemical systems for research in chemistry or biology (e.g., drug development). For example, for proteins, a molecular mechanics simulation can help determine the shape of the active site, how the active site changes in conformation upon the binding of a ligand (whether to the site itself or an allosteric binding site), or even the overall shape and positioning of the active site. In organic systems, these simulations may give insight into the structure of a polymer chain in solution and determine useful properties, such as its radius of gyration or end-to-end distance. In inorganic systems, these simulations can elucidate the crystallographic structure of materials, as well as thermodynamic observables (e.g., heat of formation). In general, the greater the complexity of a system, and the more computational power and time is used, the more accurate a simulation will be. There are a number of reasons why the complexity and computational cost of a simulation using classical molecular mechanics might increase. For example, simulation times increase when considering processes that (1) evolve over a long period of time, (2) require simulation of large cell sizes (e.g., a larger molecule, cell, or polymer chain), (3) undergo chemical changes, or (4) involve various nonequilibrium processes. In inorganic systems, the crystallization of many materials can take place over minutes or hours, far outside the accessible timescale

6

of equilibrium atomistic simulation. Another example might be the interaction of multiple large

protein complexes. Though critical dynamics might be captured on the hundreds of nanosec-

onds timescale (at the upper range of practicality), the sheer size of these systems makes direct

simulation difficult. Likewise, while nonequilibrium processes can be observed through classical

molecular mechanics simulation, one must take care that they are simulating a sufficient amount

of time to allow the simulation to adapt and change realistically. Additional complexity can be

added when (1) describing chemical reactions (e.g., the chemistry of bond breaking and form-

ing events) or (2) generally demanding the application of more complex interaction potentials

(e.g., reactive force fields or ab initio molecular dynamics approaches). Therefore, the general

complexity of evaluating the forces or energy of many systems of interest usually necessitates

downscaling of simulation time and size for practically. The computational schemes we focus

on are molecular dynamics (MD) and Monte Carlo (MC) methods (Figure 2).[6,7] These two ap-

proaches are similar in many ways. In both methods, the interactions between atoms define the

energies of the system and the forces between the atoms. A total energy is the assigned to

the system, or a net force is calculated for each atom. Monte Carlo simulations focus entirely

on the energy of the system. Here, the system energy is calculated from the initial configura-

tion. A random change (either displacing an atom, rotating a molecule, or inserting or deleting

a molecule) is then made and the energy of the new configuration is calculated. The simulation

then has a decision to make: accept this random change in configuration, or go back to the

original configuration. The decision occurs probabilistically, with the likelihood of keeping the

new configuration increasing as the new energy decreases.[21] In this way, the system will pref-

erentially—but not always—explore low energy conformations, while also randomly exploring

high energy transition states. Simulations using MC methods thus mostly surveys low energy

states while also traversing the energy barriers between low energy, favorable conformations. In contrast, molecular dynamics simulations evolve the systems forward in time based on the forces on the atoms. While Monte Carlo simulations samples configurations in a probabilistic fashion, MD simulations —at least in their purest form — move deterministically.[22] Based again on an initial conformation of atoms, a net force is calculated on each atom. The system is then advanced in time by numerical integration: the forces and masses of each atom are used to calculate the acceleration of the atoms according to Newton's second law.[23,24] The accelerations are then integrated over a small increment of time (called a "timestep") to generate a new position of the atoms. The timestep is typically related to the fastest motion in the system. For example, in organic materials, this is often a C-H bond vibration due to their very short timescale (on the order of femtoseconds).[25,26] The process is then iterated until the system has explored enough configurations such that thermodynamic properties can be obtained. MC and MD simulations both determine the energetic minima and distribution of energy states of a system at equilibrium. However, they have key differences in how they proceed. MD simulations sample configurations that are close in energy to the initial configuration (relative to the temperature), which means that the chances of capturing very high energy states or overcoming large energy barriers is small. MC simulations explicitly encompass the entire energy landscape, but the time evolution of the system is lost. Due to the reliance of the MC process on random moves, it can more easily overcome energy barriers in a free energy surface than MD. In other words, MC can traverse high energy barriers between energetic minima more simply than MD. However, this advantage comes at the cost of mechanistic information—that is, how the system might actually traverse the energy landscape. Which approach is most useful for a particular system depends on their computational performance and the required data.[27] The ability to access the temporal

features of the system is an advantage of MD simulations, and allows for useful properties, such as self-diffusion, to be easily calculated. Due to this type of insight into time-dependent properties, MD simulations are usually preferred in materials science. However, if one is primarily interested in the equilibrium morphology of materials, Monte Carlo techniques are attractive, as they are typically more efficient at utilizing computing resources. This computational efficiency is especially clear in systems defined by rugged or complicated potential energy landscapes. Additionally, Monte Carlo is often superior at evaluating systems in different phases, such as liquid-vapor equilibria and adsorption.[28,29]

1.3 Inputting Information

Three types of information are required to initialize a simulation: a descriptor of the initial state of the system, instructions for the software, and instructions for the hardware. This information is generally inputted in the form of submission files (e.g., files that are uploaded or read). For simplicity, we refer to these inputs, respectively, as "data file," "software file," and "hardware file." We note that the initial state of the system could be directed embedded within the program input (e.g., script) rather than being a data file that is uploaded. The data file describes the initial position of all the atoms and defines how the atoms will interact. A crucial aspect of initializing the system is the initial placement of the atoms, which is often defined in the data file. In both MC and MD, the simulation is likely to initially move towards an energetic minimum nearby this initial configuration. If the initial configuration is near an unphysical (i.e., unrealistic) energetic minimum—e.g., extremely high in energy, but with similar conformations that are even higher in energy—the simulation will progress within the unphysical minima, and unphysical results will be obtained.[30–33] The initialization of the simulation is also of great importance to the workflow

9

one chooses. There are many programs which will simply run a MD or MC simulation after it is initialized.[34–42] Therefore, the only time one interacts with the simulation is to set it up at the start (apart from analyzing the outcome after the simulation is finished). The start of the simulation is thus a crucial touchpoint. Much like an experimentalist must optimize measurement parameters to minimize artifacts due to the measurement itself, judicious selection of the initial conditions can facilitate the analysis of the finished simulation. One may create the data file simply by "brute force," whereby the coordinates of the atoms are generated by molecular rendering software (e.g., Avogadro).[43] Such an approach works well if the system is relatively small. However, for systems comprising thousands of atoms, this method is impractical. An additional complication is the need for randomness in the initial position. For example, consider a single chain of polyethylene initially stretched out. The all-trans conformation—in which all dihedral potential energies are minimized—is likely an enthalpic metastable minimum. Thus, this extended conformation is what is produced by some molecule drawing software. However, an extended conformation is exceedingly unlikely to occur in polyolefin chains of appreciable length, because it is highly unfavorable entropically. An outstretched polymer chain thus represents a poor choice of initial position, unless the simulation is one that is purpose-written to utilize an outstretched chain input (e.g., one that probes chain flexibility by collapsing it). Instead, it is (often) optimal to create random configurations of the atoms using Boltzmann weighting. One can find that randomness is required in many different systems. For example, in a real sample of a liquid, it would be essentially impossible for molecules to be oriented in the same direction. Therefore, the molecules should be rotated to introduce randomness while maintaining a Boltzmann distribution. Similarly, when simulating a glass, not every atom is evenly spaced (as in an ideal crystalline lattice), and so some degree of randomness should be built into the

initial state. To generate more realistic initial positions of atoms, it is often necessary to use a program to impose randomness in the system and produce a data file (Figure 3). Other groups have thoughtfully discussed the many different ways randomness can be induced, and the advantages and disadvantages of each method. In MD simulations, an important consideration is the accounting of steric repulsive forces at short distances. That is, for many types of pairwise interactions, the energy of repulsion between atoms increases dramatically when atoms get too close. The Pauli repulsion force is frequently modelled in a force field by an exponential function. The exponential nature of the repulsion means that two molecules initialized too closely will move apart rapidly at the next timestep. In situations when the atoms move farther than can be numerically accounted for, the simulation becomes unstable (and can fail or crash). Therefore, molecules should be initialized with adequate initial spacing. Several software packages exist to ensure this aspect of a reasonable initial configuration.[44,45] Alternatively, in particularly difficult cases, a different style of interaction which does not involve exponential repulsive forces (e.g. soft potentials) may be used at the beginning of a simulation. Finally, depending on the diversity of starting configurations, it may be useful to generate multiple different starting data files and to simulate them simultaneously.[46,47] For example, simulations of polymer films above their glass transition will remain relatively frozen in their initial position. Therefore, multiple simulations averaged together will give significantly more accurate results. Another critical component of a simulation is the implementation of its interactions. A classical MC or MD simulation defines its interactions according to the relative orientation of indivisible atoms. This manner in which interactions are implemented is defined as the "force field." The force field analytically defines all interactions deemed important to the outcome of the simulation, such the flexibility of a bond or long-range attractivity of an atom. The force field is an all-inclusive entity: a single force

field defines how any two arbitrary atoms several angstroms apart will be treated, as well as how two bonded atoms will behave. The choice of force field is thus crucial. One can usually select from an existing force field, as developing one independently is difficult and many force fields are already widely available for a variety of systems (Table 1).[37,48–66] It is often better to use a customized force field, if one already exists, as these have usually been optimized to reproduce the experimental properties of related systems. Such force fields exist for a variety of applications.[35,36,65,67,68] For example, several different force fields exist to model proteins, such as AMBER and CHARMM.[67,69] Whether the force field is bespoke or generic, one must ensure that the force field is appropriate for the system under consideration. If a key interaction is not contained in the instructions of an existing force field, one much either add it to the force field manually or generate a custom force field.

For modeling organic structures, certain choices for the style of interaction used in the force field are standard (Figure 4). While the available types of atomic character and parameters differ, the same general structure is used by common force fields (e.g., CHARMM, OPLS, or AMBER).[60,67,69] For example, arbitrary atoms are usually treated as interacting using Lennard-Jones 12-6 potentials. Lennard-Jones 12-6 interactions are commonly defined by the unfavorable Pauli energy expressed as the inverse distance between the atoms, r, raised to the twelfth power and a favorable dispersion energy dictated by inverse r to the sixth power: $E = 4\varepsilon[(\sigma/r)^{12} - (\sigma/r)^6]$. The ε in the equation is proportional to the intensity of the interaction, while indicates the distance at which the force goes from attractive to repulsive. Covalent bonds are defined between atoms, with different spring-type parameters for different pairs of atoms and bond orders. Angles are also defined to enforce the local geometry of the molecule. A final common type of interaction in simulations of organic molecules occurs in relation to both

12

conventional dihedral and improper dihedral angles. Conventional dihedral angles are simple torsional angles (as defined in a basic organic chemistry course), whereas improper angles often dictate geometry in certain molecules (e.g., ammonia). In contrast to organic materials, the behavior of inorganic materials is described by force fields of a different form.[50,52–58] The behavior of inorganic materials is highly dependent on the presence of metallic bonds (and bonds to metal atoms), rather than covalent bonds. Simulations of inorganic material systems will often have interactions such as "embedded-atom" energies—energetic interactions which are more favorable when atoms are around many similar atoms. Covalent-style bonds are often eschewed entirely in favor of nonbonded-style forces, which depend only on distance. Angles between atoms may also be included as part of these distance-dependent forces. Moreover, interactions such as dihedral and improper angles are typically not needed for inorganic systems. As a final note, we emphasize that a force field is a convenient construct for the approximation of intermolecular forces. The simulation must include approximations of all important forces within the system. That said, which forces qualify as "important" in a system remains at the discretion of the researcher. For example, interactions such as London dispersion interactions do not occur simply as pairwise functions but may instead have contributions from multiple neighboring atoms. These many-body forces are not entirely captured using simple Lennard-Jones interactions. There are force fields which deal with these interactions.[50,56–58] However, more complex force fields require more computational power, and thus researchers must decide whether the additional accuracy is worth the additional computational cost. Alternatively, force fields may be eschewed entirely in favor of a quantum mechanical calculation.[18,19] Quantum mechanical calculations provide significantly greater accuracy for a system. Additionally, one would no longer need to provide specific approximations for all relevant forces within a system. Rather, the rel-

evant behaviors of the system will emerge naturally from the solution of the Hamiltonian. The tradeoff is, once again, that these ab initio calculations are substantially more computationally intensive to perform. Thus, to counter this increased computational cost, the number of atoms in the system or length of time simulated generally must be decreased.

1.4   Running Simulations

Once the simulation begins, little input is required of the researcher. As such, the choice of which software to use is important. Researchers must balance competing interests of time and customizability. Scientists often look at novel systems that are not yet well understood, and these novel systems may require modification of existing software to handle interactions of interest. Some systems will be better suited to handle modifications, though at times this will come at the expense of computational efficiency. However, this is general advice, and it should be noted that every situation is different. For a software package to provide the desired performance, one must understand one's particular needs. Until now we have focused on simple molecular dynamics or Monte Carlo simulations, which are somewhat limited in their usefulness. Conventional MD simulations are often run on the order of nanoseconds. Monte Carlo simulations are similarly run for enough time steps to explore local minima, but not to explore all accessible energy states. A variety of newer methods have been developed for modified versions of MC or MD simulations to explore time and space more rapidly, allowing the simulation to garner more data without a significant increase in computational time.[30,115–123] These methods—termed "advanced sampling" methods—are useful for collecting more complete sets of data. That said, the researcher must ensure that an advanced sampling method of interest is compatible with or easily incorporated into their simulation program, or else undertake the (sometimes laborious)

process of converting to another code.

1.5   Analyzing the Data

All that remains is to collect and organize the simulation data into an understandable format. The raw output of an MC simulation that is returned to the user is the position of every atom in every conformation. For an MD simulation, the equivalent output is the position of every atom at every timestep. This quantity of data is often too massive to be of immediate use. Some simulation codes have built-in analysis capabilities, allowing the user insight into the simulation as it proceeds. Alternatively, data analysis must be performed afterwards with commercial, open source, or custom-made software. The code used for analysis can range greatly in complexity. For example, a fairly straightforward script can be used to calculate the radius of gyration of a polymer, while more complicated calculations can be done to determine far more complex material properties (e.g., example). For example, if the system in question is being stretched, a program can be written to calculate the stress tensor on the system as a whole, or atom by atom. For a polymer system, the radii of gyration and crystallinity can be derived from knowledge of every atomic position. In a protein, changes to the shape of the active site or measurement of ligand binding affinity can be calculated. For inorganic systems, thermodynamic quantities or information about the system's crystal structure can be extracted from a simulation.

1.6   Outline of the Thesis

The next chapter, Chapter 2, of the thesis will be an overview of an experimental study in which I performed all electronic measurements. The work described therein will describe

15

the substantial differences in experimental behavior for polymers with even small differences in backbone structure. This provides the motivation for the rest of this work. Next, I developed a method to quantify the energetics of polymer backbone structure, which is detailed in Chapter 3. The method allows for separation of delocalization effects and nonbonded energies in conjugated polymer. This technique opened up further avenues of research, namely the analysis of improper torsion, a heretofore unstudied method of torsion in conjugated polymers. The findings of the first analysis of this torsion is demonstrated in Chapter 4. Finally, my work using this technique again to study the long-range effects of conjugation in conjugated polymers is detailed in Chapter 5. Each section has its own introduction and conclusion on its specific subject matter.

1.7   Acknowledgments

Figure 1.1: Overview of running a simulation. The researcher begins by creating the data file (or has it embedded within the program input) to inform the program of the initial arrangement and specific interactions of all atoms (Figure 1.3). The researcher must then create a software input file, which uses the data file to begin the simulation on the program and tells the program how to run the simulation (Figure 1.5a). A hardware input is also required if specialized hardware is used (i.e., a supercomputer), which informs the hardware to run the program according to the program input as well as the best way to run the program on the hardware (Figure 1.5b). These three tasks converge to cause the simulation to be carried out. After the simulation is complete, it is then analyzed by the researcher.
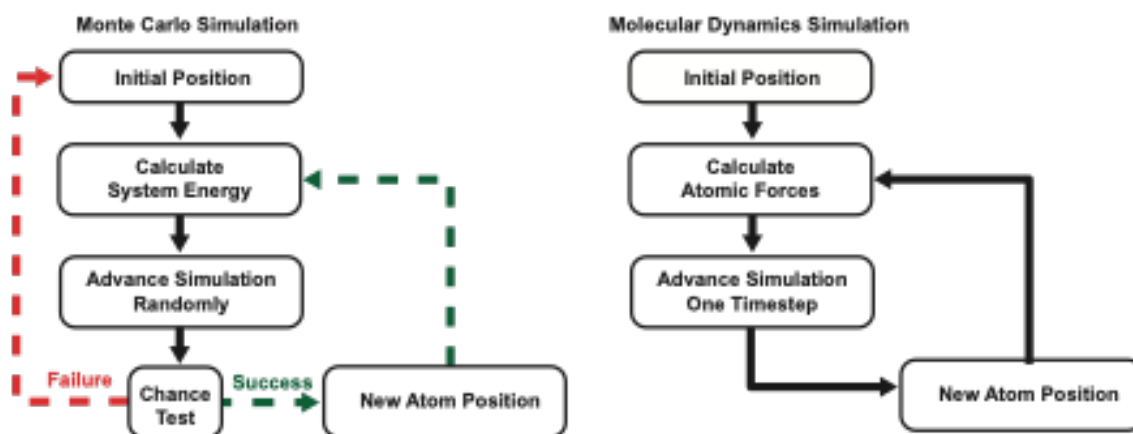
Figure 1.2: Overview of Monte Carlo (MC) and molecular dynamics (MD) simulations. Both systems progress from an initial, user-defined arrangement of atoms. In Monte Carlo simulations, the energy of the system is calculated, while in a molecular dynamics simulation the net force on each atom is calculated. Monte Carlo simulations are then advanced randomly and given a probabilistic "chance" test. The dotted lines represent possible outcomes: the system could fail the test and return to its initial position, or succeed in the test and advance to its new atomic configuration. In comparison, molecular dynamics simulations are advanced deterministically, using the force on the atoms to determine where they will end up a very short interval in the future. The atoms are then deterministically moved to their new configuration. In both MC and MD simulations, these processes are then repeated (i.e., a new energy of the system is then calculated in a Monte Carlo simulation while new forces are calculated in a molecular dynamics simulation).
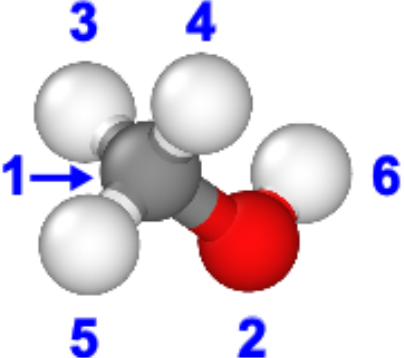
Pseudocode

Example LAMMPS file

Step 1: Create Header

n atoms
m atom types
r bonds
s bond types

```
6 atoms
5 bonds
7 angles
3 dihedrals
2 impropers

X bounds
Y bounds
Z bounds
```

Step 2: Parameters
Initiate **parameters**, p, for each atom type and interaction type

Parameter
Atom type 1   p1   p2
Atom type 2   p1   p2
Atom type m   p1   p2

Parameter
Bond type 1   p1   p2
Bond type 2   p1   p2
Bond type s   p2   p2

```
Masses
1    12.011
2    15.999
3    1.008

Pair Coeffs #sigma, epsilon
1    0.066    3.50000
2    0.170    3.12000
3    0.030    2.50000
4    0.000    0.00000

Bond Coeffs #Kb, r0
1    320.00    1.41
2    340.00    1.09
3    553.00    0.945
:
```

Step 3: Definitions
Define each atom and bond in the molecule as an atom type or interaction type. If the object is an atom, indicate charge and position. If the object is a multiatom interaction, indicate other atoms involved.

Type
Atom 1   Atom type   Definition
Atom 2   Atom type   Definition
Atom n   Atom type   Definition

Type
Bond 1   Bond type   Definition
Bond 2   Bond type   Definition
Bond r   Bond Type   Definition

Type
Angle 1   Bond type   Definition
Angle 2   Bond type   Definition
Angle r   Bond Type   Definition

```
Atoms
1  1  1  -0.00491 1.000 1.000 0.000
2  1  2  -0.58730 -.416 1.000 0.000
3  1  3  0.076700 1.364 1.000 -1.303
4  1  3  0.076700 1.364 .1146 0.526
5  1  3  0.076700 1.354 1.899 0.509
6  1  4  0.406200 -.701 1.919 -0.460
```

Figure 1.3: An example of a data file in the LAMMPS style. We divide the data file into three primary sections: Header, Parameters, and Definitions. In the "Header" section, details about the rest of the data file are indicated. In our example, how many of each interaction type and how instances of each interaction exist are notated. In the other sections, we divide the information into pieces. In the Parameters section, the type ID of atom or interaction is given (red), then the parameters (black) which define the interaction are defined (e.g. there is a type 1 bond with a Kb of 320.0 and equilibrium distance of 1.41 Å). In the "Definitions" section, a type ID (red) is given for every atom or interaction (blue) (e.g. a bond given a type of 1 will have a Kb of 320.0 and equilibrium distance of 1.41 Å). Finally, in the placement section the atoms involved in each interaction are given (green) and initial positions (purple) and charges (orange) are defined for every atom in the system.
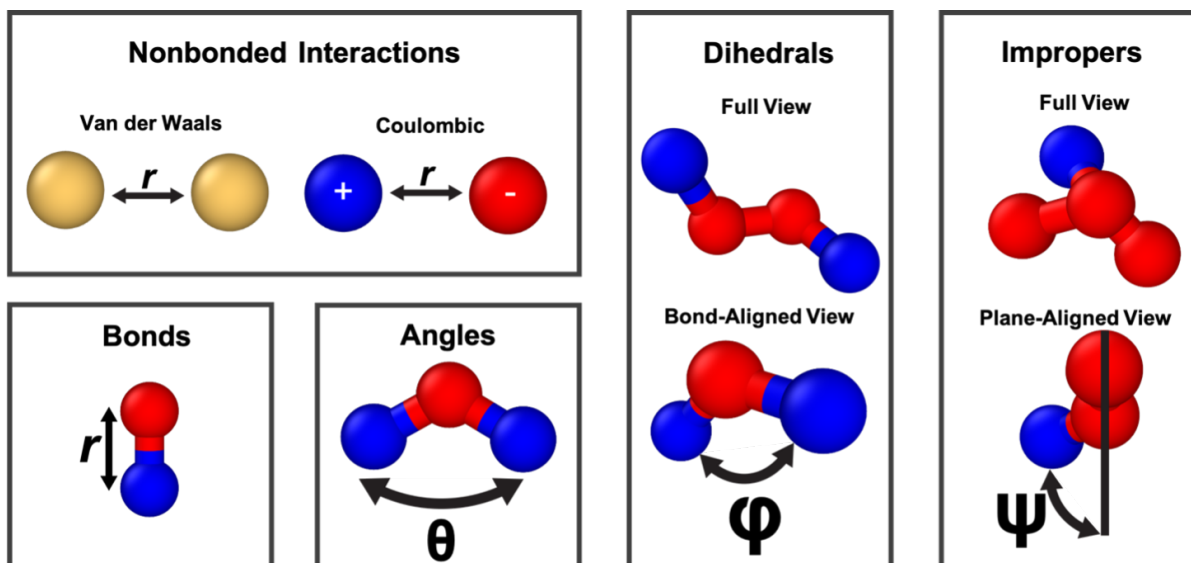
Figure 1.4: Types of interactions in a standard force field (e.g., a force field for proteins or hydrocarbons. The atoms undergoing forces are defined in blue, while other atoms in the system are shown in red. Atoms which are not connected through bonds experience two types of force. First, they experience van der Waals forces. In particular, the Pauli repulsion force at short distances and London dispersion forces at intermediate distances. These forces are usually described using a Lennard-Jones potential. Additionally, for systems where atoms have partial atomic charges, the atoms experience Coulombic interactions. In contrast, atoms that are chemically bonded experience additional forces. Directly bonded atoms interact based on their distance apart (usually with a harmonic function). Three atoms that are bonded in a linear fashion interact with a potential based on the angle with respect to the central atom. Four atoms that are bonded in a linear fashion interact with a potential based on their orientation about the central bond, called a dihedral interaction. Improper angles are torsions created when one atom is bonded to three other atoms and a specific orientation (e.g., planarity) is required (Full View). The potential is calculated based on the angle between one atom and the plane defined by the other three atoms (Plane-Aligned View).

a

Pseudocode	Example File

Step 1: Define Input Styles, Read in Data File (initial positions)

Pseudocode	Example File
Units [real, metal, nano]	`units        real`
Atom Style [info given for atoms]	`atom_style    full`
Pair Style [pairwise interaction type]	`pair_style    lj/cut/coul/long`
Bond Style [bond interaction type]	`bond_style    harmonic`
.	`angle_style   harmonic`
.	`dihedral_style opls`
.	`improper_style cvff`
.	`kspace_style  pppm 1.0e-4`
Input Data [read in data file]	`read_data     Methanol.data`

Step 2: Define Simulation Parameters
Define parameters for the system, such as timestep or statistical mechanical ensemble
Give values for ensemble, such as starting and ending temperatures and/or pressures

Timestep Value	`timestep 1.0`
Definitions Ensemble Start (T,P) End (T,P)	`fix 1 all npt iso 1.0 1.0 100.0` `&300.0 300.0 1000.0`

Step 3: Run Program
Run for set number of timesteps/random moves and output data

Simulation Running Time	`run 5000`
Final Data Output	`write_data Final_Config.data`

b

Pseudocode	Example File

Step 1: Define Simulation Parameters

Pseudocode	Example File
Name of Job (Used for error files, etc)	`#SBATCH --job-name="Example"`
Output Location (for hardware output)	`#SBATCH --output=Example`
Number of Nodes	`#SBATCH --nodes=1`
MPI tasks/node	`#SBATCH --ntasks-per-node=128`
Processors/MPI task	`#SBATCH --cpus-per-task=1`
Time Limit	`#SBATCH --time=4:00:00`

Step 2: Import Helper Programs

Import command [helper program]	`module load slurm`
	`module load cpu`
	`module load [MD_CODE]`

Step 3: Run Program
Run for set number of timesteps/random moves and output data

Run command	`srun [MD_CODE] -in in.Example`

Figure 1.5: LAMMPS input to the simulation (a) software and a (b) hardware input file. (a) The software input file. In Step 1 the program is told what to expect: how information about the atoms (e.g. location, atom type) will be given, what type of pairwise interactions will be used (in the example file, Lennard-Jones and Coulombic interactions), and so on. In Step 2, the simulation is instructed in how to run. Specifics of how to run the program are given, namely how big of a timestep to take in femtoseconds (red) and what statistical mechanical ensemble will be used (blue). Specific information for the statistical mechanical ensemble (e.g., starting and ending pressures, purple, and temperatures, yellow) is additionally specified for the program. In Step 3, the program is run for a set number of timesteps (run 5000). Some type of output command is used to get the final configuration of atoms or snapshots as they progress in the system. (b) A hardware input file, breaking down the information into three steps. Various supercomputing centers use different schedulers. Here, we provide example input using the SLURM scheduler.[70] In Step 1, we define the basic parameters of the program, such as the job's name, the place to put hardware output information, and how long to run the job for. In Step 2, the hardware is instructed to load important software for use on the simulation. In Step 3, the supercomputer is instructed to run the simulation.

Chapter 2

Stretchable and Degradable

Semiconducting Multi-Block

Copolymers

This chapter describes the synthesis and characterization of a class of highly stretchable and de-gradable semiconducting polymers. These materials are multi-block copolymers (BCPs) in which the semiconducting blocks are based on the diketopyrrolopyrrole (DPP) unit flanked by furan rings and the insulating blocks are poly(ε-caprolactone) (PCL). The combination of stiff conjugated segments with flexible aliphatic polyesters produces materials that can be stretched $\succ 100\%$. Re-markably, BCPs containing up to 90 wt% of insulating PCL have the same field-effect mobility as the pure semiconductor. Spectroscopic (ultraviolet-visible absorption) and morphological (atomic force microscopic) evidence suggests that the semiconducting blocks form aggregated and perco-lated structures with increasing content of the insulating PCL. Both

PDPP and PCL segments in the BCPs degrade under simulated physiological conditions. Such materials could find use in wearable, implantable, and disposable electronic devices.

2.1 Introduction

Semiconducting polymers and biomacromolecules share few characteristics beyond the fact that their molecular structures contain carbon and thus that they share the classification of "organic." Electronic materials that combine semiconducting properties with properties inspired by biological tissue, however, have the potential to enable a new class of wearable, implantable, and disposable devices. Mechanical compliance commensurate with that of the skin and internal organs could permit seamless interfaces between synthetic materials and these biological structures.[128–131] Moreover, the property of biodegradability could eliminate the need for surgeries to remove implanted devices, and could reduce the environmental impact of their disposal. Currently, the most successful approach to endowing medical devices with stretchability and biodegradability is based on silicon nanomembranes and metallic interconnects.[132] Semiconducting polymers, on the other hand, offer the possibilities of synthetic tunability, oxide-free interfaces, mechanical toughness, detection of a range of physiological signals, and the potential for scalable manufacturing by printing.[133] This article describes highly stretchable and biodegradable multi-block copolymers based on diketopyrrolopyrrole (DPP)—a component of semiconducting polymers that have achieved high charge-carrier mobilities (1 cm2 V1 s1) in organic field-effect transistors (OFETs)[134,135]—and poly(-caprolactone) (PCL), an aliphatic polyester that degrades under simulated physiological conditions.[136] Remarkably, one of the materials synthesized exhibits no decrease in charge-carrier mobility in OFET even with insulating PCL content up to 90 wt%. The invariance in mobility suggests that stretchability and

biodegradability can be incorporated into semiconducting polymers described. One of the long-purported advantages of organic semiconductors is mechanical compliance, i.e., flexibility and stretchability. Semiconducting polymers in particular are logical candidates for applications demanding deformability because polymer chains form entanglements, which produce the extensibility and toughness characteristics of plastics. The rigidity of the π-conjugated units, the semi-crystalline microstructure, and the generally high glass transition temperatures, however, are usually incompatible with mechanical softness. Several approaches have been used to circumvent the apparent incompatibility of semiconducting behavior and mechanical softness.[137] One goal of this research is to achieve stretchability $\geq 50\%$, which is similar to that of human skin.[138] One approach to improving the mechanical robustness of polymer semiconductors is to blend amorphous insulating polymer with semiconducting polymers.[139–142] Blending, however, leads to large-scale phase separation, which may limit charge transport. Alternatively, polymer semiconductors can be synthetically modified to improve their mechanical properties (e.g., engineering the backbone and side chain) to produce single-component materials not susceptible to phase separation.[143–146] Devices that degrade into harmless byproducts have the potential to reduce surgeries for removal, which will be desirable given the risk of hospital-borne illness. Moreover, materials that degrade in the environment have the potential to decrease e-waste. Recently, the Bao laboratory reported a degradable low-bandgap semiconducting polymer with a high charge-carrier mobility.[147] This material was condensed through imine linkages, which require acidic conditions to hydrolyze. Moreover, the mechanical properties of these materials were not reported. In this work, we designed a new class of stretchable and biodegradable semiconductors whose defining structural motif is a segmented copolymer with semiconducting conjugated segments linked by soft, biodegradable PCL segments. We measured the mechan-

ical properties, field-effect mobility, and biodegradability of these polymers in phosphate buffers solution. By tuning the structure of the semiconducting segment, it was possible to retain interconnected pathways for charge transport even with high loadings of the insulating fraction. The approach shown in this work could be extended to various conjugated polymers that are synthesized by coupling polymerizations.[148,149]

2.2 Results and Discussion

For the conjugated segments, we chose a polymer based on the N-substituted DPP unit flanked by two furan rings (Figure 2.1a).150 The DPP unit and furan rings are susceptible to decomposition by acids, peroxides, and enzymes.147,151 We chose PCL for the flexible segment since PCL exhibits high elongation at break ($\succ 1{,}000\%$) and biodegradability. Our strategy to synthesize BCPs involved connecting PDPP and PCL (PDPP-b-PCL) at the respective end-hydroxyl units using diisocyanate linking agents (Scheme S1, Supporting Information). First, hydroxyl end-capped PDPP were synthesized by Stille polymerization of dibromo DPP with thiophene (T) or thienothiophene (TT) bis-stannane in the presence of 5-bromo-2-thiophenemethanol as an end-capping agent.[152] Next, PCL was synthesized by ring-opening polymerization using 1,6-hexanediol to afford hydroxyl-terminated chains.[153] The molecular weight of the PDPPs and PCL we obtained were comparable. Finally, the PDPP and PCL segments connected with hexamethylene diisocyanate to form urethane linkages.154 Since formation of the urethane linkage does not generate by-products nor requires a catalyst, the BCPs were easily purified. After final reaction, we confirmed the increase of weight-average molecular weight by GPC using both refractive index and UV-Vis detectors, the formation of urethane linkages by NMR and the ratio of PDPP to PCL by NMR.

The tensile response of organic semiconductors is an important predictor of their durability in actual devices.[137] In particular, a high elongation at break increases the robustness of devices against fracture.[146] To measure the mechanical properties of the BCPs, we first used a "film-on-water" (FOW) technique originally described by Kim and coworkers.[155,156] Spin-coated films were removed from a glass substrate, floated on the surface of water, and subjected to tensile pull testing to obtain the stress-strain curves shown in Figure 2.1b. The improvement in mechanical robustness with increasing PCL content is clearly observed; the toughness increased by a factor of 22 for the sample containing 75 wt% of PCL compared to T-0. Furthermore, images of the breaking point, shown in the inset of Figure 2.1b, demonstrate that increasing the PCL content leads to fracture with greater ductile character. Importantly, the films of T-50 and T-75 could withstand over 50% elongation without fracturing.

Since semiconducting materials are fabricated on elastomeric substrates in stretchable devices,128 we also measured the micro-crack behavior on poly(dimethylsiloxane) (PDMS, Figure 2.1c). Thin, spin-coated films were removed from a glass substrate, floated on the surface of water, transferred to PDMS, and dried with compressed air. The fracture behavior of BCPs on elastomers is correlated with the film-on-water measurements, and T-50 and T-75 can be effectively stretched to 100% strain on PDMS without resulting in any visible cracks. In comparison, films of physical blends of T-0 and PCL 50/50 wt% (T-blend-50) show pervasive cracking at 100% strain. These results reflect the superiority of BCPs (i.e., covalently bonded polymers)—as opposed to physical blends—for improved mechanical properties. We also applied this synthetic strategy to another DPP segment in which the thiophene unit (T) was replaced with the fused thienothiophene (TT) unit (TT-0). DPP units coupled through the TT unit usually show higher charge carrier mobility than those coupled through the T unit, but are less flexible.[157] Using our

approach, we again observed significant improvement in stretchability, with homogeneous films achieving over 100% strain without cracking (TT-50). The charge-carrier mobility of semiconducting materials is an important metric for device performance. Unfortunately, many molecular design strategies that improve the stretchability of materials often reduce their mobility.[137] We measured charge-carrier mobility of our materials using top-contact, bottom-gate field-effect transistors (FETs) after annealing at 100 °C for 1 h (Figure 2.2a). For the devices based on BCP-T, we observed that the mobility declined with increasing PCL content: the mobility of T-0 was an order of magnitude higher than that of T-90 (90 wt% PCL). In contrast, the devices fabricated with BCP-TTs showed the remarkable result of no appreciable change in mobility at any fraction up to 90 wt% PCL. We hypothesized that this difference in electronic performance between the segmented BCPs was due to the morphological differences between the materials.[158] To determine what morphological differences could account for such different electronic behavior with high loadings of PCL, we characterized the morphology of the films using atomic force microscopy (AFM). Since the surface morphologies of as-spun films resulted in images in which the two phases were poorly differentiated, we observed micro-phase separation behavior of PDPP segments after selectively etching the PCL segments by exposing the BCP films to a solution of 0.5 M sodium hydroxide in water/methanol = 60/40 (volume/volume)% (0.5 M NaOH solution). The removal of PCL was monitored by 1H NMR spectroscopy. As shown in Figure 2.2b, comparison of the AFM height images revealed that the PDPP segments in TT-75 thin film formed more percolated, fiber-like networks than did the segments in T-75 films, which formed disjointed globular phases. This morphological observation is consistent with the differences in electronic behavior of the two BCP systems and can, in part, be attributed to an increase in the stiffness of the PDPP segments containing TT units.

Charge transport through the PDPP phase is strongly influenced by the ordering of PDPP segments. This molecular-scale ordering can be correlated to the state of photophysical aggregation, which is observable through ultraviolet-visible (UV-vis) absorption spectroscopy. To analyze the aggregation of PDPP segments in BCPs, we measured the UV-vis spectra of BCP films after annealing at 100 °C for 1 h (Figure 2.2c, d). As we increased PCL content in the BCP-TTs, we observed a red shift in absorbance of PDPP segments and an increase in the relative height of the 00 to the 01 vibronic peaks (A0-0/A0-1), which correlated with the strength of intrachain J-aggregation.[159,160] This trend implies that the aggregation of PDPP segments in the BCP-TTs was enhanced by PCL. On the contrary, the BCP-Ts show a decrease in A0-0/A0-1 as well as a blue shift in absorbance, indicating a disturbance of aggregation of PDPP segments by the addition of PCL. In vitro degradation experiments were performed to investigate the degradation rate of BCP-T (Figure 2.3a). The amount of residual PCL was calculated by 1H NMR by comparing the peak integration of PCL segments (4.1 ppm) to that of hexyldecyl groups in PDPP segments (0.8 ppm). The PCL segments in T-50 were completely degraded in a 0.5 M NaOH solution in less than 3 days, confirming that PCL segments in the BCP-Ts can be fully degraded. However, immersion of T-50 in phosphate buffered saline (PBS, pH = 7.4)[161] at physiological temperature (37 °C) only degraded the PCL segments of T-50 to 48% of their original content after 12 weeks.

While the purpose of incorporating the hydrolyzable polyester segments was to confine the degradation to these flexible units, we could not discount the possibility that the conjugated PDPP units were also degraded by PBS. To quantify the degradation of the conjugated segments, we performed the following experiment. First, we immersed a thin film of T-0 in PBS for 12 weeks. We then dissolved the film in chloroform and obtained UV-vis spectra. We found

that the ratio of the absorbance peaks, A0-0/A0-1, decreased by 6% after this treatment (Figure 2.3b). This result suggests that the conjugated unit itself was partially degraded by the PBS, though we were not able to determine the identity of the products of degradation. Again using the ratio A0-0/A0-1 as a metric, degradation of the conjugated units of T-50 was twice as great as for T-0. The difference may be because of faster degradation kinetics of the conjugated units due to an increase in surface area of the PDPP segments upon decomposition of the PCL. AFM height images further supported our observations regarding degradation of PDPP and PCL segments (Figure 2.3c). The roughness of T-0 films increased after 12 weeks of immersion in PBS; we attribute the increase in roughness to the degradation of PDPP segments. On the other hand, the surface morphology of T-50 films dramatically changed compared to T-0 films due to the decomposition of PCL segments. The average surface roughness (R_a) of T-50 films increased to a similar value as the Ra of T-50 films etched with 0.5 M NaOH solution (Figure S3, Supporting Information).

2.3 Concluding remarks

We reported a new class of stretchable and degradable semiconducting polymers based on multi-block copolymers of PDPP and PCL. Given that our approach to stretchability and biodegradability is based on the addition of PCL segments, we believe this approach is extendable to other conjugated polymers. Furthermore, the retention of field-effect mobility in these materials, particularly the BCP-TT series, suggests that biologically inspired properties need not come at the expense of electronic properties. These materials could lead to devices that are not only stretchable, degradable, and disposable, but also those having other properties inspired by biological tissue, namely self-repair.

2.4   Materials and Methods

Synthesis of Conjugated Blocks

For the BCP-T blocks, DPP-Br (499 mg, 0.570 mmol), 2,5-bis(trimethylstannyl)-thiophene (T) (247 mg, 0.600 mmol), 5-bromo-2-thiophenemethanol (T-OH) (11.9 mg, 0.060 mmol), tris(dibenzylideneacetone)dipalladium(0) (Pd2(dba)3, 2.7 mol %), and tri(o-tolyl)phosphine (P(o-tol)3, 10.7 mol %) were charged within a 25 mL 3-necked flask, cycled with nitrogen, and subsequently dissolved in 10 mL of degassed chlorobenzene (CB). The mixture was stirred for 20 h at 110 °C. The reaction mixture was allowed to cool to 25 °C, 5 mL of CHCl3 were added, and the polymer precipitated into methanol (200 mL). The precipitate was purified via Soxhlet extraction for 4 h with methanol and 6 h with acetone, followed by collection in CHCl3. The polymer T-0 was obtained as a dark blue solid (428 mg). A similar procedure for the BCP-TT blocks is reported in the Supporting Information.

Synthesis of Soft Blocks

ϵ-Caprolactone (ϵ-CL) (2.28 g, 20.0 mmol) and 1,6-hexanediol (HDO) (11.8 mg, 0.10 mmol), were charged within a 25 mL round-bottom flask, cycled with nitrogen and subsequently dissolved in 5 mL of degassed dichloromethane (CH2Cl2). Then, a 1.0 wt% CH2Cl2-containing solution of trifluoromethanesulfonimide (HNTf2) (2.811mg, 0.010mmol) was added. The mixture was stirred for 68 h at 25 °C. After that, 5 mL of CHCl3 were added to the reaction mixture, and the polymer precipitated into methanol (90 mL). The precipitate was collected via centrifugation. The polymer PCL was obtained as a white solid (428 mg).

Synthesis of Segmented Copolymer

For T-50: T-0 (75 mg, 3.7 mmol) and PCL (75 mg, 4.1 mmol) were charged within a 10 mL round-bottom flask, cycled with nitrogen, and subsequently dissolved in 1.5 mL of degassed CHCl3. Then, a 0.5 wt% CHCl3-containing solution of hexamethylene diisocyanate (HMDI) (1.30 mg, 7.8 mmol) was added. The mixture was stirred for 190 h at 50 °C. The polymer was precipitated into methanol (80 mL). The precipitate was collected via centrifugation. The polymer T-50 was obtained as a dark blue solid (144 mg). The remaining BCPs were obtained by changing the weight fraction of PCL and/or using TT-0.

Preparation of Substrates for Mechanical Testing

Glass slides, cut into squares (1 in × 1 in) with a diamond-tipped scribe, were used as substrates for the polymer thin films. The slides were thoroughly cleaned in an ultrasonic bath in the following sequence of 10 min steps: powdered Alconox detergent dissolved in DI water, DI water only, acetone, and then IPA. After that, the slides were dried with compressed (house) air and then treated with plasma (30 W) for 5 min at a base pressure of 200 mTorr of air to remove residual organic debris and improve surface wettability.

Preparation of Films

Solutions of BCPs in CHCl3 (10 mg mL^{-1}) were prepared and allowed to stir overnight. Prior to use, all solutions were slightly heated (15 s) with a heat gun to promote dissolution of the polymer; the solutions were then filtered with 0.45 μm PTFE filters, immediately after which they were spin-coated (Headway Research PWM32) onto the cleaned glass substrates at 1000 rpm (ramping at 500 rpm s^{-1}) for 120 s. These conditions produced films of thicknesses ranging

from 100 to 150 nm as determined by profilometry (Dektak 150 Surface Profiler).

Testing of Mechanical Properties

We examined cracking behavior of thin film using a linear actuator and optical microscopy. Spin-coated thin films were removed from plasma-treated glass substrates and floated on a water surface. The films on water were transferred to stretchable PDMS (Sylgard 184, Dow Corning) substrates. PDMS was prepared according to the manufacturer's instructions at a ratio of 10:1 (base:crosslinker) and cured at room temperature for 36 to 48 h prior to use for mechanical testing. For our stress-strain curves, we use the film-on-water technique previously described by Kim and coworkers.[28,29]

Measurement of Field-Effect Mobility

Highly doped n-type Si wafers (0.001-0.005 Ω-cm) with 300 nm of thermal oxide were sonicated for 10 min each in detergent solution (2% Alconox in deionized (DI) water), DI water only, and isopropyl alcohol (IPA). The substrates were then treated with plasma (30 W) for 5 min at a base pressure of 200 mTorr, then placed in a 0.33 vol.% solution of octadecyltrichlorosilane (OTS) in cyclohexane for 18 min. Samples were rinsed with cyclohexane and then sonicated for 10 min in chloroform (CHCl3) before spinning a 10 mg/mL solution of PDPP-b-PCL in CHCl3 at 1500 rpm for 30 seconds. Samples were annealed at 100 $^\circ$C for 1 h. 40 nm thick Au electrodes were then thermally evaporated with a length of 1000 m and width of 30 μm. Samples were tested on a Keithley 4200.

2.5 Acknowledgements

Chapter 2, in full, is a reprint of material as it appears in: Chapter 2, in part, is a reprint of material as it appears in: Sugiyama F, **Kleinschmidt AT**, Kayser LV, Alkhadra MA, Wan JMH, Chiang ASC, Rodriquez D, Root SE, Savagatrup S, Lipomi DJ. Stretch-able and Degradable Semiconducting Block Copolymers. Macromolecules 51, 5944-5949, doi:10.1021/acs.macromol.8b00846 (2018). The dissertation author was second author of this paper.
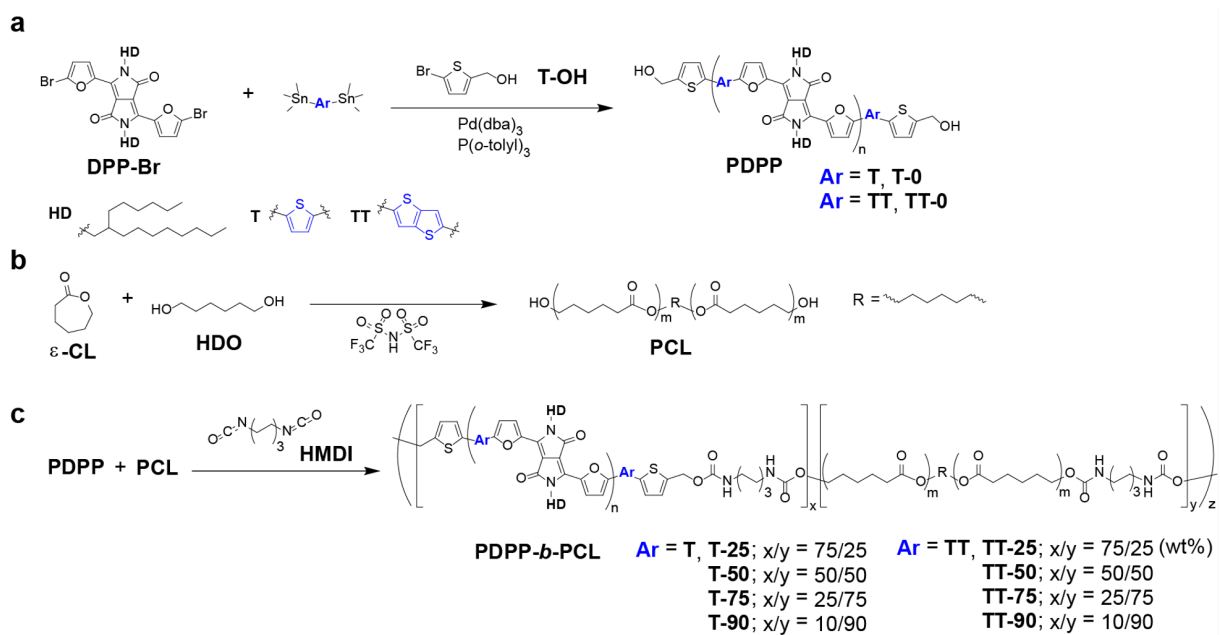
Figure 2.1: Synthetic strategy for BCPs containing DPP-based polymers and an aliphatic polyester. (a) Stille coupling polymerization of DPP-Br, stannane compound, and end-modifier. (b) Ring-opening polymerization of ϵ-caprolactone (ϵ-CL) with HDO. (c) Synthesis of BCPs with di-isocyanate linker.
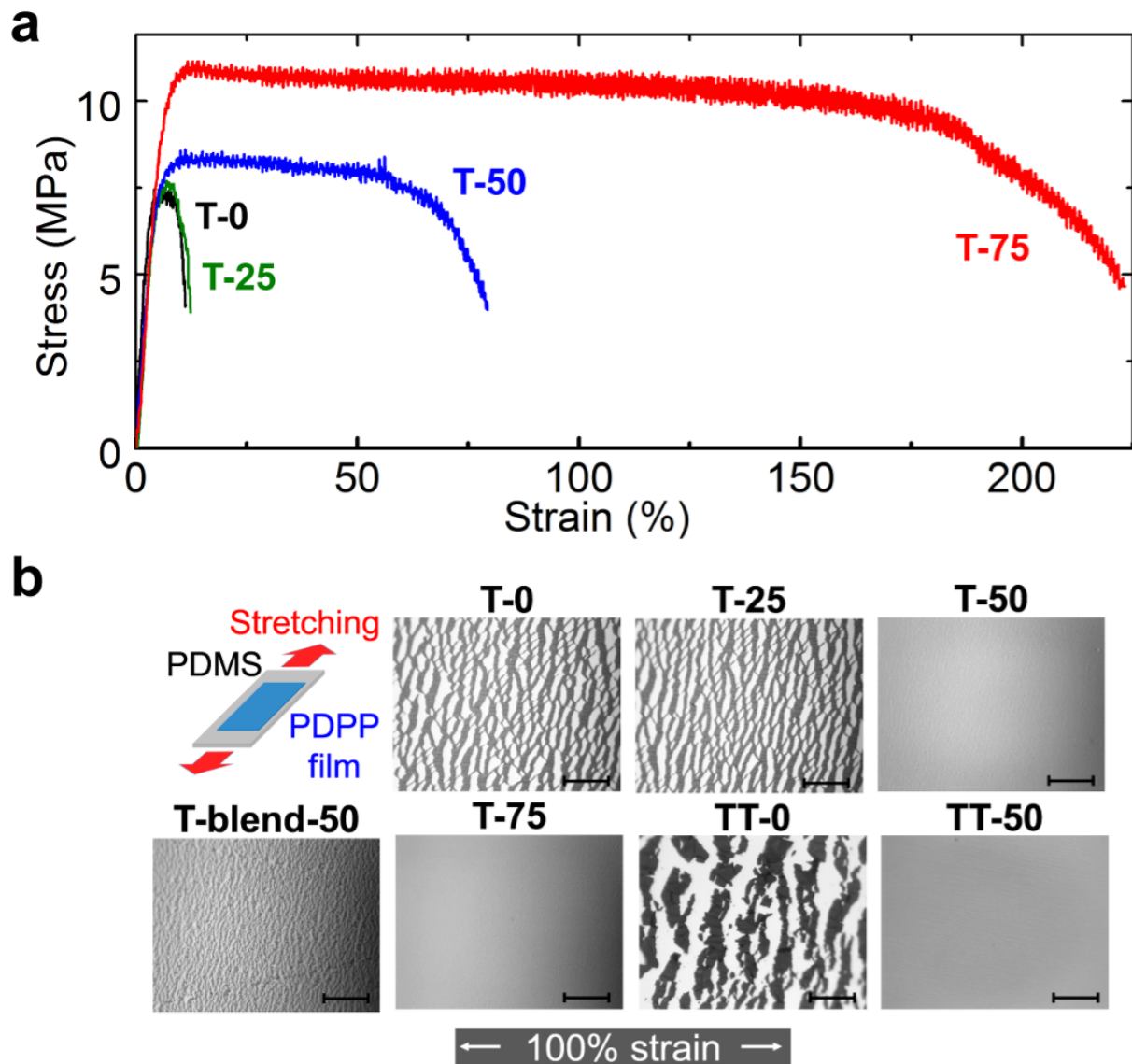
Figure 2.2: (a) Determination of the effect of PCL content in PDPP-b-PCL on mechanical properties. Stress-strain curves were obtained from films suspended on water. The photographs illustrate fracture be-havior, scale bar, 1 cm. (b) Optical micrographs of the cracking behavior of BCP and blend films on PDMS at 100% strain, 100 cycles, scale bar, 500 μm.
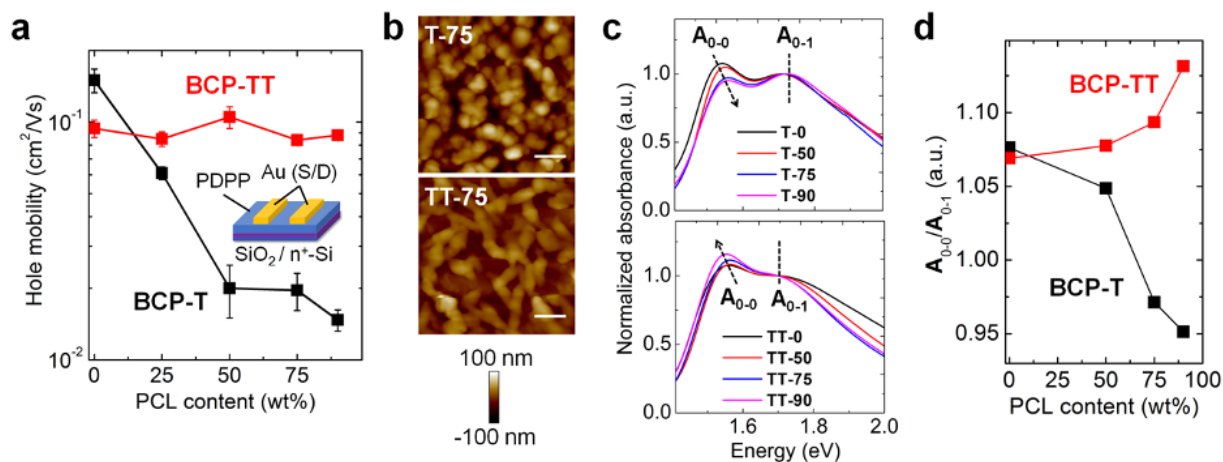
Figure 2.3: Characterization of electronic performance and morphology. (a) Schematic illustration of OFET structure and relationships between charge-carrier mobility and PCL content, standard deviations of three distinct measurements. (b) AFM height images of thin films after immersion in 0.5 M NaOH solution, scale bar, 300 nm. (c) UV-vis spectra showing the absorbance of BCPs thin films with different PCL content after annealing at 100 °C for 1 h, normalized to the A0-1 peak, (d) Relation-ship between relative heights of vibronic peak (A0-0/A0-1) and PCL content.
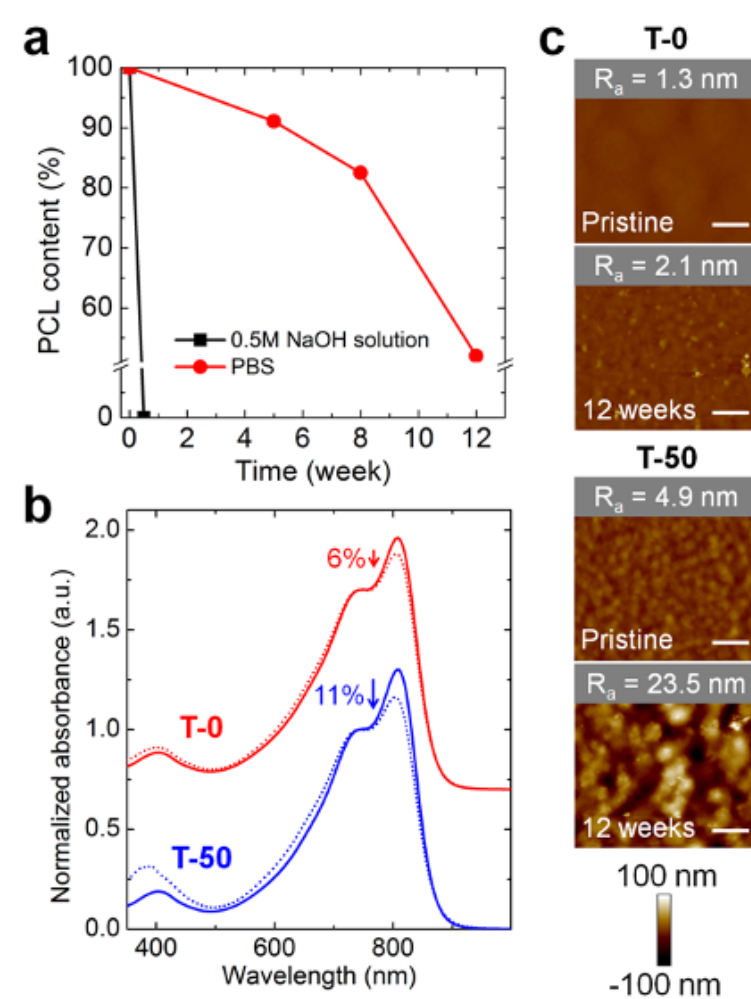
Figure 2.4: Characterization of BCP-films degradability. In vitro degradation of a T-50 thin film for different immersion times in PBS at 37 °C and in 0.5 M NaOH solution at 25°C. (a) Plot of residual PCL over time, (b) Normalized UV-vis spectra of T-0 and T-50 in chloroform for pristine films (solid line) and after 12 weeks of immersion in PBS (dotted line), (c) AFM height images of thin films before and after 12 weeks of immersion in PBS. Ra is the average surface roughness of the scanned area, scale bar, 1 μm.

Chapter 3

Decoupling Planarizing and Steric Energetics to Accurately Model the Rigidity of π-Conjugated Polymers.

The π-conjugated backbone of semiconducting polymers gives rise to both its electronic properties and its structural rigidity. However, current computational methods for understanding the rigidity of polymer chains fail in one crucial way. Namely, the standard method—the torsional scan (TS) method—cannot decouple energy related to electron delocalization from energetic effects arising from nonbonded (i.e., steric) interactions between adjacent aromatic monomers. This failure results in an overestimation of the energy associated with steric clashing and underestimation of energy associated with electronic delocalization. The overestimation of steric clashing arises because nonbonded energies are also counted through other modeled interactions (e.g., van der Waals interactions). Thus, conventional models lead to significantly

38

reduced planarization forces within the backbone (e.g., an overly twisted chain) because non-bonded forces are double counted. Here, we describe a method, "isolation of delocalization energy" (DE), to decouple the delocalization energy from the energy due to nonbonded interactions and to accurately understand the rigidity of any arbitrary conjugated material. In simulations of chains in the solid phase, adjacent monomers in three model polymers (P3HT, PTB7, and PNDI-T) were significantly more coplanar when using the DE method compared to the TS method. Likewise, the DE method showed torsional energy with up to 4.53 kJ/mol greater accuracy, relative to quantum mechanical calculations, when compared to a conventional torsional scan. The barrier to torsion and distribution of torsional angles for all three polymers were also determined to be more precise when calculated using the DE method.

3.1   Introduction

The backbone structures of π-conjugated polymers differ dramatically from those of polymers with saturated backbones. These polymeric semiconductors are generally composed of a backbone consisting of aromatic and/or heteroaromatic rings bonded to one another.[162,163] Charge transport in these conjugated structures is enabled by delocalization between overlapping π-orbitals,[164–166] which gives rise to the band structure.[167] Electronic delocalization is generally energetically favorable, resulting in highly planar polymer chains.[168–170] The semiconducting behavior of these π-conjugated materials in particular has given rise to a myriad of device applications, from organic transistors[171] and solar cells[172] to chemical sensors.[173] Due to their mechanical robustness and synthetic tunability, organic electronic devices fabricated from conjugated polymers have many advantages over their inorganic counterparts. In particular, polymers with the "donor-acceptor" motif—in which electron-rich and electron-poor monomer residues al-

ternate along the backbone—can achieve low bandgaps and high mobilities. Furthermore, this

"push-pull" effect further drives coplanarity of adjacent monomers.[174,175] Electronic delocaliza-

tion between adjacent monomers is thus a defining characteristic of conjugated polymers.[176,177]

Computational modeling of conjugated polymers potentially offers a high-throughput method of

analyzing relationships between the structure of the individual chains and the morphology in

the solid state. In such models, the ability to predict the rigidity of the backbone depends on

accurate determination of the energy of electronic delocalization between adjacent monomers,

a task that is not trivial. Typically, the energy is calculated by means of the conventional torsional

scan (TS) method, in which the torsion between adjacent monomers is steadily adjusted and

the total energy is calculated through a quantum mechanical (QM) method at each torsional

value.[178,179] The TS method has become standard to model and understand the rigidity of con-

jugated polymers.[180–182] However, the TS method returns both the energy related to dihedral

delocalization, along with the energy related to nonbonded energy (here, primarily steric inter-

actions). Nonbonded energy nearly always increases at planarity due to steric clashes between

atoms brought into close proximity (i.e., as in the eclipsed conformation in a Newman projection).

Thus, nonbonded energy acts to counter (and sometimes overwhelm) the favorable energy of

electron delocalization. Additionally, the TS method is typically the only part of the calculation

of the total energy capable of accounting for the energy related to electronic delocalization. On

the other hand, nonbonded forces also arise from other parts of the calculation (e.g., Lennard-

Jones interactions).[182–184] The usual result of this conventional approach is an underestimation

of the rigidifying planarization force and an overestimation of the nonbonded forces (i.e., the

nonbonded forces are double counted). Additionally, the domination of the nonbonded forces in

some torsional scans makes it difficult or impossible to measure the fundamental energy barrier

to torsion.[179] These inaccuracies prevent conjugated polymers from being accurately modeled and compared, especially for those with different backbone structures. Any model in which the rigidity of the polymer backbone is important (e.g., charge transfer, mechanical properties, film morphology, solvent interactions) suffers as a result of the inability to treat the energy due to delocalization by itself. To address the inaccuracy with which conventional approaches account for the total torsional energy in conjugated polymers, we developed a method to determine the energy solely related to electronic delocalization. We term this method the "delocalization energy isolation method" (DE). Quantum mechanical data is used in both the conventional torsional scan method, data we refer to as QM-TS, and the delocalization energy method, data we refer to as QM-DE. The quantum mechanical data were incorporated into a force field for molecular dynamics simulation based the ubiquitous OPLS force field (commonly used to model organic liquids and materials).[60] The force field utilizing the torsional scan method is termed OPLS-TS, and the force field optimized with the delocalization energy isolation method is termed OPLS-DE. The DE method is described in Figure 3.1. First, a conventional torsional scan, based on the seminal work by Marcon and Raos,[179,185] was conducted by optimizing the geometry of the planar conformation of the dimer. Then, we calculated the potential energy curve as a function of increasing torsion angle between the monomers (Figure 3.1a). The total energy from these calculations has contributions from both electronic delocalization, Edelocalization, and nonbonded interactions, Enonbonded. We then sought to separate Enonbonded from Edelocalization to extract the energy due solely to delocalization. To approximate Enonbonded, an identical torsional scan was performed on a variation of the structure, where one monomer was dually hydrogenated (Figure 3.1b). The placement of a hydrogen atom in the π-system (specifically, at the point of attachment with the aromatic monomer) interrupts the delocalization of electrons.

Thus, the calculated energy from the hydrogenated dimer is taken as being primarily due to nonbonded forces in the system, Enonbonded, plus an additional energy related to the unphysical placement of the hydrogen atom in the π-system, Ehydrogenation. The energetics from the placements of the second hydrogen atom should remain relatively constant for all torsional angles. Finally, the molecule was modified such that the hydrogenated monomer was replaced by a methyl group (Figure 3.1c). In this methyl group, one of the hydrogen atoms is placed in the same perpendicular position as in the hydrogenated dimer. The other two hydrogen atoms are oriented in the same directions as the carbon atoms attached to the (2,5) positions of the unsaturated monomer. The position of the hydrogen atoms thus mimics the position of the atoms in the hydrogenated dimer. The methylated monomer thus provides an approximation of the energy of the placement of the unphysical hydrogen atom, Ehydrogenation. The total energy of this methylated monomer is subtracted from the total energy of the hydrogenated dimer to provide an estimation of the total nonbonded energy, Enonbonded. The nonbonded energy can in turn be subtracted from the energy of the pure dimer to obtain an estimation of the delocalization energy. In doing so, both the energy of delocalization and nonbonded energy in the system are isolated. We had three goals in attempting to account for these nonbonded interactions: accuracy, universality, and understandability. Of these goals, the most fundamental is accuracy, because accurate understanding of the rigidity of a conjugated polymer chain will allow for better understanding of charge transport and mechanical properties. Indeed, previous work has shown that the rigidity of the semiconducting backbone is closely related to the charge transport of a polymer chain,[170,186] while other work has shown a correlation between elastic modulus and chain rigidity.[187–189] The next goal was to build a universal model that could be used to characterize any conjugated polymer. While early studies with conjugated polymers tended to

42

focus exclusively on poly(3-alkylthiophene) (P3AT) derivatives, the field is no longer dominated

by a single polymer.[190] Instead, the emergence of donor–acceptor (D–A) polymers has resulted

in the development of a diverse array of conjugated polymers applied to all areas of organic

electronics.[191] For example, families of poly(diketopyrrolopyrrole) (PDPP), poly(naphthalene

diimide) (PNDI), indacenodithiophene (IDT), and poly(benzodithiophene) (PBDT)-based back-

bone structures are all commonly used in organic transistors and solar cells.[192–195] Therefore,

computational models must be able to accurately handle a wide (and growing) range of polymer

structures, and to allow for the comparison between polymers. An additional benefit of such

universality is that advancements in computational modeling are also applicable to fused-ring

electron acceptors, which have dominated recent organic solar cell literature due to the high

power conversion efficiencies of the devices they enable.[196] Finally, we aimed to develop a

method that generates easily understandable data to guide both physical experiments and the

rational design of conjugated polymers. With a better understanding of the planarizing forces in

a polymer backbone, the relationship between polymer planarity and both charge transport and

dissipation of mechanical energy can be better understood.

3.2   Results and Discussion

QM Calculated Nonbonded and Delocalization Energies

We use the DE method to estimate the nonbonded and delocalization energies of three

polymers—poly(3-hexylthiophene) (P3HT), polythieno[3,4-b]-thiophene-co-benzodithiophene

(PTB7), and poly(naphthalene diimide) with a single bridging thiophene (PNDI-T)—as shown

in Figure 3.2. The delocalization energy determined by the DE method is then compared to the

energy calculated from the TS method, or the total energy in the DE method. We find that the isolated delocalization energy, as determined by the DE method, differs significantly from the total energy obtained from the TS method. For all three polymer models, the nonbonded energy increases most significantly when the monomers are coplanar with one another. There are two major consequences of this result. First, the energetic barrier to rotation about the polymer backbone is underestimated across all three polymers. The maximum in nonbonded energy occurs when the backbone is completely planar, which is also the conformation resulting in the minimum of the energy related to delocalization. In contrast, we find that the nonbonded energy is negligible near perfect orthogonality ($90°$ of dihedral torsion), while the energy associated with delocalization is at its maximum. Overall, the competing delocalization and nonbonded interactions result in smaller total energies. Second, the energies of the TS method are at times dominated by the nonbonded forces. For PNDI-T, the nonbonded energy skews the torsional scan so much that the energy is almost entirely related to conformational effects arising from steric hindrance. This is a critical point, since combining the torsional scan energy with an additional van der Waals term, such as a Lennard-Jones potential, will result in significant overestimation of torsion in the polymer. Notably, this increased torsion is due to the polymer undergoing antiplanarization from the nonbonded forces, with little to no compensating planarization force due to delocalization. These two findings underscore that the standard practice of using the torsion scan method in concert with van der Waals interactions will adversely affect the predicted electronic and mechanical properties of the polymer. Our result also explains why previous attempts to simulate conjugated polymers have been fraught with difficulty, with the results obtained by the conventional TS method for some polymers being so problematic that they are not pursued.[179] As a specific illustrative case, consider PTB7, which has two regioisomeric

monomer types: one with the fluorine atom pointed away from the benzodithiophene (F-out) and the other with the fluorine atom pointed toward the benzodithiophene (F-in). During the synthesis, the orientation of the fluorine-substituted thieno[3,4-b]thiophene is statistical (essentially random). The two regioisomers have similar electronic structures, however, and thus the rigidity of the two regioisomers predicted from electronic delocalization alone should also be similar. Nevertheless, the TS method results in diverging energies for the two different configurations (Figure 3.2c and 2d). Previous studies of PTB7 have resulted in such divergent characterizations of torsional energy that the two conformations were treated entirely differently, despite their nearly isoelectronic structure.179 The divergent energies given by the TS method therefore do not reveal the true rigidifying energy of PTB7. In PTB7, the underlying fundamental rigidifying energetics are obscured by steric forces. When the F-out dimer is considered, the presence of the sulfur results in a smoother surface: i.e., there is no hydrogen atom protruding from a carbon to generate an unfavorable steric interaction with the benzodithiophene unit. Thus, the PTB7 F-out coupling motif results in the lowest nonbonded energies of all three polymer systems considered. There is a slight increase in total energy in the TS method at planarity, and the energies of delocalization and total energy are approximately equal. In contrast, when considering the F-in dimer, the torsional scan is significantly affected by the nonbonded energies. For example, when the fluorine substituent and the sulfur atom of the benzodithiophene are on opposite sides, the difference in energy between a 0° and 90° dihedral angle is approximately 16 kJ/mol. When the fluorine substituent of the thieno[3,4-b]thiophene unit and the sulfur atom in the benzodithiophene ring are adjacent, the difference in energy between 0° and 90° of torsion is only approximately 7.5 kJ/mol. Given that this energy determined by the torsional scan is the only force in a simulation that will push the polymers towards planarity—and that nonbonded forces

are already separately accounted for (e.g., through Lennard-Jones potentials)—the TS method will result in a highly twisted polymer. Note that this effect is seen irrespective of the fact that every "F-in" coupling results in an "F-out" coupling with the benzodithiophene of the adjacent monomer (to the right of the parenthesis, as drawn). Nevertheless, the 50% of the dihedral interactions are of the F-in type, and will thus contribute to twisted structures with highly reduced planarizing forces.

Comparison of the force field and QM dimerization energies.

We then fit both the quantum mechanical energies from the torsional scan (QM-TS) and quantum mechanical energies of the estimated pure delocalization energy (QM-DE). We used the dihedral style used by a conventional OPLS force field to facilitate use in MD or Monte-Carlo simulations. In this particular case, we compared the QM and force field energies as a function of torsional angle (Figure 3.3) to determine how well the methods allow for simple approximation of quantum mechanical energy. For P3HT, PNDI-T, and the F-in conformation of PTB7, complete breaking of planarity (i.e., a 90° torsional angle) was under-penalized in terms of calculated energy when using the OPLS-TS method. After fitting both the QM-TS and QM-DE data to an OPLS-style dihedral model, differences between the two models were similar to those observed in the unfit (Figure 3.2) delocalization energies. The largest differences were seen in PNDI-T, where at nearly all dihedral angles, the expected differences in energy exceeded 5 kJ/mol. Additionally, we found that the energy of the dimer obtained from the TS method was significantly higher near planarity, due to the conflating of the steric hindrance and electronic delocalization noted previously. Similar behaviors were observed in the F-in structure of PTB7, and to a lesser extent, P3HT. The F-out conformation of PTB7 was the lone exception, for which the differences

between the TS and DE methods were low for all torsional angles. To test the accuracy of the DE characterization of inter-ring torsion, dimers were placed in vacuum without any torsional barrier and allowed to freely rotate. The relative accuracy of the energy difference with respect to the dihedral angle for randomized configurations of each dimer is shown in Figure 3.4. The accuracy of the force fields is determined by comparing torsional force field energies derived from the DE and TS methods (OPLS-DE and OPLS-TS) to quantum mechanical calculations at the RI-MP2 scale. The comparison was done to measure which force field best resembles the energies of the quantum mechanical method, as quantum mechanical methods are the best approximation of the energies of various conformations. We note that while we used RI-MP2, the DE method described here can be used to approximate any quantum mechanical method. Encouragingly, we find that the DE method showed greater relative accuracy across all polymers when compared to the torsional scan method. Our results from Figure 3.2 show that the torsion characterized by the DE method is more accurate than the torsional scan method as steric hindrance leads to increased deplanarization. For example, for the F-out structure of PTB7, the TS and DE methods gave similar energetic values. Thus, there was only a relatively small increase in accuracy (0.33 kJ/mol) when using the OPLS-DE force field. In comparison, for PNDI-T, the TS method resulted in significantly different energies when compared to the OPLS-CP method. Accordingly, PNDI-T sees the largest improvement in accuracy compared to QM. For highly sterically hindered configurations (i.e., P3HT, PNDI-T, and PTB7 (F-in)), the overall improvement in accuracy of the OPLS-CP force field ranged from 1 kJ/mol to 4.5 kJ/mol. Notably, these average values include comparisons between dimer conformations in which the dihedral angle (and thus torsional energy) was highly similar. As such, improvements to the torsional energy result in little change in accuracy of energy between the two conformations, depressing the overall im-

provement in accuracy. The OPLS-DE model differs from the usual total energy from torsional

scan model in that it aims to isolate nonbonded steric forces from the delocalization forces, thus

accurately describing the torsional barrier. Therefore, the greatest improvement in accuracy

between the OPLS-DE method and the torsional scan method should occur when comparing

a planar dimer and an antiplanar dimer, where these energies are most unfavorably coupled.

Indeed, for all modeled polymers except PTB7 (F-out), we show that the largest improvement

in relative accuracy occurs when comparing a planar ($0°$ or $180°$ torsional angle) dimer and

an antiplanar ($90°$ or $270°$ torsional angle) dimer (Figure 3.4). In contrast, the OPLS-TS force

field performs best when the dimers have similar torsional angles (i.e., the energy difference

between dimers is relatively low), where the relative energy are more sensitive to non-torsional

energies of the conjugated polymer system (e.g., Lennard-Jones interactions, harmonic bond

lengths). The differences in energy are on average quite small as well when torsional angles

are similar, within the standard error of quantum mechanical methods. The energetic differ-

ence between planar conformations and other conformations is crucial to accurately define the

conformation of the polymer. Therefore, our results show that for arbitrary configurations, the

OPLS-DE force field more accurately describes the motion of conjugated polymers relative to

the torsional scan method. The torsional barrier to the rotation of each polymer (i.e., energy of

planarization) was calculated using both the DE (blue) and TS (red) model in Figure 3.5. We

calculated the torsional barrier in three different ways for both models. For the first two methods,

we compared the calculated energy at perfect antiplanarity ($90°$ dihedral angle) and perfect pla-

narity ($0°$ or $180°$). The $0°$ dimer calculation is referred to as "$90°$-$0°$" (backslash-style hatching),

while the $180°$ dimer calculation is labeled "$90°$-$180°$" (frontslash-style hatching). For polymers

with high steric forces, one might wish to avoid the regions in which steric clashes dominate

the torsional scan, and simply take the difference between the maximum and minimum of the torsional scan. This calculation is referred to as "Max-Min" (solid bars) in Figure 3.5. In planar (0° and 180°) conformations, electrons should be able to delocalize as easily in one conformation as the other. Therefore, we expect near-identical energetic minima at these torsional angles. Similarly, we expect the energetic maxima to be located at perfect antiplanarity (90°). Intuition thus dictates that all three calculations of planarization energy should be nearly identical if the model accurately represents the delocalization forces. The DE method gave highly similar energies (only varying by 1.5 kJ/mol) for all calculation styles when applied to each polymer, with the exception of the PNDI-T 90°-0° measurement (which varied by 3 kJ/mol). For all the polymers modeled, the OPLS-CP Max-Min value was within 0.1 kJ/mol of either the 90°-0° or 90°-180° calculation. This precision indicates that the maximum calculated value of the torsional barrier was always at or close to perfect planarity, while the minimum value was always at or close to perfect antiplanarity. A very slight difference between the 90°-0° and 90°-180° calculations exists for all polymers in the OPLS-CP model (±1.5 kJ/mol), with the exception of PNDI-T. PNDI-T had a slightly larger mismatch between the 90°-0° and 90°-180° calculations, yet both calculations remained within 15% of the overall calculated energy. We attribute the mismatch to the massive steric forces within this conformation of PNDI-T, which created some noise within the calculation of the delocalization force. In comparison, the TS method can give significantly different values for each calculation of the torsional barrier. The TS method gave a large spread of energetic calculations of the torsional barrier, with wide ranges of up to 100 kJ/mol. For P3HT, the 90°-0° energy was nearly half that of the 90°-180° energy due to steric hindrance, likely caused by clashes between the proximate hydrogen and sulfur atoms. Similarly, the F-in and F-out structures of PTB7 showed torsional barriers that differed by up to 10

49

kJ/mol. In this case, the Max-Min method appeared most effective, with relatively similar values for the two configurations of PTB7. However, for PNDI-T, all methods of calculating the barriers using the torsion scan method gave significantly different values, with the Max-Min calculation appearing the least effective (i.e., the most inaccurate in determining the fundamental energy of the system). For the $90°$-$0°$ calculation, the $0°$ value was significantly higher than the antiplanar conformation, resulting in the lone negative value. The $90°$-$180°$ value of the planarization energy was relatively small, even comparable to that of P3HT, despite being a donor–acceptor polymer with significant differences in electronegativity between the monomers, a feature associated with more rigid polymers due to the push-pull effect. The differences in the Max-Min value were particularly large—over 50 kJ/mol—due to the calculation between the energetic maximum, where steric clashes are present, and the minimum, where the steric clashes no longer occur. We end our analysis of Figure 3.5 by considering how the calculated torsional barriers could be interpreted for experimental design. The energies from the TS method are not indicative of the overall rigidity of the resulting polymer system. P3HT is labile (i.e., has a low energetic barrier to torsion) in the torsional scan method, especially if the $90°$ - $0°$ method is used. The TS method would suggest that the fundamental rigidity of PTB7 is comparatively more rigid than P3HT. However, the extent of increased rigidity in PTB7 would be unclear, as the model suggests differences in the energetic barrier by up to 10 kJ/mol for the PTB7 F-out and F-in structures. For PNDI-T, how one interprets the fundamental rigidifying force of the polymer is defined by which calculation is used. If the $90°$-$0°$ method is used, we would expect the polymer to be rigid, but locked in the antiplanar configuration. If the $90°$-$180°$ method is used, we would expect the polymer to be, approximately, as labile as P3HT. Finally, if the Max-Min method is used, we expect a polymer chain with over triple the rigidity of the other polymers. In com-

parison, the DE method is more precise in its determination (and interpretation) of the rigidity of each polymer: P3HT (13 kJ/mol of planarizing energy) ≺ PTB7 (17 kJ/mol for both the F-in and F-out structures) ≺ PNDI-T (25 kJ/mol). These results correlate with the increasing disparity in electronegativity and increasing size of the π-system from P3HT to PTB7 to PNDI-T, which result in more rigid polymers. These results are consistent with experimental expectations, in particular the similarity of both PTB7 dimers, and the intuition regarding D–A polymer backbone rigidity.[202]

Large scale polymer morphology.

Molecular dynamics simulations of P3HT, PTB7, and PNDI-T were performed to determine how a change in torsional potential would affect the polymer morphology (Figure 3.6). These simulations predict what morphologies the polymer chains in the amorphous regions of each polymer would adopt when using the OPLS-DE force field compared to OPLS-TS. We found that the OPLS-DE force field resulted in differences in dihedral conformations adopted, as measured by inter-ring torsion, that were significantly closer to planarity across all three polymers (Figure 3.7). In P3HT, the simulations using both OPLS-TS and OPLS-DE resulted in a nearly Gaussian distribution of torsional angles. However, the center of the distribution was shifted closed to planarity when using the OPLS-DE method, resulting in a polymer with its most frequent torsional conformation at approximately $40°$ and the frequency of torsional angles steadily decreasing towards both $0°$ and $90°$. In contrast, the OPLS-TS characterization resulted in the most common torsional angle being at approximately $50°$, with a significantly higher preference for the polymer in a conformation of a complete break in conjugation ($90°$) than perfect planarity. We note that the OPLS-DE results are more consistent with previous computational

studies using quantum mechanical methods, which showed that the average torsional value of P3HT is approximately $30°$ - $40°$.[203,204] Interestingly, our own torsional scans show minima in total energy for P3HT at approximately 0-$10°$ and 20-$40°$. We thus posit that the torsional scan is excellent for predicting the ultimate distribution of the torsional angles, but a poor tool for understanding the fundamental energies of the system. In PTB7, the differences between the OPLS-DE and OPLS-TS models were smaller but still significant. The relative similarity of the two generated distributions can be attributed to the fact that half of the torsional angles in a PTB7 have the F-out conformation, for which we previously determined the TS method is relatively accurate (Figure 3.4). However, we find that the DE method for PTB7 shows a higher frequency of planar conformations ($<45°$) and lower frequency of high degrees of torsion ($>45°$). Similar to P3HT, the inclusion of a true planarizing force in the OPLS-DE method results a significantly more planar polymer chain, rather than one in which twisted conformations are more common. PDNI-T shows, by far, the clearest difference between the force fields derived from the TS and DE methods. The TS method results in a maximum frequency at approximately $70°$, with all torsional angles above $45°$ having large probabilities and very little probabilities for angles below $45°$. In contrast, the OPLS-DE distribution resembles a normal distribution centered around $40°$. The OPLS-DE model fits well with our current understanding of NDI polymers: while these polymers are often referred to as highly twisted, they do not present configurations that are nearly entirely antiplanar (as is suggested in the torsional scan model). Theoretical models[205] posit an energetic minimum around $40°$, consistent with the OPLS-DE results. Notably, torsional angles commonly above $45°$ would present a serious obstacle to π-stacking, which occurs to significant degree in NDI polymers.[206] These results underscore the superiority of the OPLS-DE model in accurately predicting the morphologies of conjugated polymers. Electronic properties

of polymer condensed phases. Finally, we aim to show how a more accurate prediction of poly-

mer morphology can better inform the electronic (i.e., charge transport) properties by analyzing

the morphological characteristics such as the conjugation length (i.e., the length of a film a

charge may delocalize without needing to undergo a charge hopping process). We calculate

the conjugation length as described in our previous work.184 P3HT has been shown to allow

charges to delocalize for torsional angles of up to $40°$, which we assume correlates with the

conjugation length; we thus use a $40°$ torsional angle as the cutoff for delocalization length for

all modeled polymers.[207] This assumption, of course, is an oversimplification of a complex elec-

tronic phenomena, and we emphasize that the maximum torsional angle for which charge can

still delocalize will vary from polymer for polymer. Rather than being a quantitative calculation,

this assumption is made as a proxy to estimate how electronic charge transport behavior varies

between polymers.

3.3 Methods

Force Field Parameterization.

QM calculations at the MP2 level of theory were used to measure the fundamental rigidity

of the conjugated polymer systems since MP2 has been shown to provide an excellent tradeoff

between accuracy and computational cost.179,180,197 Additionally, wavefunction-based meth-

ods such as MP2 can provide insights into underlying physics behind nonbonded interactions

not easily obtained by electronic structure density functional theory (DFT) calculations without

specialized corrections.198,199 Our strategy for generating QM data for both the TS and DE

methods (QM-DE and QM-TS) considers dimers—as opposed to oligomers—for several rea-

sons. First, the literature is varied regarding how many monomers outside of the central dihedral torsion, if any, are necessary to accurately reflect the energy.[168,185,200] Additionally, these monomers are typically kept consistently coplanar with the monomers undergoing torsion in computational models, whereas in reality torsion between all monomers will constantly shift as the conformation of the polymer evolves. As such, we focus entirely on the energetics associated with the local breaks in conjugation between adjacent monomers. Electronic delocalization between adjacent monomers is the largest source of delocalization energy, and is the focus here. QM/MP2 calculations were performed on three systems: 1) the fully conjugated dimers, 2) the hydrogenated dimers, and 3) dimers in which one of the monomers was replaced by a methyl group entirely (with the hydrogen atoms oriented similarly to the hydrogenated dimer). In all systems, the side chains were replaced with methyl groups to reduce computational time while maintaining electronic delocalization between the π-systems. For the hydrogenated dimer, two hydrogen atoms were added to the carbons at the (2,5) positions. For the carbon not bonded to the opposing monomer, the hydrogen was placed in a conventional configuration. For the centrally bonded carbon atom in the dimer, the hydrogen atom was placed orthogonal to the plane of the ring to block any π-orbital delocalization. For the methylated dimer, the hydrogens in the methyl group were manipulated to replicate the placement of atoms in the dimer. Two of the hydrogens were attached in the directions of the bonded carbon atoms in the dimer, scaled to be at equilibrium distance (1.08 Å). The third hydrogen was placed in the same location as the nonphysical hydrogen (as is in the hydrogenated dimer). The increased energy from the hydrogen not being placed in an equilibrium position was thus compensated by subtracting the energy of the methylated dimer from the energy of the hydrogenated dimer. A methyl group was used instead of the full monomer to minimize nonbonded interactions with the remaining

54

monomer while maintaining the energy related to the placement of the nonphysical hydrogen. The remaining energies were fit by an OPLS-style dihedral model, where the fitting was performed using a Levenberg-Marquadt algorithm. For the OPLS-TS model, the torsional scan energy was used to define the energy of backbone torsion in a conjugated polymer. To calculate the energy related to torsion between conjugated rings in the modified OPLS-DE force field, the isolated delocalization energy was used instead of the total calculated energy from the torsional scan.

Verification of Force Field Accuracy.

We obtained diverse unbiased structures of the gas-phase dimer for each conjugated polymer system by means of constant temperature (298K) constant volume (or NVT) MD simulations with LAMMPS,[201] where the critical torsional barrier between the dimer was omitted with the internal structure of each monomer constrained as rigid bodies. The conformation of the dimer was recorded every 100 ps, and the resulting structures used as input to a RI-MP2 QM calculation. The relative QM energies of each configuration was then compared to that obtained from our forcefield based simulations employing either the OPLS-TS or the OPLS-DE method. This comparison approximated how effective the OPLS-DE characterization was compared to a conventional torsional scan for modeling interactions between monomers. The energy difference between each dimer state was used rather than comparison to a refererence state to normalize any potential idiosyncrasies of a reference state (e.g., incorrect calculation of the energy at planarity).

Bulk-Phase Simulations and Characterization.

Simulations of each conjugated polymer were performed for 30 polymer chains, with each chain containing 30 monomers. The initial torsional angles between monomer rings were determined randomly using Boltzmann weighted probabilities of each torsional angle. Simulations were carried out between a model determined using the (1) OPLS-TS and (2) the OPLS-DE force fields. These simulations provided a comparison of the torsional characterization of each model on the morphology of the bulk phase. To determine the weighted probabilities, these polymer chains were placed in a simulation box by PackMol and run for 20 ps in the microcanonical (constant particles N, volume V and energy E or NVE) ensemble.[44] The equilibrium density of each system was then obtained by simulation in the constant pressure (1 bar) constant temperature (NPT) ensemble, where the system was allowed to equilibrate for 5 ns at 400 K, before being cooled to 300 K over 0.5 ns. Each system was then simulated in the NVT ensemble, heating from 400K – 800 K over 2 ns, held at 800 K for 5 ns, and then cooled to 300 K over 2 ns for proper equilibration. Finally, the long-term production dynamics were run for 10 ns in the NPT ensemble, with snapshots (atomic positions) of the corresponding bulk-phase morphology taken every nanosecond. For all NVT and NPT simulations, a Nosé-Hoover thermostat with a damping parameter of 100 fs was used. For all NPT simulations, a Nosé-Hoover barostat with a damping parameter of 1 ps was used.

3.4   Conclusion

The isolation of the delocalization energy allows for more accurate simulations of any arbitrary conjugated polymer when compared to the conventional torsional scan method. Three

model polymers—P3HT, PTB7, and PNDI-T—show simulated chain morphologies that are significantly more planar than the morphologies predicted using other methods. This increased rigidity along the polymer backbone results in significantly different predicted mechanical and electronic properties. We find that the DE method provides several major advantages over the conventional TS method. The first is the accuracy of the model, due to the separation of the delocalization and steric forces. The second is the highly generalizable methodology that can be used with any quantum mechanical method for any conjugated polymer. The third is the ability of the model to better inform rational design of new conjugated polymers (i.e., more accurate predictions of the mechanical and electronic properties from the predicted morphology). One of the primary difficulties in modeling the morphology of conjugated polymers has been accurately describing the inter-ring twists, which in turn govern the mechanical and electronic properties of the polymer.[209] The DE method improves upon our understanding of describing such torsional effects by more accurately elucidating how the energetics of a polymer backbone change with respect to dihedral angle. Likewise, with its generalizability to all conjugated polymers, the DE method offers a platform for high-throughput modeling of conjugated polymers. Therefore, the DE method is synergistic with advanced methods such as machine learning models, which can greatly increase the general accuracy of a simulation. However, with machine learning, the parsing of how the fundamental energies within the system relate to systemic changes (e.g., deplanarization) can become muddled if they cannot be decoupled.[209] The DE method improves upon this synergy by (1) decoupling energetics related to delocalization and steric effects and (2) providing a clear and direct understanding of how deplanarization can affect the energetics (and thus, morphology) of the polymer. However, the DE method only considers the interactions between adjacent monomers. A deeper understanding of how distant monomers

affect the rigidifying forces within the backbone may further improve the accuracy of the model and facilitate the simulation of conjugated polymers at larger domain scales (e.g., longer polymer chains, bulk morphology within a thin film). In turn, more accurate models over larger domain scales will enable more accurate predictions of mechanical (e.g., elastic modulus, yield strength) and electronic properties (e.g., conjugation length, charge transport in highly disordered polymeric materials) for device applications. Likewise, a better understanding of how fundamental energies govern the morphology of a semiconducting polymer can better inform experimental and rational design. For example, many previous studies have observed a trade-off between the electronic and mechanical properties when synthetically altering the structure of a conjugated polymer.[210,211] The morphology of a solid film governs both the electronic and mechanical characteristics. Therefore, more accurate simulations can offer guidance as to how to design new polymers for optimizing both properties simultaneously, or predict the optimal composition of polymer blends (e.g., within a bulk heterojunction). Additionally, the DE method is not limited to specifically π-conjugated polymers. While π-conjugated polymers were tested in this manuscript, this method should be effective for characterization of conjugated organic ligands in MOFs, small-molecule acceptors in organic electronics, and liquid crystal mesogens. By understanding the fundamental force governing conjugated morphologies, the behavior of conjugated systems can be better understood.

3.5 Acknowledgements

Figure 3.1: Overview of parameterization of the DE method. Initial torsional scans are performed (a) with a simple dimer (bi(3-methylthiophene)), rotating the dihedral angle through all possible configurations. The dimer is then hydrogenated (b), with one of the hydrogen atoms bonded to the carbon atom involved in the dimer bond. The C-H bond is typically perpendicular to the plane of the ring. An additional hydrogen is also added on the end of the dimer, i.e., on the carbon which would continue the chain in a polymer. This provides an estimation of the nonbonded energy of the dimer, as any energy due to electron delocalization between dimers is blocked by the hydrogen. Additionally, a version of the dimer where (c) one of the monomers is entirely replaced by a methyl group is used. In this structure, one of the hydrogen atoms on the methyl group is in the same location as in the hydrogenated dimer to control for any added energy caused by the unphysical hydrogen atom.
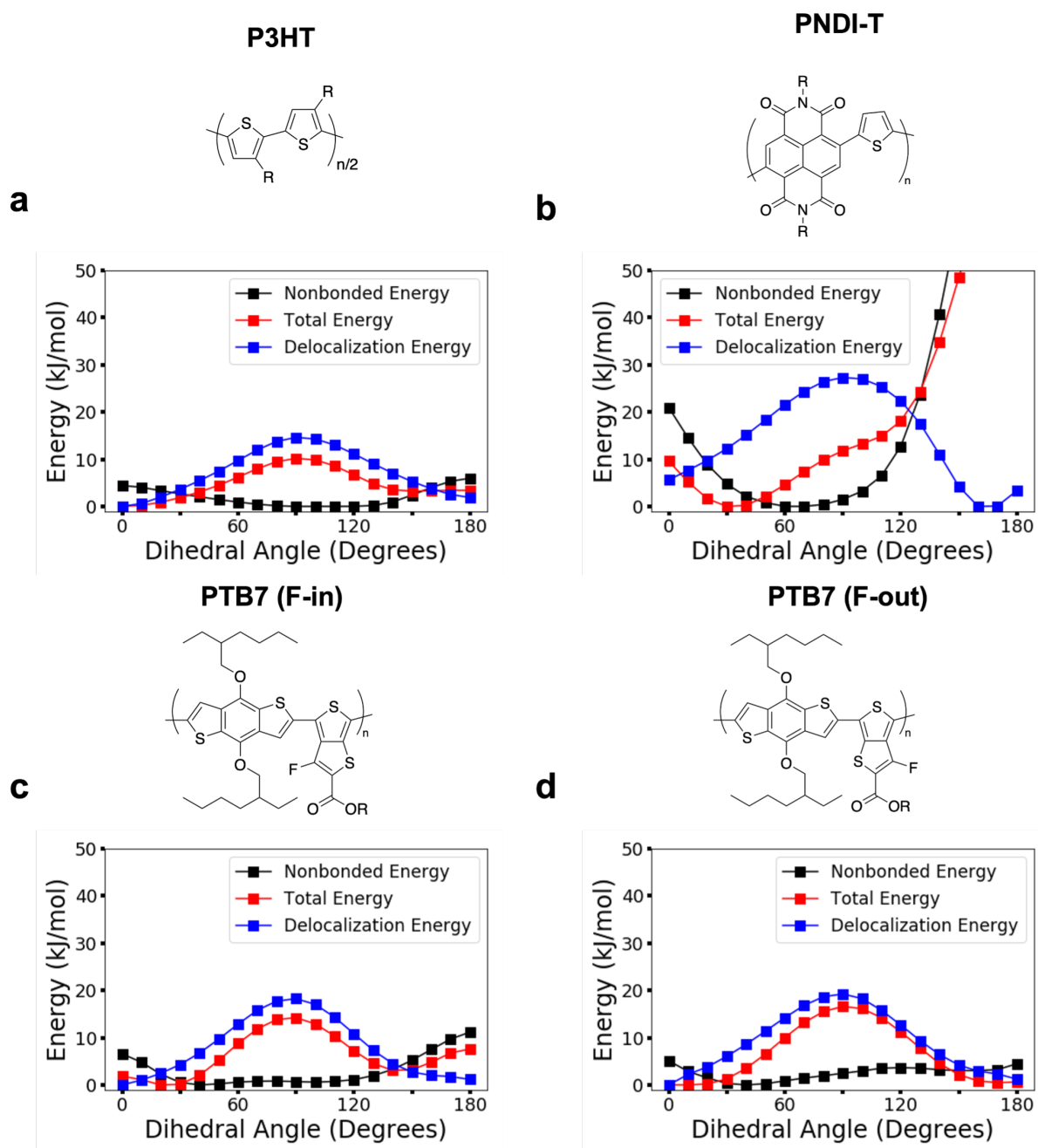
Figure 3.2: Estimations of the types of energy as used in the DE method, showing the pure delocalization energy (blue), nonbonded interactions (black), and total energy of the TS method (red). Notably, the minimum energy for all three types of energy is set to zero, so the energies are not purely additive. In all three polymers, nonbonded interactions (namely, steric hindrance) serve to destabilize the planar conformation. The energies are shown for (a) P3HT, (b) PNDI-T, (c) PTB7 with the fluorine on the interior ("F-in"), and (d) PTB7 with the fluorine on the exterior ("F-out").
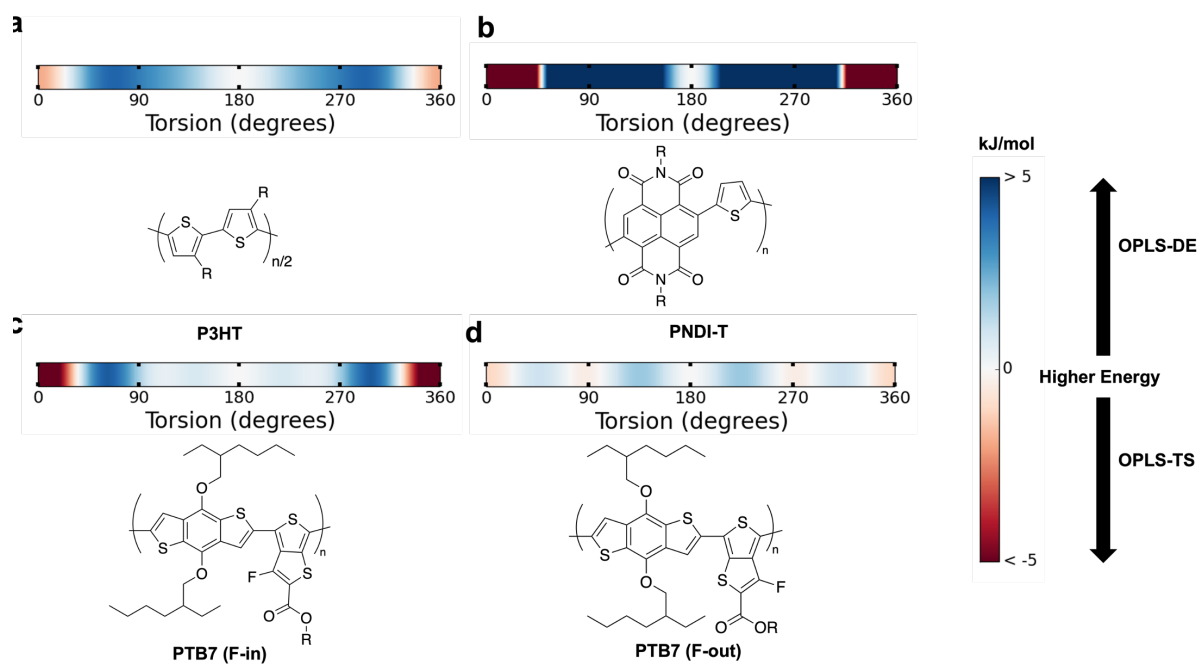
Figure 3.3: Difference in energy between the DE and TS methods for (a) P3HT, (b) PNDI-T, (c) the F-in conformation of PTB7, and (d) the F-out conformation of PTB7. Blue indicates that the DE method applies a higher energetic penalty to backbone torsion, while red indicates that the TS method applies a higher energetic penalty. Dark red or dark blue indicate differences that are ≥1 kcal/mol.
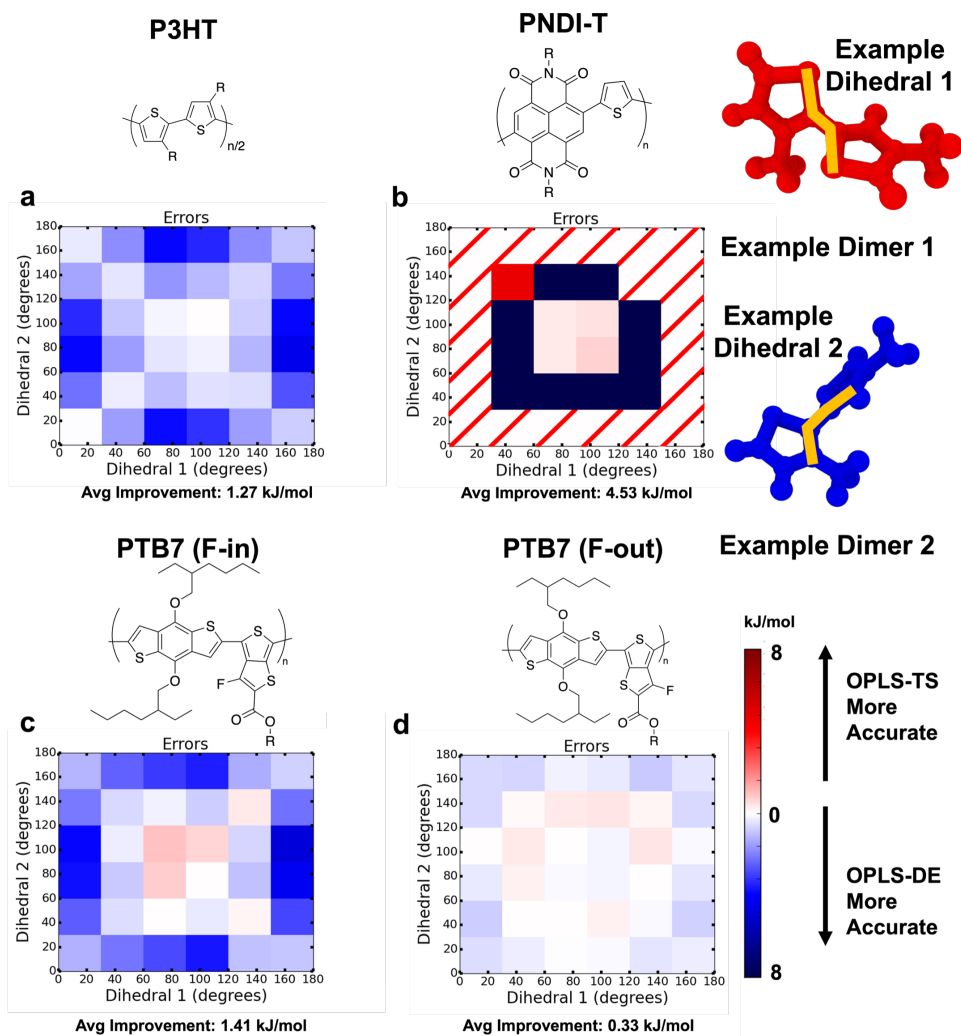
Figure 3.4: Relative accuracies the energy of torsion for (a) P3HT, (b) PNDI-T, (c) the F-in configuration of PTB7, and (d) the F-out configuration of PTB7. An example of two random conformations of P3HT are given, Example Dimer 1 and Example Dimer 2. For these two dimers, their central dihedral (Example Dihedral 1 and Example Dihedral 2) would be parameterized by OPLS-TS or OPLS-DE. The total energy difference as calculated by the quantum method, RI-MP2, is then used to compare the energy of the conformations. The quantum mechanical energy difference is then compared to the difference in energy calculated by the OPLS-DE and OPLS-TS force fields. Red indicates that the OPLS force field based on the TS method performs better, while blue indicates the OPLS-DE force field performs better. A red slash through a box indicates that no combination of dimers with those dihedral angles were tested.
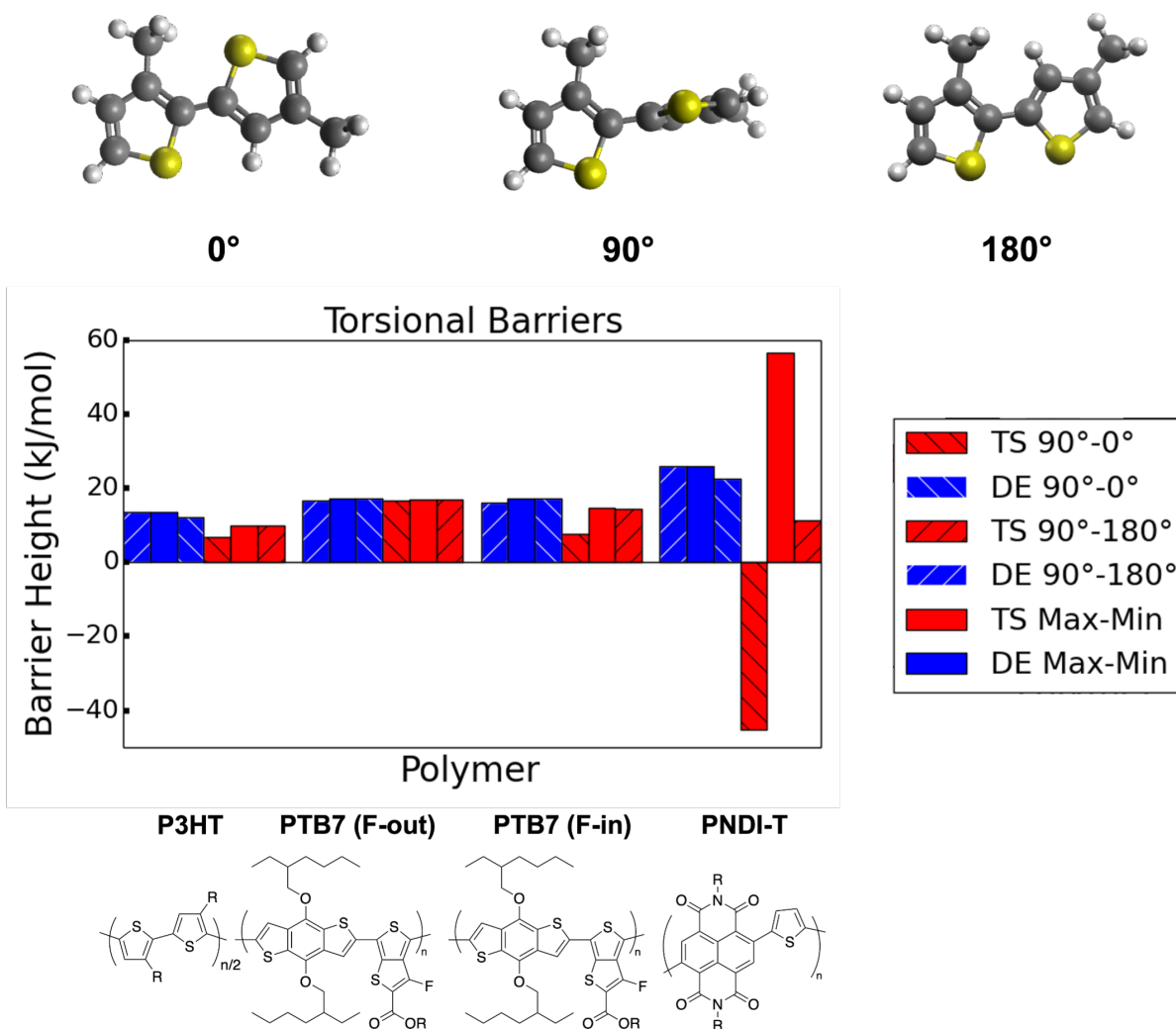
0°   **90°**   **180°**

Figure 3.5: Relative planarization energies of P3HT, PTB7 (F-in and F-out), and PNDI-T as determined using the DE and TS methods. The energy difference is estimated between the dimers with 0° and 90° of torsion ("90°-0°"), 180º and 90° of torsion ("90°-180°"), and the maximum and minimum values of the energy ("Max-Min").
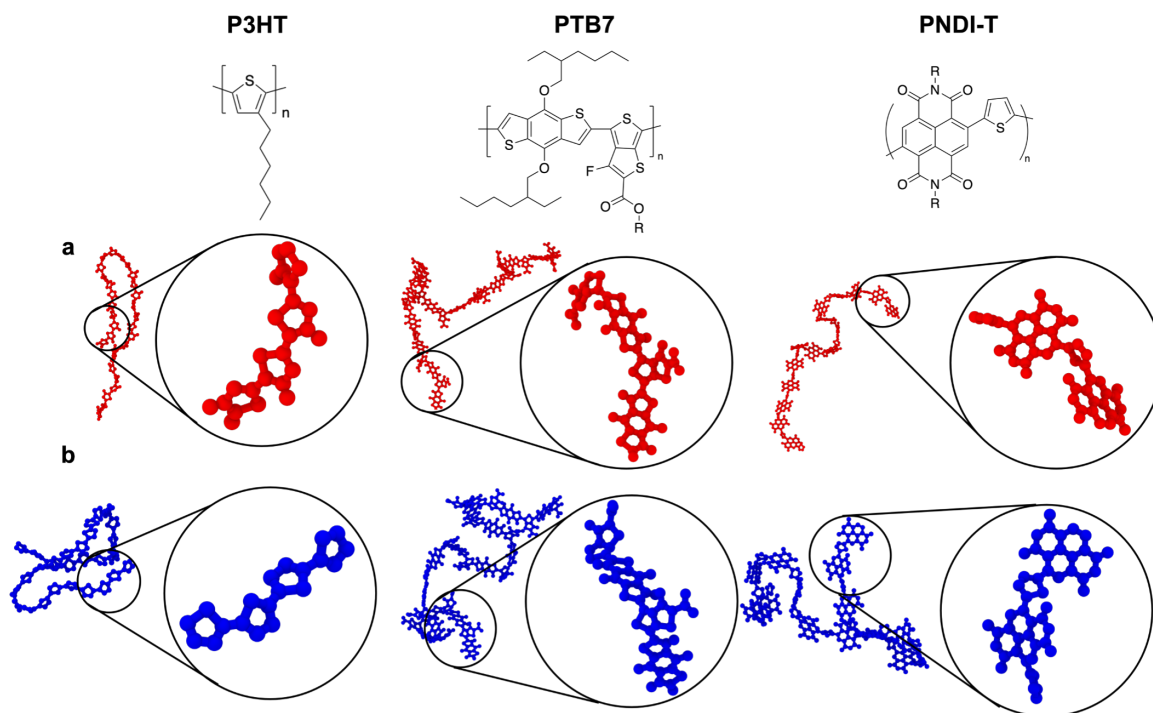
Figure 3.6: Visualizations of the morphology of a single chain for P3HT, PTB7, and PNDI-T. Side chains are removed to make torsional angles clearly visible. A zoomed-in image of first four monomers (as characterized in the simulation) is provided. The arbitrary images are representative of the general morphology. For all polymers, chains simulated using the OPLS-TS force field were less linear and more twisted (a) than those simulated using the OPLS-DE force field (b). This disparity is particularly apparent in the simulation of PNDI-T.
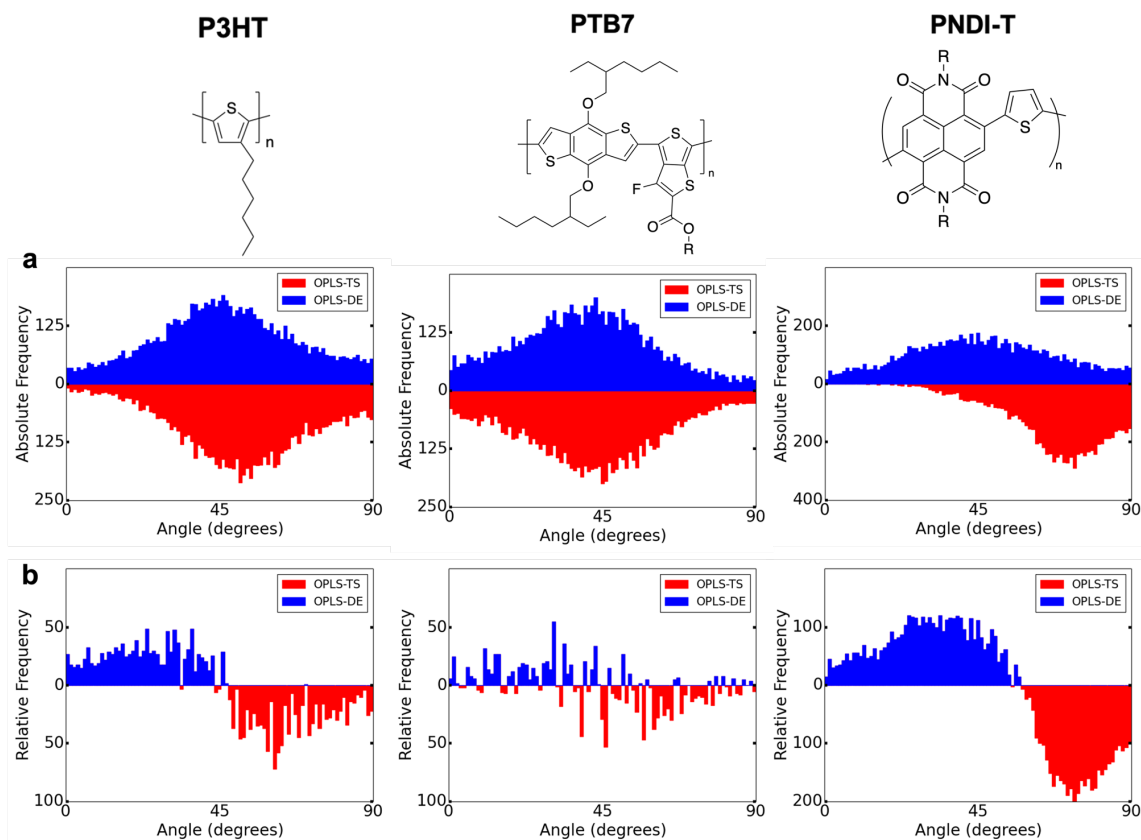
Figure 3.7: Distribution of dihedral angles in molecular dynamics (MD) runs for P3HT, PTB7, and PNDI-T. Angles are measured by deviation from planarity, such that 0° and 180° are considered identical. The total distribution of angles is shown in (a), with the upper blue bars indicating the distribution of the model using the OPLS-DE force field and bottom red bars reflecting the distribution of angles when the OPLS-TS force field is used. The net difference between the models is shown in (b), with blue bars pointed up indicting that the torsional angle is more common when the OPLS-DE model is used and red bars pointing down indicating that the torsional angle is more common when using the OPLS-TS model.
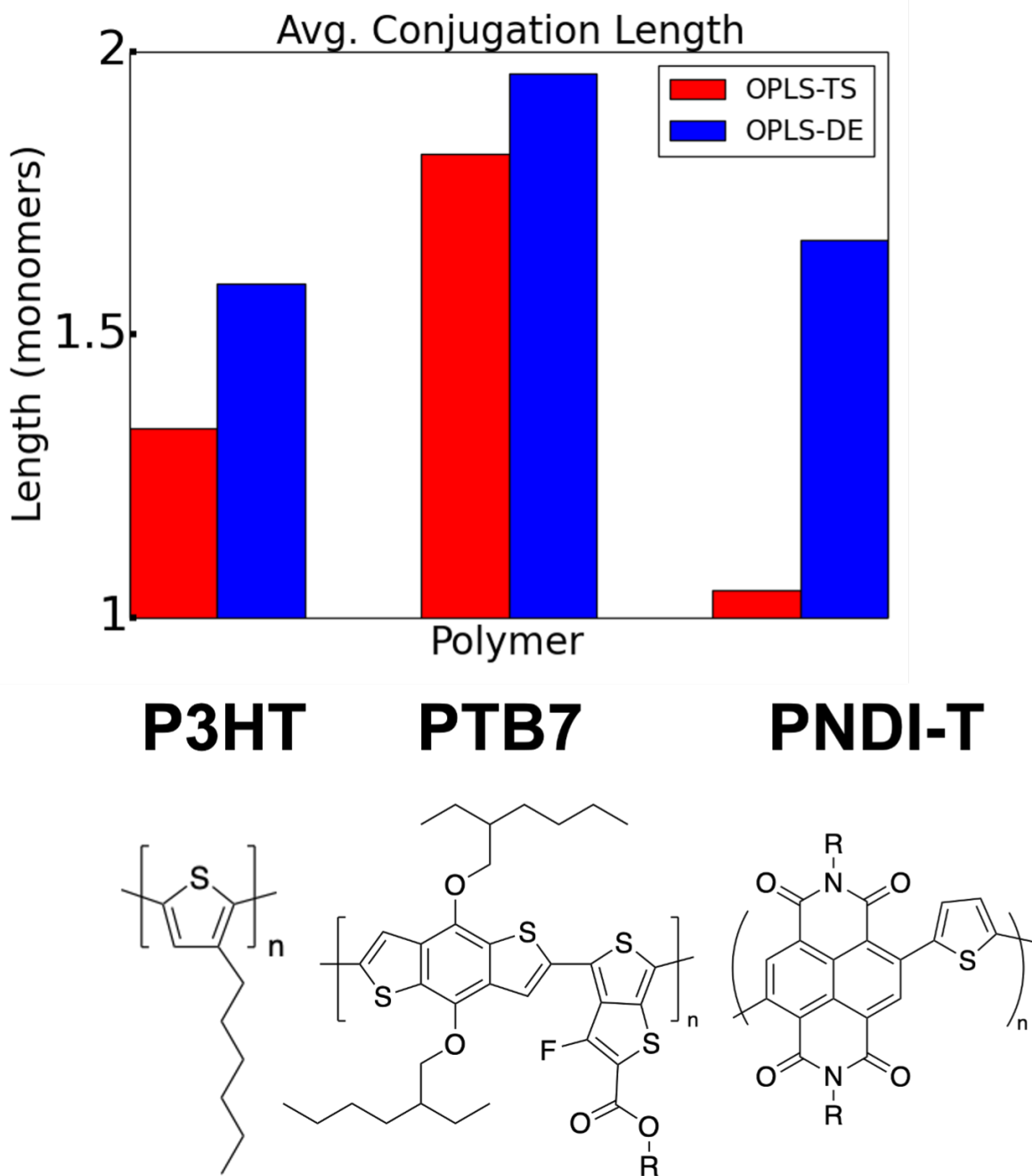
Figure 3.8: Difference in simulated conjugation length of each polymer.

Chapter 4

Modeling Energetics and Correlation between Improper and Dihedral Torsion in Conjugated Polymers

The ability of a π-conjugated (conducting or semiconducting) polymer to transport charge is critically dependent on the coplanarity—or lack thereof—between conjugated units. This coplanarity can be disrupted by dihedral twisting, which limits the delocalization of electrons along an extended π system. Thus, in order to obtain physically realistic models of the rigidity of conjugated polymers, it is critical that the energetics of dihedral twisting are treated correctly. However, conventional computational methods typically consider loss of planarity arising only from conventional dihedral torsion (i.e., relative rotation of two conjugated rings about the bond that connects them). Such methods neglect the effects of out-of-plane ("improper") torsion (i.e., two conjugated units bending toward each other like pages in a book). In this paper, we describe

a method to isolate the effects of improper torsion on the energetics of three model polymers (P3HT, PTB7, and PNDI-T). Simulations suggest that improper torsion is generally unfavorable for electronic delocalization: the breaking of planarity is increases the energy of delocalization more significantly than the additional overlap of π-orbitals lowers it. Nevertheless, we find that for PNDI-T, improper angles of up to 30° can lead to more favorable energetics than angles of 0°. This observation suggests that it is possible to maintain conjugation at high degrees of torsion. Additionally, simulations in which the dihedral and improper torsions are isolated suggest that energies of the system generally increase more quickly with improper torsion than with conventional dihedral torsion. Altogether, this work shows that judicious consideration of improper torsion (and how it affects the energies predicted by dihedral torsion) using the method described can offer an avenue for more simulating conjugated polymers with greater accuracy than is now possible.

4.1 Introduction

π-Conjugated polymers have backbones in which there is a motif of alternating double and single bonds. This arrangement enables the delocalization of electrons, which gives rise to the band structure, along with optical absorption and emission.[132,178,179] The delocalization of charge carriers between adjacent monomer residues is energetically favorable and thus provides a driving force for the coplanar configuration of monomers.[145] As a consequence of this drive toward coplanarity, conjugated polymers tend to be more rigid than saturated polymers.[180,181] The characteristic rigidity of conjugated polymers has recently begun to be investigated using computational methods.[182] A common technique for characterizing the torsion between adjacent monomers of a conjugated polymer chain is the torsional scan.[144–146] In this

method, the energy of a simple oligomer—e.g., a dimer—is calculated at planarity. Then, torsion between monomers is calculated by as a function of increasing dihedral angle. As a result, the change in energy between adjacent monomers can be calculated and used to define the energy of deplanarization. However, the torsional scan method measures the energy with respect to only one type of torsion, i.e., modulation of the conventional dihedral angle.[145,146] However, semiconducting polymers can experience another type of torsion: improper or "out-of-plane" torsion (Figure 4-1). Therefore, for most torsional scans, the energy associated with dihedral torsion cannot be decoupled from the energy associated with improper torsion. Dihedral torsion refers to the motion of two monomers in which a monomer can twist while maintaining the same center of mass, a motion often introduced in organic chemistry to refer to the gauche and trans states of a polyalkane (Figure 4-1b). Dihedral torsion can be likened to the motion of a screwdriver upon an unthreaded screw—a motion which causes torque, but no change to the center of gravity. In contrast, improper torsion occurs when the twisting of the polymer produces a movement in the center of mass of one of the monomers. The motion occurs in the direction of the normal vector relative to the orientation of the conjugated ring (Figure 4-1c). Improper torsion can be likened to the motion of a door hinge, with the center of gravity of one monomer moving as the torsional angle increases until it aligns with the center of gravity of the other monomer at $180°$. Improper torsion breaks the coplanarity of the monomers, thus (theoretically) disrupting delocalization of charge carriers between two monomers. While dihedral torsion has received nearly all attention for torsion in conjugated polymers, recent advances in organic electronics suggest that dihedral torsion may not be the exclusive form of torsional disorder that affects charge transport. Organic electronic materials with highly twisted dihedral angles have become more common in recent years.[183,184] While conventional wisdom would be that these materials

would have poor electronic properties, some of these materials are at or near best-of-their-class electronic performance.[183] It is unclear how common this additional style of improper torsion may be in these materials. It is possible that with high steric hindrance, improper torsion may be more common and even cause π-orbital overlap when improper torsion is high. However, the effects of improper torsion on the overall energy of the polymer chain—along with its effects on electronic delocalization—are not currently well understood. Improper torsion is difficult to treat in a simulation due to the increased proximity of the two monomers resulting in potentially large increases in steric energies. This difficulty arises when the energies that result from the improper torsion become convoluted with the energies arising from steric effects (e.g., as a result of increasing torsional angle). To model improper torsion, energy related to improper torsion has primarily been dealt with through simple 3-body angles, as included in conventional force fields (e.g., OPLS, AMBER).[69,185] As improper angles approach $90°$, these simple three-body angles will also approach $90°$, causing energy to spike sharply. Two methods are commonly used to define the 3-body angles and, thus, control the improper torsion. In the first method, a minimum energy is defined at the equilibrium angle for all angles spanning the monomer. The equilibrium angle is defined as the angle calculated from a quantum mechanical geometry optimization. As the improper angle deviates from planarity, the energy associated with changing harmonic angles quickly spikes. In the second method, simple angular characterizations are taken from a general force field (i.e., OPLS, CHARMM) and used to enforce improper angles. As the 3-body angles generated from a force field do not strictly enforce a single angular conformation (e.g. three angle equilibria defining a full circle do not add to $360°$), it improper torsion faces a less sharp energetic penalty. However, due to a lack of study it is currently unclear how well either of these methods constrains improper torsions between adjacent monomers. An additional diffi-

culty arises from the likely correlation between the energetics of improper torsion and the energetics of dihedral torsion. For example, if electron delocalization is being partially blocked by an improper torsion, additional dihedral torsion may result in a lower energetic penalty for blocking further delocalization. Due to this coupled relationship, it is not possible to fully characterize the energetics stemming from improper torsion using a simple modification of angular or improper potentials. We thus introduce a method of characterizing the effects of improper torsion on electronic delocalization similar to that of the torsional scan, which is used to elucidate the energetic effects of dihedral torsion. First, we characterize the energetics of improper torsion—combined with dihedral torsion—by using a method developed to isolate the nonbonded and delocalization energetics of torsion ("OPLS-CP"). Next, we implement a method to characterize the correlated energetics of dihedral and improper torsions through a collective variable module, PLUMED.[186] We test our energetic characterizations on a set of randomized dimer configurations to determine the applicability and necessity of correlated energies. Finally, we compare both existing methods of controlling improper torsion using different angular parameterization schemes in order to control improper torsion.

4.2   Results and discussion

Using the computational method described in the Improper Angles of Films section, we determined the frequency of each improper angle for P3HT, PTB7, and PNDI-T with different angular parameterizations (Figure 4-3). Surprisingly, for all three polymers the distributions of improper angles that occur were fairly similar. However, there are several notable observations consistent for all three polymers. First, the most frequent angle defining the improper angle between monomers was relatively small, around $5°$. However, monomers with no improper torsion

at all (i.e., a torsional angle of $0°$ or $1°$) occurred infrequently. Therefore, our simulations suggest that most conjugated polymer chains will have some amount of improper torsion, regardless of how the inter-ring angles are parameterized. Our simulations suggest that the ubiquitous occurrence of improper torsion will lead to an incorrect calculation of the dihedral angle, even at small improper angles (Figure 4-4). Second, large improper angles between monomers occurred relatively frequently. That is, the frequency of monomers with an improper angle ¿$10°$ is approximately equal to the frequency of monomers with improper angles ¡$1°$. Thus, our simulations suggest that significant improper angles are common in all conjugated polymers. Therefore, the presence of improper torsion within a conjugated polymer is a necessary consideration for the overall energetics of the polymer chain (e.g., electronic delocalization). Moreover, this consideration must also take into account how improper torsion and dihedral torsion affect one another as well. We additionally note that these simulations are performed at normal equilibrium conditions (i.e., at room temperature). Elevated temperatures or non-equilibrium conditions could result in a high degree of polymer torsion, thus resulting in more frequent and larger improper torsion between monomers. In such conditions, the effects of improper torsion on the energetics (and thus physical properties) of the polymer chain are likely to be even more impactful. A critical component of the energy associated with both dihedral and improper torsion is the non-bonded interaction. Nonbonded forces usually manifest as steric repulsion at the internuclear distances considered here. In order to separate the effects of nonbonded forces from those of electronic delocalization on the overall energy, we first investigated the energetics related to dihedral and improper torsion without accounting for nonbonded energy (Figure 4-5). We have previously found that the torsional scan method quickly run into difficulties when steric hindrance results in a domination of the nonbonded energy over the delocalization energy. A

similar case holds true for improper torsion as well. For all degrees of improper torsion (e.g., all considered improper angles), the overall energetic differences are dominated by a dramatic increase in energy (Figure 4-5). Given an increase in steric hindrance, it seems likely that these interactions are unrelated to electronic delocalization. Given that combinations of dihedral and improper torsion can avoid steric hindrance (i.e. a slight combination of both would prevent nucleic collisions) and nonbonded interactions are already dealt with in simulations through e.g. Lennard-Jones interactions, including the nonbonded energy for improper torsion could result in greater inaccuracy. In addition, the energetics of dihedral torsion when improper torsion is included are additionally skewed by nonbonded interactions. In P3HT, the energy of adjacent monomers sharply rises and falls near $0°$ of torsion as the large sulfur atom becomes close to the hydrogen atoms in the adjacent ring. The F-in variation of PTB7 sees large variations in energy (both upwards and downwards) as the fluorine atoms approach the benzodithiophene monomer. Notably, these same energetic variations are not present in simulations of the F-out variation of PTB7. For PNDI-T, there is a clear energetic maximum at around $180°$ with a value that is approximately 3 times greater than the next greatest local maximum. However, there is no clear energetic minima because nearly all conformations are dominated by steric hindrance. Likewise, these energetic distributions do not offer any facile interpretation in terms of effects specific to conjugated materials (e.g., electronic delocalization). Finally, energetic calculations near $0°$ and $180°$ can also differ greatly (e.g., for F-in PTB7, PNDI-T). Therefore, we find that the dominance of steric hindrance in individual torsional scans (and between torsional scans) both (1) affects the energetics associated with improper and dihedral torsion and (2) obscures information about the energetics that are fundamentally important to the material system (e.g., energy related to electronic delocalization).

To decouple the steric effects in our simulations, we use a method described in Improper Angle Characterization to approximate the nonbonded energy of the system. We recalculate the energy of each polymer system using this method in order to decouple the delocalization energy and nonbonded energy. In doing so, we elucidate the effect of both dihedral torsion and improper torsion on the energetics solely associated with delocalization of charge (Figure 4-6). Once the nonbonded energies are removed, a clear pattern emerges: the potential barrier associated with dihedral torsion tends to decrease as improper torsion increases. That is, the total energy that can be lost or gained due to dihedral torsion is reduced as improper energy increases, likely to a reduction in overall delocalization energy available to be gained or lost. For all three polymers, there are energetic minima around dihedral angles of $0°$ and $180°$ and maxima around $90°$ and $270°$. Likewise, for polymers at the same dihedral angle, an increase in improper torsion results in a lower amount of delocalization energy available to be lost or gained for P3HT and PTB7. Interestingly, this trend holds true for PNDI-T until the high improper angles, at which point an increase in improper torsion resulted in the most favorable energetics, even when compared to PNDI-T with no improper torsion ($0°$). For this polymer with a strong push-pull effect and a highly twisted native state, a high improper angle is most energetically favorable than no dihedral angle. This finding suggests that improper torsion may play a role in PNDI-T electronic delocalization in this highly twisted polymer. While in Figure 4-5 the energy overall increases with increasing improper torsion, the increase is smaller than in PTB7 and P3HT. The fact that the energy decreases more slowly despite high steric hindrance in PNDI-T suggests this polymer may be more amenable to improper torsion. Notably, the total energy for approximately a $20°$ improper torsion—the amount of improper torsion at which electron delocalization begins to become more favorable with greater torsion, suggesting π-orbital overlap—is

lower than the energy required to transition between $0°$ and $180°$ in all polymers, suggesting this dihedral torsion is not infrequent. Finally, we see that the PTB7 F-in and F-out have similar energetic distributions when nonbonded forces are removed. This comparison of the two monomer variations suggests that the change in fluorine position primarily affects the nonbonded energetics, while the delocalization energy across all dihedral angles remains approximately the same. The exact reduction of dihedral barriers is calculated from the difference in energies between the $0°$ and $90°$ dihedral angles for each polymer (Figure 4-7). We find that the torsional barrier decreases as the improper angle increases. In general, it appears that energetic loss due to increased torsion is more significant than any additional overlap of π-systems that is induced by the introduction of improper torsion. The exception to this is PNDI-T, for which a high improper angle results in the most favorable energetics (Figure 4-6). However, the torsional barrier due to dihedral torsion is still lowered, suggesting that this electronic favorability is relatively impervious to dihedral torsion. This observation is interesting because we previously show that all polymer systems are predicted to have a non-negligible amount of improper torsion (Figure 4-3). Our simulations of PNDI-T suggest that favorable delocalization energetics can be maintained despite a highly twisted backbone. Future study is needed to determine whether this is related to the high degree of push-pull effect in this poly(naphthalene diimide)-based polymers (e.g., from the greater differences in electronegativity between the donor and acceptor moieties). Likewise, future work is needed to determine if the relatively high frequency of large amounts of improper torsion allow for large amounts of overlap within the π-system, thus allowing conjugation to be maintained over larger length scales (e.g., more pathways for charge carriers to move). That is to say, because the polymer chains that compose a polymeric solid (e.g., a thin film) will have some frequency and degree of improper torsion (and dihedral torsion), whether more favorable

electronic properties can be maintained if conjugation can persist despite torsion of the backbone. We observe that the primary cause of the change in the dihedral barrier appears to be the energy associated with the planar dimer ($0°$ or $180°$), which rises much more quickly than the energy of the dimer in the antiplanar state ($90°$ or $270°$). Because the energetic difference (between the $0°$ and $90°$ orientations) is reduced, this finding suggests that improper torsions are inherently energetically unfavorable for electronic delocalization. We expand our comparison of dihedral and improper torsions by investigating the effect of each torsion in the absence of the other on each polymer. That is to say, we investigate the effect of dihedral torsions (with $0°$ of improper torsion) and improper torsions (with $0°$ of dihedral torsion) on P3HT, PTB7, and PNDI-T when isolating the delocalization energy (Figure 4-8). For P3HT, PTB7 (F-in), and PNDI-T, improper torsion generally has a greater effect on the energetics in comparison to dihedral torsion (for equivalent torsional angles and the absence of the other type of torsion). In PTB7 (F-out), the effect of both styles of torsion are similar. The fact that the effect of improper torsion on the two monomer variations of PTB7 differs so significantly indicates that there is a twofold effect on the energetics, as previously discussed. That is to say, there is both disruption of the internal monomeric conjugation, as well as increased overlap of π-conjugation. The similarity between the torsional scans of the F-out variation of PTB7 in Figures 5 and 6, suggest that the F-out conformation is the least sterically hindered of all four polymer conformations simulated. In comparison, the same amount of improper torsion on the F-in variation results in changes to the energetics that are 2-3 times greater. This finding suggests that improper torsion is significantly more energetically harmful than dihedral torsion, likely due to further disruption due to steric effects. The sole difference between the F-out and F-in conformations of PTB7 is steric hindrance. When the energy of delocalization is isolated (i.e., when the nonbonded forces are removed) and

no improper torsion is imposed, both conformations have similar energetic distributions across all dihedral angles (Figures 5 and 6). The two dimer conformations are chemically equivalent. However, in the F-out conformation, the fluorine atom points toward the outside of the dimer, such that the unsubstituted sulfur atom is the closest atom to the benzodithiophene backbone. This orientation minimizes steric clashes between the atoms involved, likely reducing the effects of steric clashes on lowering the internal conjugation of each monomer. The result is that the dihedral torsion and improper torsion yield similar energetic barriers. In contrast, in the F-in conformation of PTB7, the fluorine atom is significantly closer to the benzodithiophene backbone, which increases the likelihood of steric clashes. As a result, the F-in conformation has a substantially stronger energetic penalty for improper torsion in comparison to dihedral torsion at all torsional angles. Altogether, this difference suggests that steric hindrance has a significant effect on the fundamental electronic delocalization of monomers when improper torsion is considered. In a real system (e.g., in a polymeric thin film), polymer chains will be subject to both improper and dihedral torsion simultaneously. Therefore, we elucidate how our computational method compares to conventional torsional scans for determining the energetics of polymer systems in which there is both improper and dihedral torsion (Figure 4-9). We compare the accuracy of a conventional torsional scan model to that of our computational model as described above. For all three polymers, our model improved upon the accuracy of a conventional torsional scan, with PNDI-T showing the largest improvement. Specifically, our model seemed to improve in accuracy relative to increase in steric hindrance within the polymer system. The F-out variation of PTB7, the dimer with the lowest steric hindrance, sees the least improvement in accuracy when dihedral and improper forces are both included (0.47 kJ/mol). P3HT and the F-in conformation of PTB7 (two dimers experiencing moderate degrees of steric hindrance) see

larger improvements in accuracy, at 2.27 kJ/mol and 2.61 kJ/mol, respectively. PDNI-T, a polymer with high degrees of steric hindrance, sees the largest improvement in accuracy at 4.69 kJ/mol. These results demonstrate that (1) correct calculation of the energy related to improper torsion and (2) consideration of the relationship between improper torsion and dihedral torsion substantially helps improve the accuracy of a model for conjugated polymers. This improvement in accuracy generally correlated with the steric hindrance present in each polymer system. Consequentially, it is possible that the increase in accuracy was due to the correlation of nonbonded energies rather than accounting for the energy related to improper torsion. Therefore, we compare our model using coupled improper and dihedral torsion to a modified torsional scan model, in which nonbonded energies are isolated and removed as well. That is, an OPLS-style dihedral angle with no coupling to an improper angle is compared to the coupled improper and dihedral energies. The results are shown in Figure 4-10. For all polymers, when only the energy of delocalization is considered, there remains an improvement in accuracy for the model in which improper torsion is considered. This improvement in relative accuracy was approximately 33% to 50% that of the models for which delocalization and nonbonded energetics were not decoupled. This decrease suggests that a fraction of the improvement in accuracy was due to the correlation to steric interactions. However, a substantial improvement in accuracy was shown for all polymers when energy is related to coupled improper and dihedral angles. The exception was once again PNDI-T, in which the improvement in accuracy was significantly decreased in comparison to the model in which steric interactions were considered. That is to say, the increase in accuracy was largely in part due to the correction of nonbonded effects. The primary reason for this discrepancy between the two determinations of relative accuracy seems to be due to a poor representation of PNDI-T at small degrees of improper torsion (¡5°). Although this

79

finding shows that consideration of improper torsion improves the accuracy of PNDI-T simulations, a comparison between models that do and do not account for nonbonded effects suggest that sterically hindered polymers like PNDI-T largely benefit from removal of the nonbonded energy from torsional characterizations.

4.3 Concluding Remarks

This work sought to understand the effect of improper torsion on the energetics of three model polymers: P3HT, PTB7, and PNDI-T. Our simulations suggest that varying degrees of improper torsion would be common in the polymer chains that compose a solid sample. This finding is significant because of how improper torsion affects conjugation along a polymer chain. First, improper torsion decreases conjugation when planarity is broken. Second, improper torsion increases electronic delocalization if additional overlapping of the π-orbitals is induced. In general, we find that the first effect is stronger than the second, and thus an increase in improper torsion generally results in a greater energetic barrier to torsion for all polymers except PNDI-T (when large improper angles are induced). As a result, improper torsion is generally an obstacle for electronic delocalization. Additionally, we find that energetic penalties from steric interactions can significantly obscure the energetic penalties associated with electronic conjugation relative to increasing improper torsion. Therefore, by modifying our computational method to isolate the energy related to electronic delocalization, we show that the barrier to torsion decreases as improper angle increases. Similarly, by isolating the effects of both styles of torsion, we determine that improper torsion generally imposes a stronger energetic penalty compared to dihedral torsion. However, the complex interplay between steric interactions, dihedral torsion, and improper torsion results in some exceptions. In particular, simulations of PNDI-T suggest

that it is possible for adjacent monomers in a conjugated backbone to be highly twisted and still maintain conjugation. Finally, we show that a computational method that considers both improper and dihedral torsion can be used to more accurately simulate all three model polymers, although the increase in accuracy for some polymers (e.g., the F-out variation of PTB7, PNDI-T) mainly stem from the correlation to steric effects. Our findings indicate that the inclusion of a modified characterization of improper torsion helps better describe the energetics of conjugated polymers. Thus, consideration of the improper torsion within a conjugated system is required for highly accurate models of semiconducting polymers. This importance stems from the effect of improper torsion on both the overlap of π-orbitals as well as internal disruption of π-systems. In addition, improper torsion can directly affect dihedral torsion. Therefore, improper torsion appears to be of particular importance in polymer structures with large amounts of steric hindrance. Improper torsion is even more so likely to be important when high degrees of torsion are present in general (e.g., films under strain, polymers deposited from melt, films annealed at high temperatures). While description of improper torsion improves the accuracy of modeling conjugated polymers, further steps should be taken to quantify the effects of improper torsion. Judicious exploration of the placement of additional hydrogen atoms to optimally block steric hindrance would be preferred, as high steric hindrance can still cause difficulties in modeling. For example, we show that the behavior of PNDI-T differs greatly from both P3HT and PTB7 when improper torsion is introduced between two monomers. Further exploration of highly sterically hindered polymers (particularly D–A polymers with asymmetric monomers) can provide information about the disruption of electronic delocalization in conjugated polymers. For example, our findings suggest that PNDI-T can maintain favorable electronic delocalization at high degrees of improper torsion. Therefore, further investigation of improper torsion in D–A polymers

elucidate the energetic effects of π-orbital overlap. Additional work in this area could offer significant insights into the high mobilities of modern D–A polymers, many of which are amorphous or take advantage of short-range aggregation. Thus, accurate understanding of how chemical structure affects the morphology (as mediated by chain conformation and packing structure) of a polymer solid offers an avenue for improving predictions of its physical (e.g., electronic and mechanical) properties. In doing so, computational simulations of conjugated polymers can be used to facilitate the rational design of new polymeric materials.

4.4   Materials and Methods

Improper Angle Characterization

Improper Angle Characterization. To extract the energies arising from improper torsion between two aromatic monomer residues, we first isolated the nonbonded (steric) forces. Without isolating these forces, it is likely that they would otherwise dominate the output of a torsional scan equivalent (e.g., placing an improper dimer under an increasing degree of improper torsion). To extract the energy related to nonbonded interactions, we underwent a three-step process (Figure 4-2). We first conducted a torsional scan on a simple dimer with a perfectly coplanar structure. The energetics of the dimer system were calculated at the RI-MP2 level with a cc-PVTZ basis set. The improper angle of the dimer was slowly increased in 5° intervals up to 30°. After 30°, the improper angle was modified by 10° at a time to account for the low likelihood of improper angles occurring beyond 30°. At each improper angle, we performed a torsional scan, allowing the monomer to undergo a dihedral rotation in increments of 10° up to 360°. Each individual dihedral scan was fit to an OPLS function, and the OPLS parameters

82

between improper angles were fit to a 6th order Fourier series in order to handle any arbitrary functional form. For the second step, this process was repeated, except this time two hydrogen atoms were added to one of the monomers at the (2,5) positions. One hydrogen atom was placed in a physical position, on the carbon that is not part of the inter-ring bond. The other hydrogen was placed perpendicular to the aromatic ring in the direction of the normal vector (1.08Å away). This unphysical hydrogen blocks electron delocalization, as well as any forces related to the energy of delocalization. For the third step, this process was again repeated with another structural variant. In this final step, one of the rings was replaced entirely with a methyl group. The hydrogen atoms in the methyl group were oriented in such a manner as to replace the carbon atoms that would be bonded to the 2-carbon if a full ring was used. Likewise, the unphysical hydrogen atom was again placed in the same position as in the hydrogenated dimer (i.e., in an orientation that minimizes the energy) to minimize steric effects. After repeating torsional scans for this chemical structure, the energy associated with each improper angle was fit to an OPLS-style dihedral form. The parameters for each OPLS-style dihedral were then fit to an arbitrary 6th order Fourier function.[185] By subtracting the calculated energy associated with conjugation, as determined using the methylated monomer, from the calculated energy of the hydrogenated dimer, one can isolate the nonbonded energy (i.e., steric forces). Likewise, by subtracting the calculated energy of the hydrogenated dimer from the simple dimer, one can isolate the energy of electronic delocalization.

Selection of Materials

To determine the effectiveness of our method across a diverse array of π-conjugated polymers, three different polymers were tested: poly(3-alkylthiophene) (P3HT), polythieno[3,4-

b]-thiophene-co-benzodithiophene (PTB7), and poly(naphthalene diimide) with a single bridging thiophene (PNDI-T). P3HT is a well-studied homopolymer that is often used as a model semi-conducting polymer.[187] We chose PTB7 as a representative polymer because the benzodithiophene backbone motif is common for modern p-type polymers.[188] Additionally, PTB7 has two distinct monomer types (and thus two distinct monomer configurations). In one, the fluorine is pointed to the outside of the dimer, a conformation we refer to here as "F-out". Alternatively, the fluorine can also be oriented inward, and this configuration is referred to as the "F-in" conformation. These two conformations are typically dealt with distinctly when using a dihedral torsional scan and thus are also treated separately here. Finally, we chose PNDI-T because the naphthalene diimide backbone motif is common for n-type donor-acceptor (D–A) polymers.172 PNDI-T has several characteristics that distinguish it from P3HT and PTB7. PNDI-T is highly sterically hindered in the planar state, causing it to adopt a highly twisted conformation.159 Additionally, the monomers that compose PNDI-T have much greater differences in electron affinity relative to PTB7. One strategy for improving the charge transport capabilities of D–A polymers is tuning the electronegativity between the donor and acceptor moieties. Therefore, we also use PNDI-T as a model to elucidate the applicability of our computational method for current state-of-the-art D–A style polymers.

Calculation of Accuracy

To determine the relative accuracy of the new torsional style, both monomers of a dimer for all three polymers were frozen in place using the RIGID package.[189] Any existing restrictive energetics associated with dihedral torsion were removed, and thus the dimer was allowed to freely rotate at 800 K to sample conformational space. Snapshots of random conformations

were taken every 100 ps and quantum calculations were conducted at the RI-MP2 level for each conformation, for a total of 100 conformations. The difference in energy between all dimers (as calculated by RI-MP2) was then compared to the difference in energy as calculated by a conventional dihedral parameterization and a specialized force field coupling dihedral and improper torsion. PLUMED (a software package conventionally used for methods requiring definition of an arbitrary variable, e.g., metadynamics) was used to provide external bias on two coupled collective variables: (1) the conventional dihedral angle and (2) the absolute value of both improper angles summed together (to identify how improper torsion affects electronic delocalization).[186] These collective variables could be jointly used to calculate the overall energetic change due to torsion.

Improper Angles of Films

Initial conformations of the polymer film were set using Packmol at a density of approximately 0.2 g/cm3.[190] These polymer films were allowed to equilibrate in the NPT ensemble for 5 ns at 400 K before being cooled to 300 K over 0.5 ns. Two different styles of angular parameterization were then given to each inter-ring interaction. In one style, the angles bridging adjacent monomers were set to all be at the equilibrium angle determined by a geometry optimization performed at the BP86 level with a def2-SVP basis set. For the second style, angles were directly taken from a force field parameterization scheme for OPLS-style force fields, LigParGen.[191–193] The films were then placed in the NVT ensemble and heated to 800 K over 2 ns, kept at 800 K for 5 ns, and cooled to 300 K over 2 ns to induce randomization. After allowing each film to equilibrate at 300 K over 1 ns, the improper angles were measured.

4.5 Acknowledgements

Chapter 4, in full, is a reprint of material in preparation to be published in: **Kleinschmidt AT**, Chen AX, Pascal TA, Lipomi DJ. Modeling Energetics and Correlation between Improper and Dihedral Torsion in Conjugated Polymers. *In Review*. The dissertation author was first author of this paper.
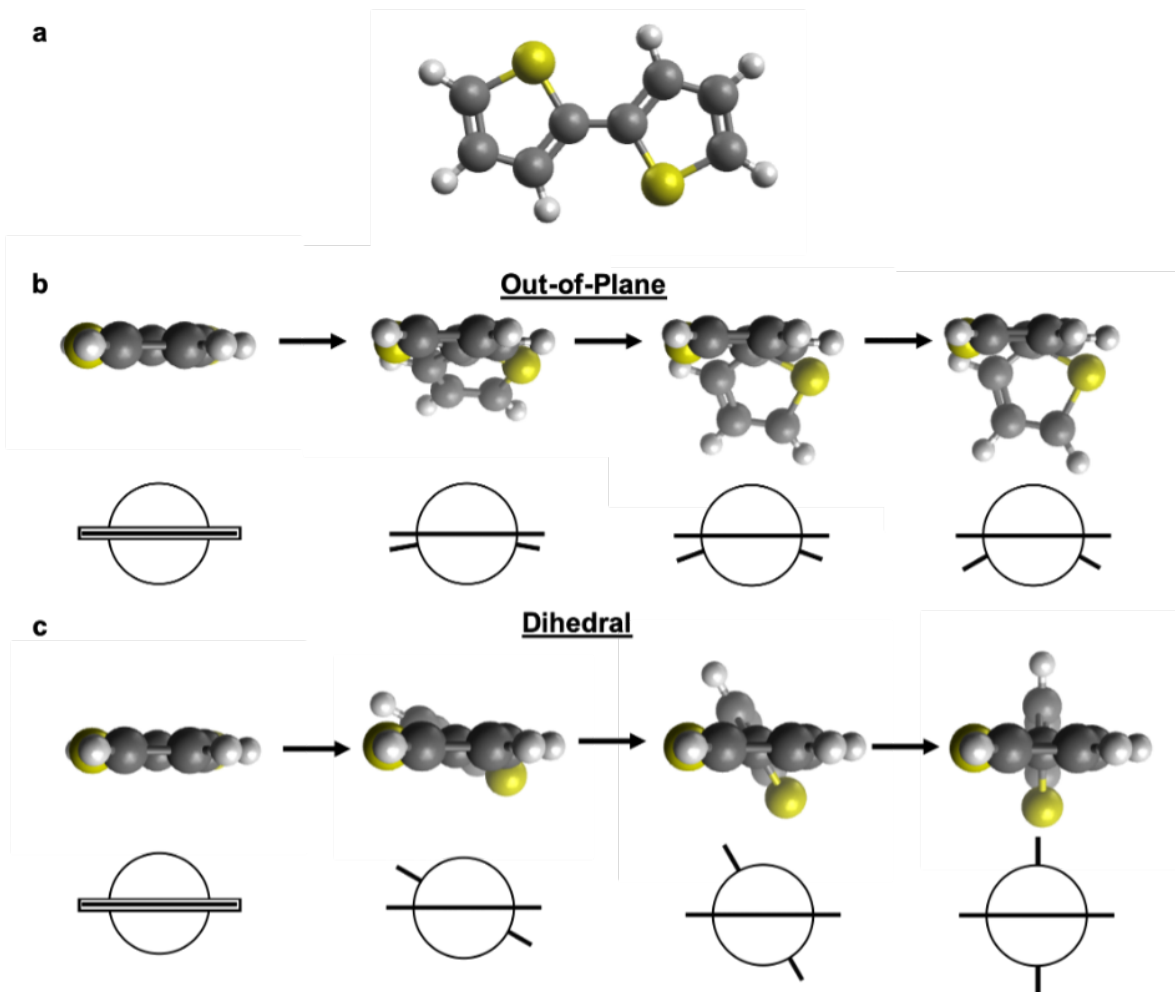
Figure 4.1: Conjugated polymers can experience two types of torsion: dihedral torsion and improper torsion. In (a) dihedral torsion, the twisting of monomers does not result in a change in the center of gravity. This is in contract to (b) improper torsion, in which an increase in torsional angle accordingly shifts the center of gravity of one monomer.

$E_{delocalization} + E_{conjugation} + E_{nonbonded}$ $E_{conjugation} + E_{nonbonded}$ $E_{conjugation}$
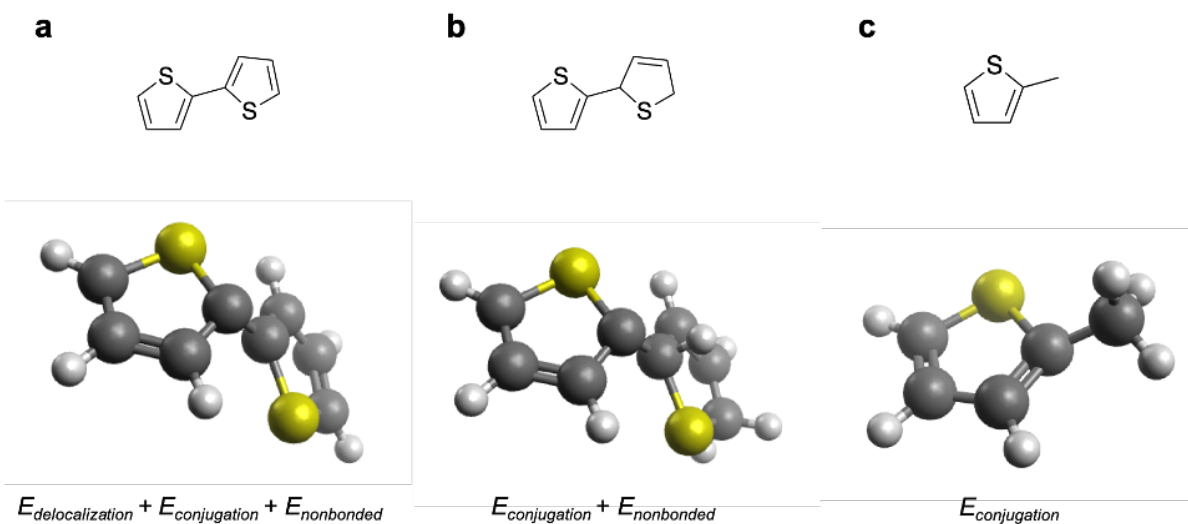
Figure 4.2: Method of isolating the energy associated with electronic delocalization. Torsional scans are conducted on (a) a coplanar dimer, (b) a hydrogenated dimer, and (c) a methylated monomer (i.e., where a monomer is replaced by a methyl group). By subtracting the calculated energy (relative to improper angle) of the hydrogenated dimer from the simple dimer, the delocalization energy can be isolated. Similarly, by subtracting the calculated energy of the methylated monomer from the hydrogenated dimer, the nonbonded energy can be isolated. Thus, this method allows one to decouple the energetics related to electronic delocalization and energetics from steric forces.
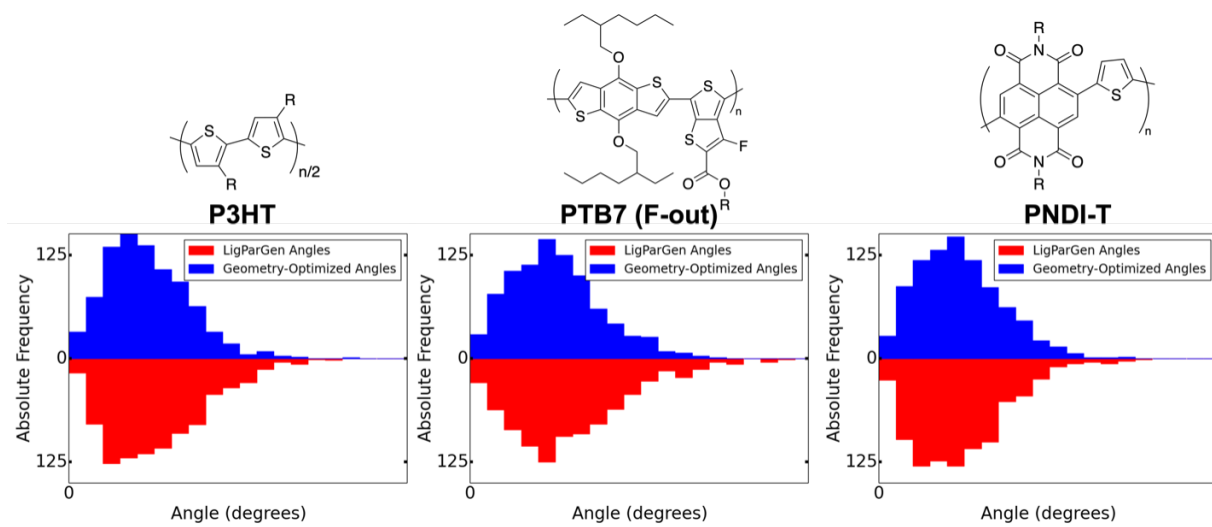
Figure 4.3: Improper angles of randomized films.
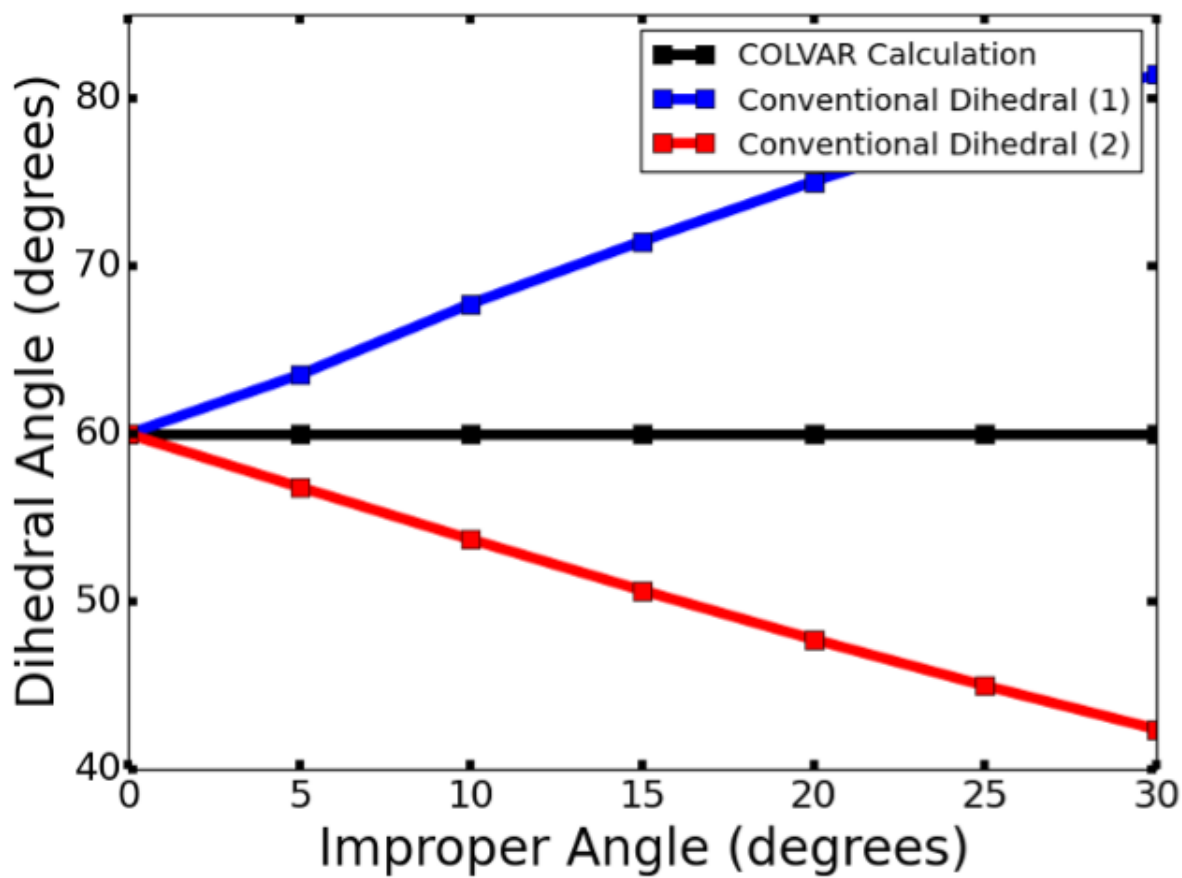
Figure 4.4: Calculation of dihedrals with increasing improper angle.
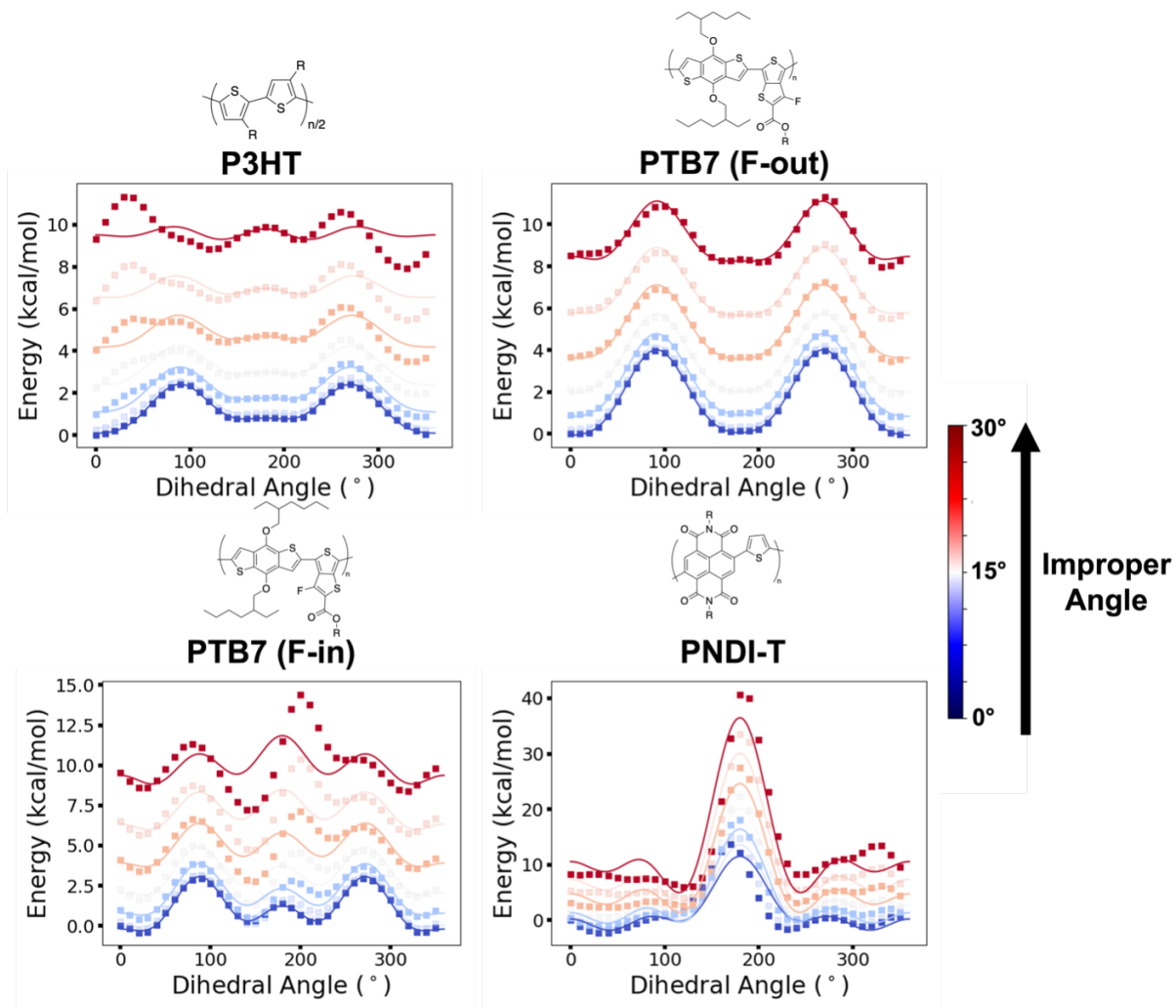
Figure 4.5: Energy calculated directly from torsional scans of adjacent monomers for (a) P3HT, (b) PTB7 F-out, (c) PTB7 F-out, and (d) PNDI-T relative to dihedral angle (from 0° to 360°) and improper angle (from 0° in blue to 30° in red).
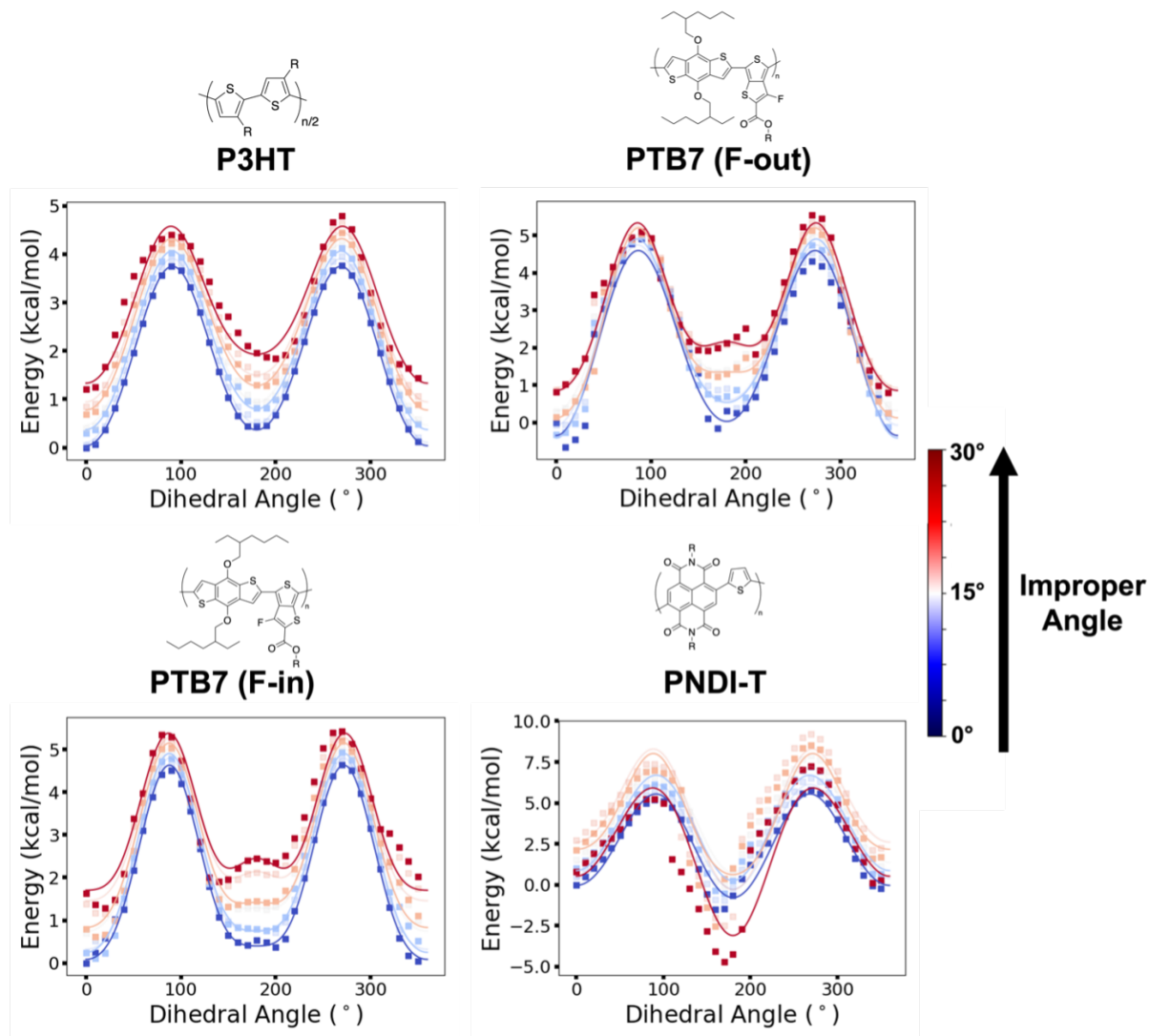
Figure 4.6: Energy associated with delocalization isolated from torsional scans of adjacent monomers for (a) P3HT, (b) PTB7 F-out, (c) PTB7 F-out, and (d) PNDI-T relative to dihedral angle (from 0° to 360°) and improper angle (from 0° in blue to 30° in red). By removing the nonbonded energy associated with steric interactions from each simulation, the effect of both dihedral torsion and improper torsion on the delocalization energetics can be elucidated.
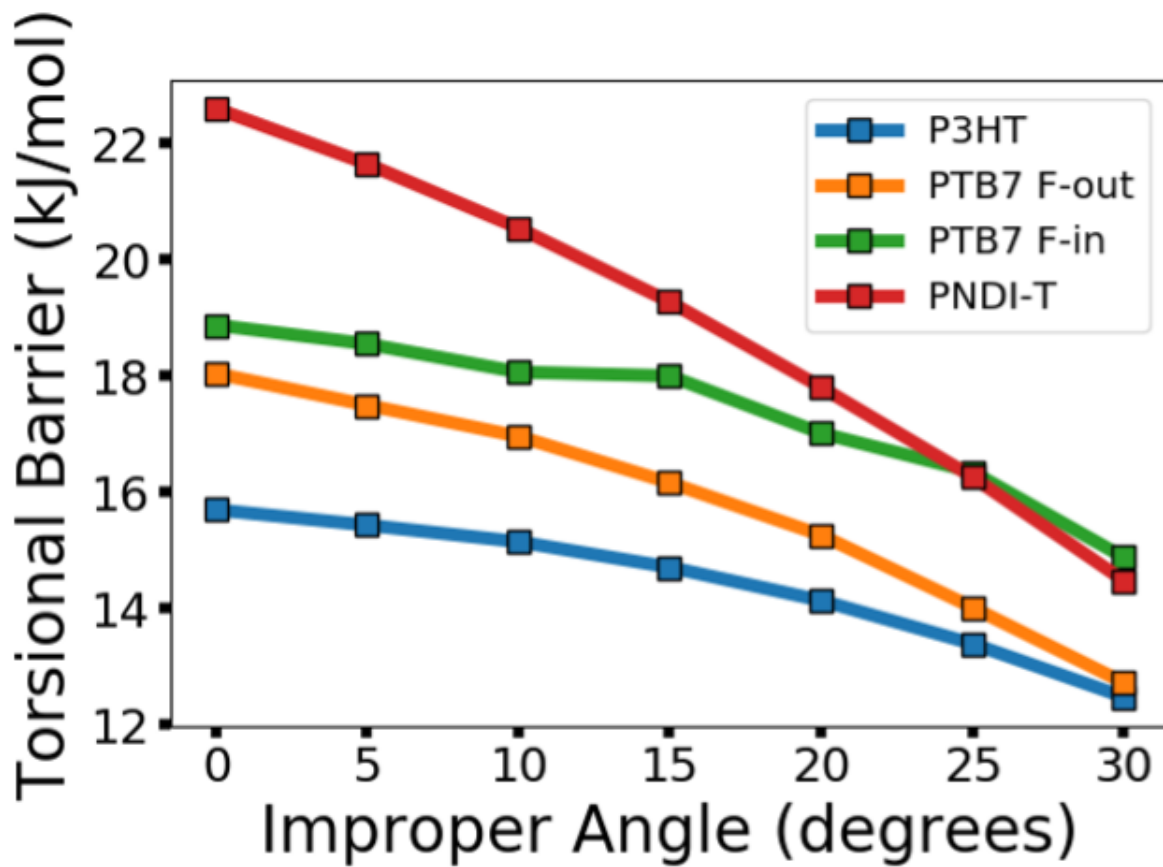
Figure 4.7: The torsional barrier, generally, decreases relative to increasing improper torsion for P3HT, PTB7 (F-in and F-out), and PNDI-T.
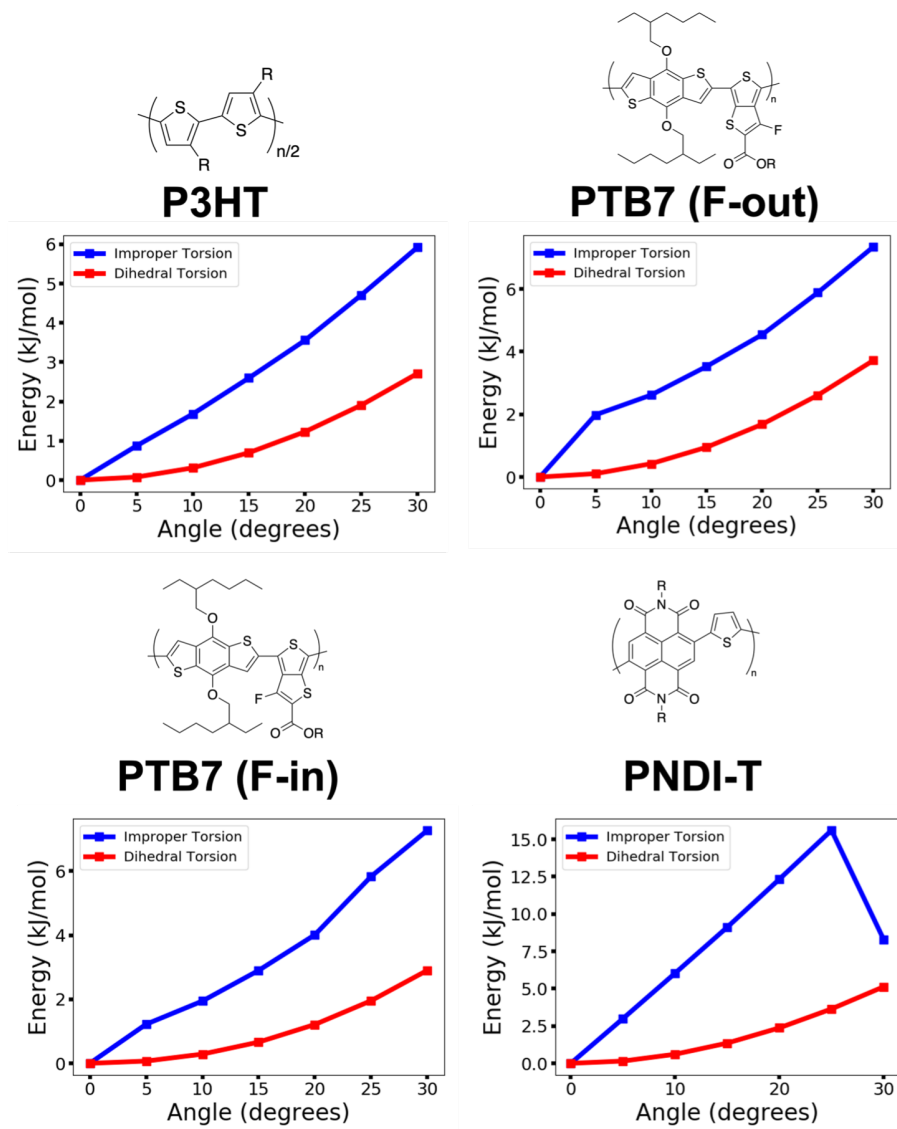
Figure 4.8: Increase in energetic barrier relative to increasing dihedral torsion (without improper torsion) and increasing improper torsion (without dihedral torsion) for P3HT, PTB7, and PNDI-T.
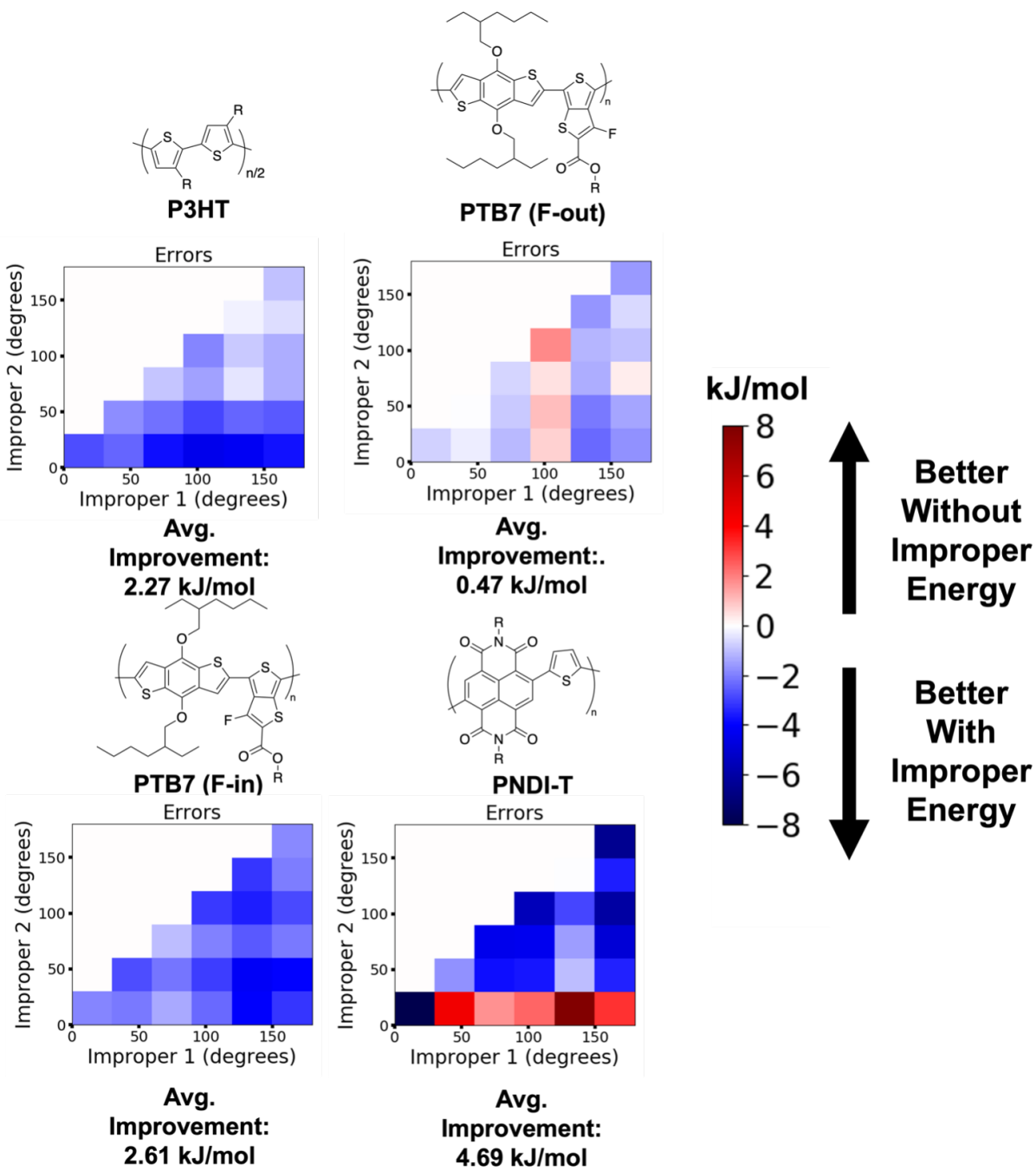
Figure 4.9: Comparison of accuracy for the energetics of P3HT, PTB7, and PNDI-T when both dihedral torsion and improper torsion are considered using a conventional torsional scan.
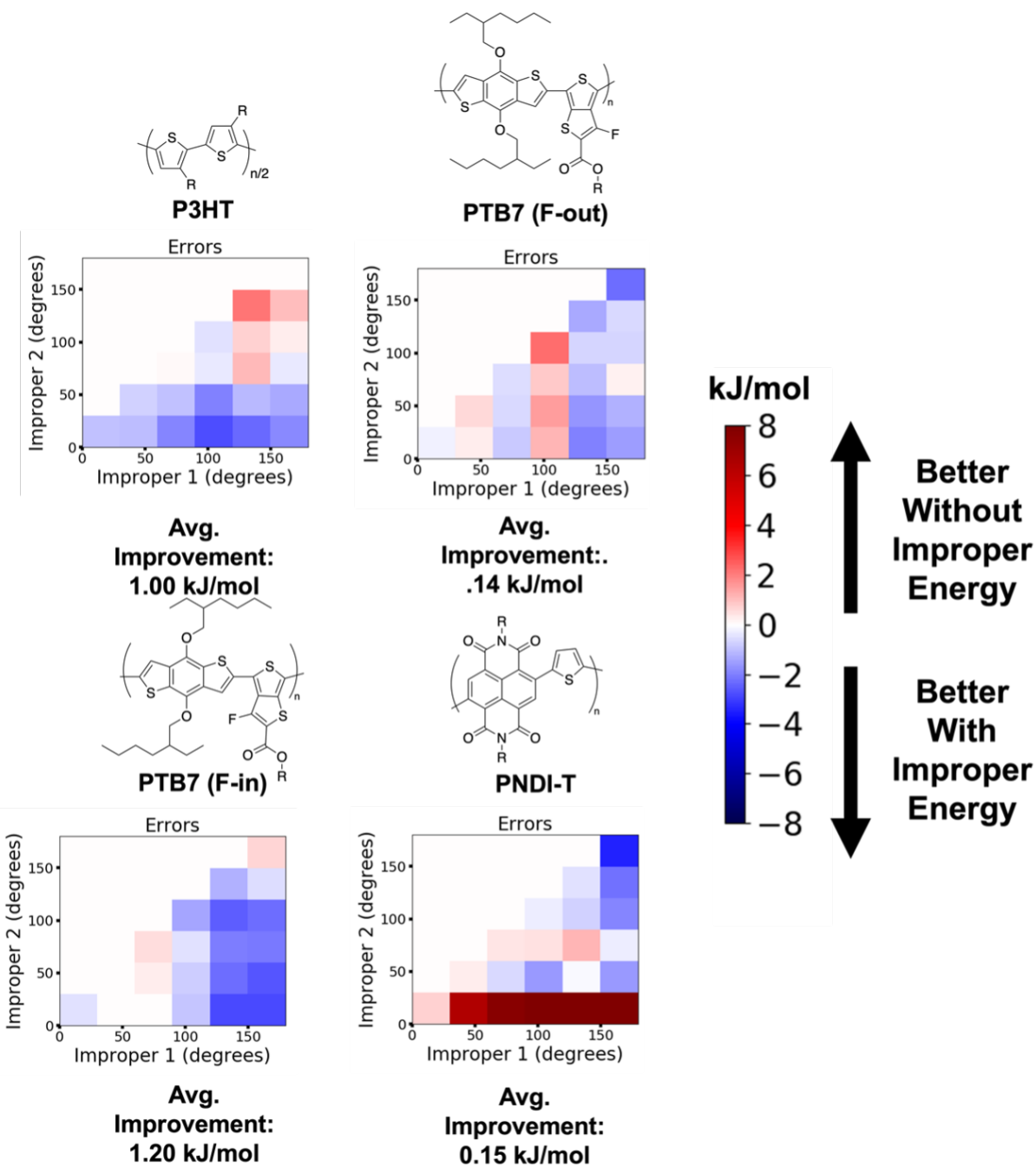
Figure 4.10: Comparison of accuracy for the energetics of P3HT, PTB7, and PNDI-T when both dihedral torsion and improper torsion are considered using a modified torsional scan model. In this modified method, the delocalization energy is decoupled from the nonbonded energy in order to isolate the effects of improper torsion solely on the energetics associated with electronic delocalization.

Chapter 5

Interactions Across Many Monomers Significantly Affect π-Conjugated Polymer Morphology

The ability of a π-conjugated (conducting or semiconducting) polymer to transport charge is critically dependent on the coplanarity—or lack thereof—between conjugated units. This coplanarity can be disrupted by dihedral twisting, which limits the delocalization of electrons along an extended π system. Thus, in order to obtain physically realistic models of the rigidity of conjugated polymers, it is critical that the energetics of dihedral twisting are treated correctly. However, conventional computational methods typically consider loss of planarity arising only from conventional dihedral torsion (i.e., relative rotation of two conjugated rings about the bond that connects them). Such methods neglect the effects of out-of-plane ("improper") torsion (i.e., two conjugated units bending toward each other like pages in a book). In this paper, we describe

a method to isolate the effects of improper torsion on the energetics of three model polymers (P3HT, PTB7, and PNDI-T). Simulations suggest that improper torsion is generally unfavorable for electronic delocalization: the breaking of planarity is increases the energy of delocalization more significantly than the additional overlap of π-orbitals lowers it. Nevertheless, we find that for PNDI-T, improper angles of up to 30° can lead to more favorable energetics than angles of 0°. This observation suggests that it is possible to maintain conjugation at high degrees of torsion. Additionally, simulations in which the dihedral and improper torsions are isolated suggest that energies of the system generally increase more quickly with improper torsion than with conventional dihedral torsion. Altogether, this work shows that judicious consideration of improper torsion (and how it affects the energies predicted by dihedral torsion) using the method described can offer an avenue for more simulating conjugated polymers with greater accuracy than is now possible.

5.1   Introduction

Charges in a π-conjugated polymer can rapidly move through the entirety of a polymer chain. When monomers are coplanar with each other, charges can easily delocalize within polymers.[179,194–196] This delocalization effect gives rise to the high electronic mobility of π-conjugated polymers. Charges are able to delocalize across many monomers at the same time.[14,197–199] As delocalizing over a larger space is energetically favorable for charge carriers, this means that the configuration of even distant charge carriers affects the overall energy of the system. That is, a single conjugated monomer would induce a monomer even a significant distance away towards planarity, provided the monomers in between are coplanar to facilitate delocalization of charge carriers. However, this effect has been relatively neglected in compu-

98

tational study of π-conjugated polymers. Experimental studies of organic electronics have long attempted to examine the extent of electronic delocalization. For example, studies have long been carried out for basic π-conjugated polymers to estimate their "conjugation length", or the number of monomers over which charge carriers can easily delocalize.[198,200,201] However, this approach has become less common is recent years, likely due to both the exploding diversity of π-conjugated polymers and inaccuracy of the methods. Computational study of the materials could be a more accurate avenue for study of long-range interactions between monomers in π-conjugated polymers, as molecular simulations can give atomistic detail into how the molecule is arranged. However, while studies have been carried out to determine spectroscopic effects of breaks in delocalization, the effect of long-range delocalization on morphology (and thus the effects of morphology on charge carrier delocalization) has been overlooked. A key computational tool, molecular dynamics simulation, does not typically take into effect of distant interactions of conjugated polymers.[145,148,151] Given that molecular dynamics simulations predict the morphology of a material in atomistic detail, molecular dynamics simulations are a key tool for probing how long-range interactions affect the morphology of organic electronics, particularly π-conjugated polymers. However, implementing long-range interactions between monomers in π-conjugated polymers is not easily accomplished in molecular dynamics simulations. Molecular dynamics simulations commonly use what is known as a "force field" to determine all interactions between atoms in a system in a computationally efficient way.[69,185,202] A simple 2- to 4-body expression is typically used to compute an interaction term (i.e. Lennard-Jones style interaction). However, no term like this is suitable for simply computing the interaction between distant monomers. Not only are most expressions either highly localized (i.e. bond parameters for directly bonded atoms) or highly general (approximate Van der Waals parameters for every atom

in the system for every other atom in the system), the energetics of distant monomers interacting additionally depends on the orientation of every monomer between the monomers in question. Other styles of molecular dynamics simulation, particularly molecular dynamics based on first principles quantum calculations, are too computationally demanding to be commonly used to determine the morphology of multiple polymer films.[18,19,203] As such, a method for integrating long-range interactions into π-conjugated polymer simulations is desired. The focus of the study in this manuscript is the polymer DPP2F-TT, a donor-acceptor polymer with diketopyrrolopyrrole (DPP) as the acceptor unit, thienothiophene (TT) as the main donor unit, and furans acting as "π-bridges" between the donor and acceptor units. DPP2F-TT is a high-performance example of a popular type of π-conjugated polymer containing DPP.[204,205] The DPP and TT unit have an intermediate conjugated unit between them, but with substantial differences in electron affinity are still expected to significantly interact. Given that the torsion (or lack thereof) between both DPP and TT and the intermediate furan will likely modulate their interaction, however, DPP2F-TT provides an excellent case study of how the morphology and co-planarity of multiple rigid units affects their energetic interactions. Additionally, previous study has indicated that the likely significant interaction between the nonadjacent DPP and TT units result in significantly different overall behavior than an identical polymer with a smaller thiophene unit.[206] This suggests that the interactions of monomers not directly bonded are key for determination of the morphology of DPP2F-TT. Three things are examined in this manuscript. Nonbonded interactions can obscure the overall energy of multi-conjugated ring interaction. We thus first use a previously-developed method shown in Figure 5-1 to isolate nonbonded interactions from effects arising from electronic delocalization in π-conjugated polymers. The energetics of these long-range interactions are presented and their relative importance analyzed. Interactions of rings with one

intermediate ring between them are analyzed, with the expectation that this technique should be applicable to interactions any distance apart. Second, to include the energetics of long-range interactions in molecular dynamics simulations, an approach using collective variable analysis is proposed and implemented. This approach is additionally used to characterize how much the simulations are improved by removal of nonbonded interactions. Finally, we implement our long-range interactions into film-scale molecular dynamics simulations to determine the effects of these long-range interactions on polymer morphology.

5.2   Results and discussion

Nomenclature

A variety of terms and standards to simplify discussion of the following work is described here and shown in Figure 5-2. Given that the interactions are no longer simple two-body interactions in which both monomers act equally upon each other, it is important to be able to easily refer to each monomer in the trimer system. The trimers are thus referred to a monomer 1, 2, and 3, numbering the monomers from left to right as they are drawn in the figures. In figures showing energetics with torsional angle, every single color of plot represents a change in the energy as the dihedral torsion between monomers 1 and 2 is modified. Monomers 1 and 2 are circled in some figures to emphasize that it is the torsion between those two monomers that is being characterized within a singular plot. The torsion between monomer 2 and 3 is held constant within a single color of plot. As dihedral torsion between monomers 2 and 3 is increased, the color of the plot is changed, moving from blue to red. The direction of distant monomers pointed in the same direction can additionally be important to discuss. As such, monomers

pointed in identical direction relative to the adjacent monomer are referred to as being in the syn configuration, while flipping one of the monomers by 180° results in the anti configuration.

Energetics of Long-Range Interaction

First, the energy of interaction between monomers is determined for both dimers and trimers and shown in Figure 5-3. The energy is calculated using a previously reported method to isolate the delocalization energy. Dimer calculations help give a measure of the strength of interactions over a short distance, both as a point of comparison for longer-distance interactions and to help future calculation of the interaction between the distant monomers.145 Only two types of interaction define DPP2F-TT, the interaction between DPP and furan and the interaction between TT and furan. The interaction between DPP and furan is an intensely strong interaction, far stronger than the interaction between other conjugated systems with strong push-pull effects.[208] For comparison, the barrier to torsion between thiophene and another strong acceptor, naphthalenediimide, is nearly half of that than the barrier between DPP and furan. The strong interaction between DPP and furan suggests significant interaction may be possible between DPP and TT. In comparison, the interaction between furan and TT is significantly weaker, an expected outcome for an all-donor pair. The findings emphasize previously reported work suggesting a strong rigidifying effect with significant differences in push-pull character in conjugated polymers. The energy of the interaction with increasing torsion between the 1 and 2 monomers is shown in Figure 5-4. The energy shown is the total energy of the 1, 2, and 3 monomers all interacting without any correction for the nonbonded energy, with the 3 monomer constantly coplanar with the 2 monomer. These plots thus measure the energy of the additional interaction energy that the 3 monomer provides to torsion between the 1 and 2 monomer. Includ-

ing the interaction of a ring not directly involved in torsion between two conjugated monomers can have several kcal/mol of energetic effect. One can think of the torsion between the furan and DPP units as being modified by either adding a TT unit to the furan (Figure 5-4b, top left) or by adding another furan unit to the DPP (Figure 5-4b, bottom right). The additions of these two different rings have substantially different effects on the energy of the torsion between the DPP and furan conjugated rings. When the thienothiophene is added to make a DPP-furan-TT trimer, the total barrier height (difference in energy between a 90° torsion and 0° torsion) of the DPP-furan interaction increases substantially. The barrier grows from approximately 8 kcal/mol (Figure 5-4a, left) to nearly 11 kcal/mol, an increase of 3 kcal/mol or over a third of the energy from the simple dimer interaction. In contrast, little change to the barrier height is seen when another furan is added. If anything, the barrier height decreases slightly, plausibly the effect of adding another donor to counterbalance the strong acceptor. However, what is accentuated is the discrepancy in energy between the two conformations in which the conjugated rings are coplanar, 0° and 180°. The difference in energy between 0° and 180° is the largest for any trimer system in furan-DPP-furan, about 2.5 kcal/mol. The high discrepancy between the energy of the 0° and 180° conformations of the trimer system suggests potential strong preferences for specific orientations of the polymer, though given the strength of steric clashes steric effects cannot be discounted from Figure 5-4 alone.

Similar trends are seen for the modification of the TT-furan torsion with the addition of a DPP ring or another furan. The torsional barrier again significantly increases with the addition of the DPP ring. For the TT-furan-DPP trimer, the initial torsional barrier of under 4 kcal/mol (Figure 5-4a, right) is increased to over 6 kcal/mol (Figure 5-4b, bottom left). The change in maximum interaction energy of over 50% for TT-furan is greater than the difference in barrier

height previously measured between P3HT and PNDI-T (a donor-acceptor polymer with a high push-pull effect, expected to be highly rigid), fundamentally modifying the nature of the interaction of the furan-TT unit from fairly labile to highly rigid. Thus, treatments of the torsions of polymers like DPP2F-TT which ignore the effects of the DPP and TT unit on each other (i.e. either eliminating the unit entirely or keeping it constantly planar) will be ignoring almost half of the total energy of interaction between conjugated rings. The addition of a second furan hardly seems to affect the energy of torsion between the first furan and TT at all. However, it is not clear from these plots whether there is some underlying effect that is obscured by nonbonded interactions. Additionally, while these plots show the additional torsional energy when 3 conjugated rings are considered, this plot does not yet demonstrate the effects of torsion between the 2 and 3 conjugated ring on the torsional energetics between the 1 and 2 conjugated rings. The energies of the interaction between the 1 and 3 conjugated rings—the two monomers in a trimer not directly bonded—with increasing torsion between the 2 and 3 conjugated rings is shown in Figure 5-5. The energies are calculated by subtracting the unmodified strength of the total unmodified energy of the 1-2 and 2-3 interactions from the total energy of a trimer with a certain degree of torsion. Thus, the remaining energy is the total energy of interaction between the 1 and 3 dimers. Four plots are shown in different colors. The blue plot represents the energy of modifying the torsion between monomers 1 and 2 while monomer 3 is perfectly planar with monomer 2. As the plots shift towards red, the angle between monomers 2 and 3 increases. At 90° of torsion between monomers 2 and 3, the plot is red. The energy of interaction between these monomer is representative of interactions of monomers not directly bonded in a conjugated material. The energy of interaction between the 1 and 3 monomer is substantial, but does appear to be somewhat affected by the nonbonded interactions. A prime example is the behav-

ior of torsion between diketopyrrolopyrrole and furan as the torsion between the thienothiophene and furan is modified, as shown in Figure 5-5a. The maximum energetic interaction between monomers 1 and 3 is approximately 3 kcal/mol. This strength of interaction is approximately the same are the strength between directly bonded monomers in a homopolymer (e.g. P3HT). As these interactions are typically the strongest interactions within a homopolymer chain, the interaction between these distant polymers is still of high interest in conjugated materials. At the same time, interactions between the 1 and 3 polymer appear to be modified by nonbonded interactions. The difference in energy between the $0°$ and $180°$ conformations, differences which should not be due to the fundamental delocalization interaction between the monomers, is 1.5 kcal/mol. Previous work has suggested that such high differences between states which should have highly similar delocalization interactions suggest nonbonded interactions are interfering with the energetics. Additionally, the interaction between the "π-bridge" appears low, but the exact nature of the interaction is unclear. While the interaction across the thienothiophene unit appears low (typically less than 0.5 kcal/mol), the interaction between π-bridges across the DPP unit is highly counterintuitive, with a spike in energy when the monomers are directed in the syn configuration. To clarify these issues, the interaction of the 1 and 3 monomers with nonbonded interactions eliminated must be used. The energy of interaction between the 1 and 3 monomers after correction for nonbonded interactions is shown in Figure 5-6. A number of differences are apparent wen nonbonded energy is accounted for. Firstly, the energetic differences between the $0°$ and $180°$ conformation of the polymer largely disappears. For example, in Figure 5-6a, the difference between energies between $0°$ and $180°$ as demonstrated in Figure 5-5a is eliminated. However, while the minima are identical and evenly placed at 0 and $180°$, the maxima shift with increasing torsion between the furan and thienothiophene. While the energy achieves

a perfect maximum at 90° and 180° when no dihedral torsion is considered, twists between the furan and thienothiophene shift the maximum energy towards 180°. These conformations of the dimers represent configurations in which the 1 and 3 monomers are far away from planarity with each other, while the lower energy shifting occurs while the monomers are coplanar with each other, with a twisted monomer between them. To elucidate, consider the orientations of the monomers in a DPP-furan-TT trimer, where the 1 monomer is DPP, the 2 monomer is furan, and the 3 monomer is TT. When the TT monomer is perfectly coplanar with the furan, the DPP has no energetic preference between 0° and 180°. Once the TT monomer begins to twist, however, the energy begins to skew from perfect symmetry. When the 3 monomer, TT, is twisted from the furan from 60°, energy is slightly more favorable when the 1 and 3 monomers are directly coplanar with each other, even though both are separated by a highly twisted intermediate monomer. A similar shift is seen when the trimer is reversed, TT-furan-DPP. This finding correlates well with findings from naphthalene diimide polymers, where charge carriers were still able to delocalize across monomers bridged with several intermediate π-bridges. Removing the nonbonded interactions thus unveils an interaction between distant monomers previously unable to be characterized, as they were obscured with conflating nonbonded interactions. In addition, the interactions between π-bridges across both DPP and TT appears distinctive. The interaction between the DPP and TT units across the π-bridge bear a pattern familiar for the energetics of π-conjugated polymers under torsion: lower energy at planarity, higher energy when planarity is broken. In contrast, the interactions between π-bridges appear significantly more idiosyncratic. The energy of interaction between π-bridges appears significantly more dependent on the orientation of the monomers to each other (in the case of furan-TT-furan) and to the central monomer (as in the case of furan-DPP-furan). In furan-TT-furan, the interaction

without correction for nonbonded energy is minimal, as shown in Figure 5-5b. After correction for nonbonded interactions, however, a stronger pattern emerges. First, the overall potential energetic penalty increases sharply (2 kcal/mol). Additionally, the strongest deviations of from expectation locations of maxima and minima (minimum at 0°, maximum at 90°) occurs for furan-TT-furan. Instead of the greatest energetic penalty being at 90°, the greatest energetic penalty is at when both furans are twisted at 60° in opposite directions. The shift from an energetic maximum at 90° of torsion to maximum at 60° of torsion suggests that a single furan is strongly interacting with both monomers (both TT and the other furan), regardless of the conformation of the intermediate thienothiophene. That is, even if the intermediate TT is twisted to an extent that electronic delocalization is largely blocked between TT and a furan ring, both furans still strongly interact without an intermediate planar ring to pass along electronic delocalization. The orientational of three monomers interacting equally must thus be considered in a furan-TT-furan system. This behavior lies in contrast to the DPP-furan-TT system. In that system, the confor-mation of the furan relative to the other two monomers is only relevant in terms of how easily monomer 3 can interact with monomer 1. Finally, the behavior of furan-DPP-furan is analyzed. This interaction appears to be the overall strangest of the three interactions, with a significant increase when both furans are pointed in the syn direction both without and with correction for nonbonded interactions. The trimer configuration of those monomers thus appears highly idiosyncratic to the relative orientations of the 1 and 3 monomers, in this case both furans. How-ever, when the nonbonded energies are removed, the delocalization energy shows a clearer trend. The energy associated with torsion of the 3 monomer results in an initial energetic favor-ability, but as planarity continues to be broken in the monomers becomes unfavorable overall. Given the strength of DPP as an acceptor unit and strength of the interaction between a dimer

of DPP and furan, it seems likely that the idiosyncracies are due to it being unfavorable for DPP

to be unable to delocalize across both donor units. Finally, the relative accuracy of accounting

for the nonbonded interactions is demonstrated in Figure 5-7. Given the novel and idiosyncratic

behaviors shown in some of the trimer systems, it is necessary to show that the removal of

nonbonded interactions is beneficial. All trimer systems show an improvement in accuracy of

their characterization when nonbonded forces are removed. The starkest improvement in accu-

racy occurs in furan-DPP-furan, the trimer system with the highest amount of steric hindrance

overall. However, DPP-furan-TT and furan-TT-furan both see small improvements in accuracy,

suggesting that the equality between the energies of the $0°$ and $180°$ positions and skewing of

the maxima from $90°$ are real effects.

5.3   Conclusion

This work sought to understand the effect of improper torsion on the energetics of three

model polymers: P3HT, PTB7, and PNDI-T. Our simulations suggest that varying degrees of

improper torsion would be common in the polymer chains that compose a solid sample. This

finding is significant because of how improper torsion affects conjugation along a polymer chain.

First, improper torsion decreases conjugation when planarity is broken. Second, improper tor-

sion increases electronic delocalization if additional overlapping of the π-orbitals is induced. In

general, we find that the first effect is stronger than the second, and thus an increase in im-

proper torsion generally results in a greater energetic barrier to torsion for all polymers except

PNDI-T (when large improper angles are induced). As a result, improper torsion is generally an

obstacle for electronic delocalization. Additionally, we find that energetic penalties from steric

interactions can significantly obscure the energetic penalties associated with electronic conjuga-

tion relative to increasing improper torsion. Therefore, by modifying our computational method to isolate the energy related to electronic delocalization, we show that the barrier to torsion decreases as improper angle increases. Similarly, by isolating the effects of both styles of torsion, we determine that improper torsion generally imposes a stronger energetic penalty compared to dihedral torsion. However, the complex interplay between steric interactions, dihedral torsion, and improper torsion results in some exceptions. In particular, simulations of PNDI-T suggest that it is possible for adjacent monomers in a conjugated backbone to be highly twisted and still maintain conjugation. Finally, we show that a computational method that considers both improper and dihedral torsion can be used to more accurately simulate all three model polymers, although the increase in accuracy for some polymers (e.g., the F-out variation of PTB7, PNDI-T) mainly stem from the correlation to steric effects. Our findings indicate that the inclusion of a modified characterization of improper torsion helps better describe the energetics of conjugated polymers. Thus, consideration of the improper torsion within a conjugated system is required for highly accurate models of semiconducting polymers. This importance stems from the effect of improper torsion on both the overlap of π-orbitals as well as internal disruption of π-systems. In addition, improper torsion can directly affect dihedral torsion. Therefore, improper torsion appears to be of particular importance in polymer structures with large amounts of steric hindrance. Improper torsion is even more so likely to be important when high degrees of torsion are present in general (e.g., films under strain, polymers deposited from melt, films annealed at high temperatures). While description of improper torsion improves the accuracy of modeling conjugated polymers, further steps should be taken to quantify the effects of improper torsion. Judicious exploration of the placement of additional hydrogen atoms to optimally block steric hindrance would be preferred, as high steric hindrance can still cause difficulties in modeling. For

example, we show that the behavior of PNDI-T differs greatly from both P3HT and PTB7 when improper torsion is introduced between two monomers. Further exploration of highly sterically hindered polymers (particularly D–A polymers with asymmetric monomers) can provide information about the disruption of electronic delocalization in conjugated polymers. For example, our findings suggest that PNDI-T can maintain favorable electronic delocalization at high degrees of improper torsion. Therefore, further investigation of improper torsion in D–A polymers elucidate the energetic effects of π-orbital overlap. Additional work in this area could offer significant insights into the high mobilities of modern D–A polymers, many of which are amorphous or take advantage of short-range aggregation. Thus, accurate understanding of how chemical structure affects the morphology (as mediated by chain conformation and packing structure) of a polymer solid offers an avenue for improving predictions of its physical (e.g., electronic and mechanical) properties. In doing so, computational simulations of conjugated polymers can be used to facilitate the rational design of new polymeric materials.

5.4   Materials and Methods

Isolation of Delocalization Energy

A method to separate out the energies related to delocalization from the other energies in the system—here lumped together as the nonbonded energies—has been previously reported, as is presented here with modifications to analyze long-range energetics related to torsion. The previously reported method to extract the energy related to delocalization of two conjugated rings at once is additionally used to determine the energy related to delocalization across multiple rings. Trimers were used as the smallest oligomeric form in which conjugated

rings not directly bonded to each other could interact. To determine the energy of delocalization, two separate forms of the trimer form were analyzed. First, a simple torsional scan of the trimer system was performed.[145,146,151] A torsional scan is the measurement of the energy of the planar trimer, then the energy of the system is calculated by a quantum mechanical method. The RI-MP2 method was used with the cc-pVTZ basis set. This method of quantum mechanical calculation was chosen because it has been frequently used to characterize torsion in conjugated polymers in the past, and can estimate nonbonded interactions without need for special modification.[145,148,207] It is important to note, however, that this method could be used with any quantum mechanical method. All torsions between $0°$ and $180°$ were characterized for both torsions between individual conjugated rings with $10°$ spacing, for a total of 361 conformational characterizations. The process was then repeated with a version of the trimer with nonphysical hydrogen atoms added to block the movement of π-electrons between conjugated rings. Two nonphysical hydrogen atoms were added to the central conjugated ring in the direction of the normal vector of the ring. The chemically modified version of the trimer with two nonphysical hydrogens is referred to as the "hydrogenated trimer." The hydrogen atoms block any electronic delocalization between the two rings from occurring. The two hydrogen atoms were added to opposing sides of the central monomeric unit to minimize any interactions between the two hydrogen atoms. To correct for the energies of the addition of nonphysical hydrogens, the energy of the outermost rings bonded to a single methyl group with the hydrogens adjusted in position such that one of the hydrogen atoms was placed in the same orientation as the nonphysical hydrogen in the hydrogenated trimer and the other two hydrogens pointed in the same position as the bonded atoms to the equivalent carbon atom in the hydrogenation dimer. After correcting for the energy of the nonphysical hydrogens, subtracting the energy of the hydrogenated trimer un-

der torsion from the energy of the full trimer provides an estimation of the delocalization energy which is not present in the hydrogenated trimer.

Isolation of Interaction Energy of the Terminal Conjugated Rings

While the energy between bonded conjugated rings can be well characterized in the past, the energy between conjugated rings not directly bonded to each other has been relatively unexplored. As such, a determination of the energy of interaction between the terminal conjugated rings of a trimer with varying interring torsions was sought, excluding any interactions with the central ring. To do so, the method from the previous section was used to isolate the delocalization energy across all three monomers. Additionally, the total delocalization effects between the directly bonded rings (the terminal rings of the trimer and the central ring) were calculated. The energies of the delocalization energy between the directly bonded rings were then subtracted from the total delocalization energy of the system, leaving only the energy of interaction between the two terminal conjugated rings.

Determination of Accuracy

To determine whether using the method of isolating delocalization energy compared to the method using the total energy related to dihedral torsion (i.e. torsional scan) is an improvement, a simple method was used to determine the relative accuracy of each method. Each possible trimer in DPP2F-TT was simulated—DPP-furan-TT, furan-TT-furan, and furan-DPP-furan. To solely determine the energetics of the intermonomer torsion, the internal coordinates of each conjugated ring were held constant using the RIGID package.189 The trimers had any dihedral torsions restricting the rotation of the bonds removed, and the trimers were allowed to

freely rotate in a simulation box large enough to minimize self-interaction effects (300 Å) at 800 K. Random snapshots of the trimer conformations were taken every 100 ps, and the energy of the conformation was characterized using the RI-MP2 method with a cc-pVTZ basis set. The energy of each conformation was then characterized. The simple two-conjugated ring interactions were characterized using the delocalization energy, as this has been demonstrated in the past to be more accurate. The dihedral energy fit to the total energy of the torsional scans and the pure energy related to delocalization are then used to characterize the energy due to the two terminal conjugated rings interacting. To incorporate the relationship between the two torsions in the monomer, the PLUMED packaged was used with an external energetic bias (akin to implementing external energy for i.e. a metadynamics sampling run).186 The delocalization energy between the terminal monomers interacting was included through this external bias by relating the external added energy to correspond to two collective variables—the same torsions characterized by the delocalization energy—and apply an external energy based on the value of those two torsions and the energy they correspond to based on the torsional scans. In this way, the ability of the force fields to represent the quantum mechanical calculations they were based on is determined.

5.5   Acknowledgements

Chapter 5, in full, is a reprint of material in preparation to be published in: **Kleinschmidt**

AT, Ramji R, Chen AX, Pascal TA, Lipomi DJ. Correlation of Energetics in Distant Monomers of

π-Conjugated Polymers. *In Review*. The dissertation author was first author of this paper.
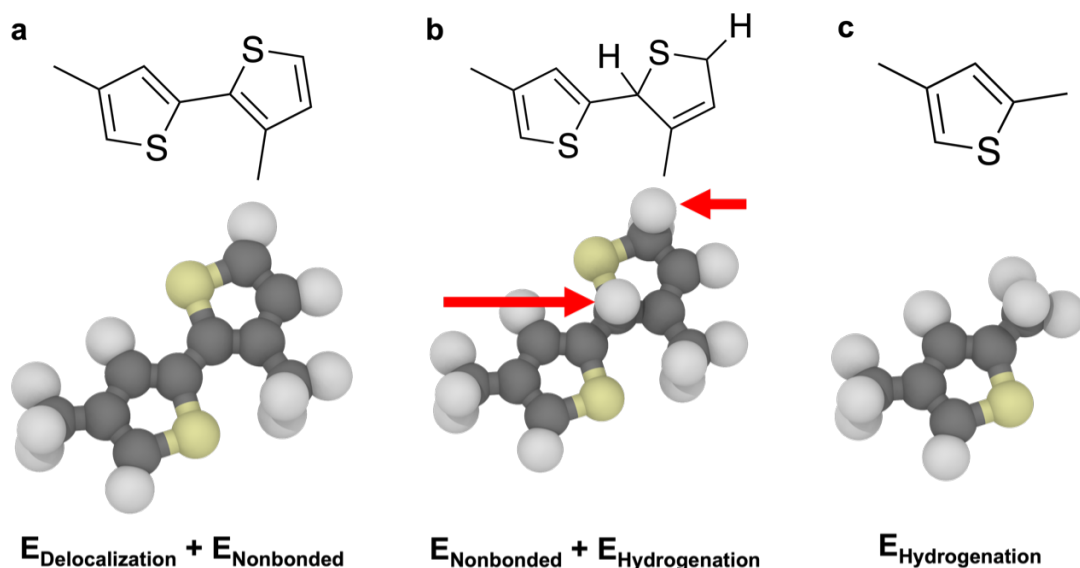
Figure 5.1: Overview of method to isolate the energy related to charge carrier delocalization in conjugated materials. In Figure 5-1a, a basic quantum mechanical calculation of the total energy of conjugated rings interacting is performed. Side chains are replaced with simple methyl groups, as they add substantial cost to quantum mechanical calculations and provide relatively little contributions to the interactions of the conjugated rings. In Figure 5-1b, the conjugated rings are modified by adding hydrogens to the central conjugated ring at the points connecting the rings together. This blocks π-delocalization of charge carriers between conjugated rings, providing an estimate of only the other energies of the system, $E_{Nonbonded}$, and the energy related to the addition of the hydrogen atoms, $E_{Hydrogenation}$. To provide a correction for the energy of the addition of hydrogen atoms in unphysical positions, the terminal rings in the trimer are bonded to a methyl group. In the methyl group, one hydrogen atom is placed in the same position as the hydrogen atom added to the central monomer, with the other two hydrogens pointed in the same direction as the atoms that carbon would be bonded to in the central ring. This provides an estimation for $E_{Hydrogenation}$. This estimation of $E_{Hydrogenation}$ is subtracted off of the energy of the hydrogenation dimer to provide an estimation of $E_{Nonbonded}$, which is subtracted off the total energy of the unmodified trimer system to provide an estimation of $E_{Delocalization}$.
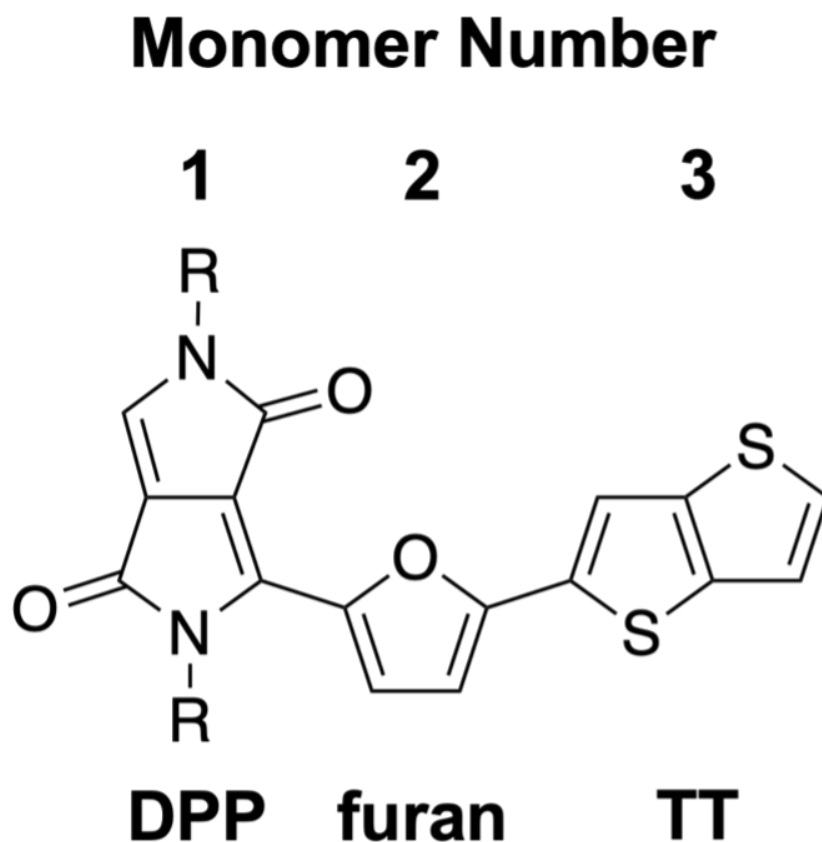
Figure 5.2: Overview of nomenclature used in the rest of the manuscript. Any monocolor plot of lines shows the torsion between the first two monomers shown in the pictoral representation of the trimer. The monomers are numbered from left to right based off the pictoral diagram, which represents the order in which torsion is shown (monocolor plots show the energetic effects of torsion between monomers 1 and 2, a change in color indicates torsion between monomers 2 and 3). The trimer is referred to in the same order that the pictoral representation of the trimer shows. The above trimer would thus be referred to as DPP-furan-TT.
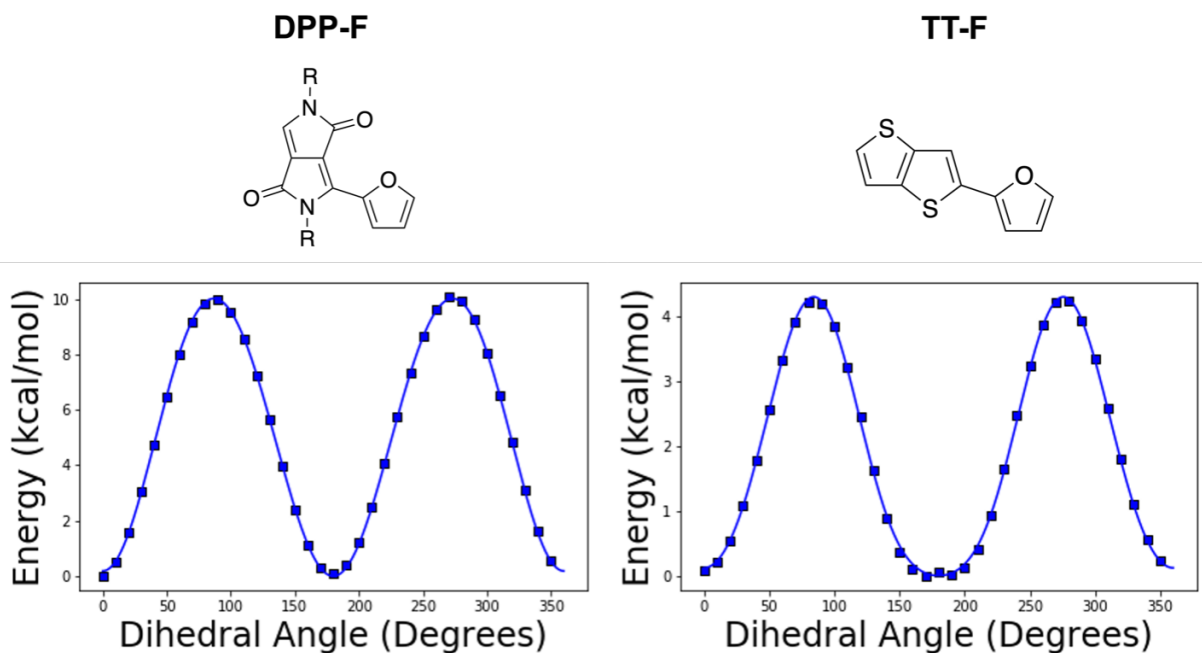
Figure 5.3: The energetics of two conjugated rings directly bonded to each other interacting in DPP2F-TT. The nonbonded energy is removed based on a previously reported method to isolate the energy related to delocalization in the conjugated rings. Only two types of interactions between directly bonded conjugated rings occur in DPP2F-TT. The interaction between TT and furan is relatively weak, approximately the maximum energy of interaction between conjugated rings in P3HT. In contrast, the interaction between DPP and furan is by far stronger than the interaction between previously reported conjugated rings with strong push-pull effects, such as in poly-napthalenediimide materials.
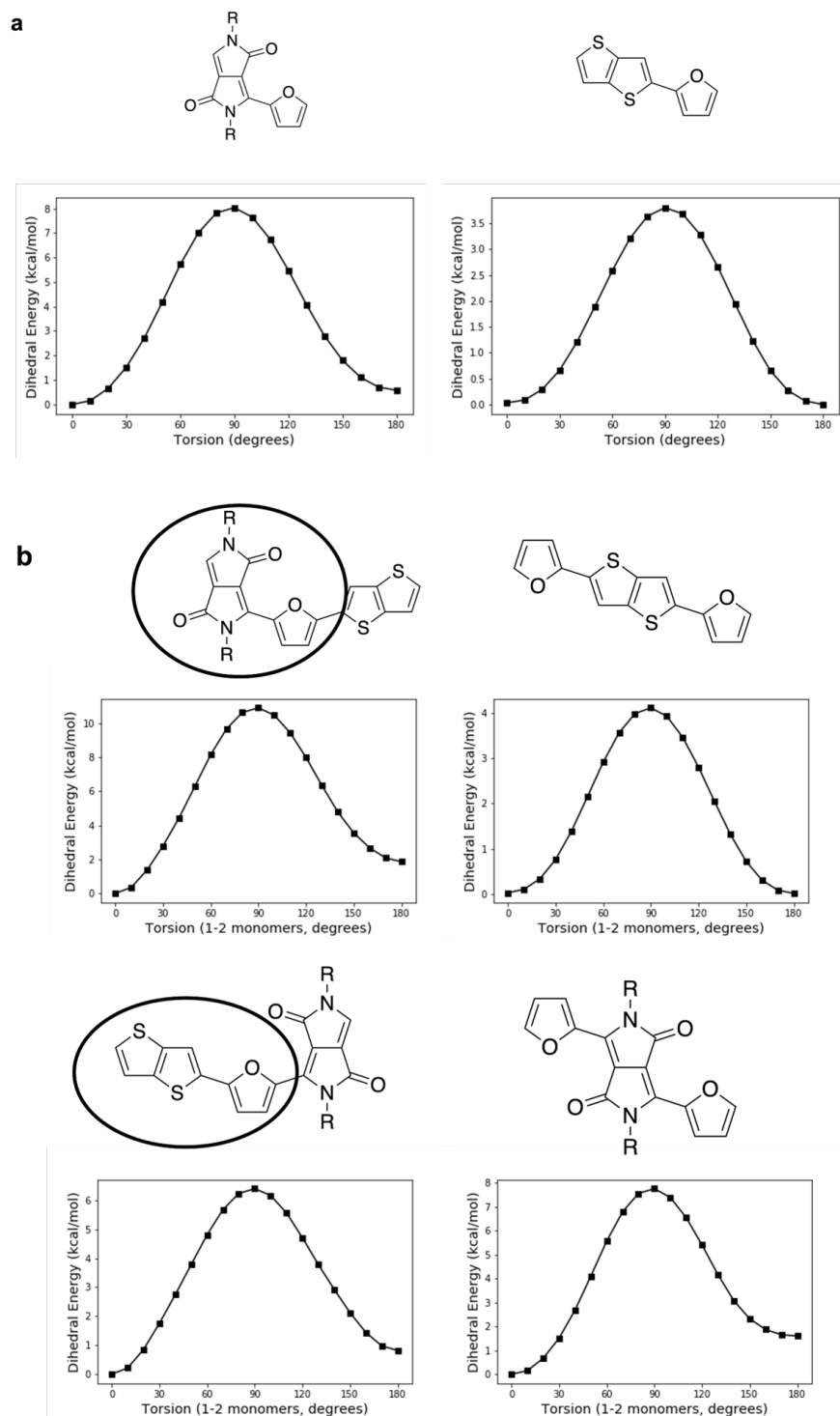
Figure 5.4: Estimation of how the introduction of a third ring changes the total energy of the system compared to a two-ring system. In Figure 5-4a, the total energy of two conjugated rings is shown for both DPP-furan and TT-furan. In Figure 5-4b, the total energy of three conjugated rings interacting is shown for DPP-furan-TT, furan-TT-furan, and furan-DPP-furan.
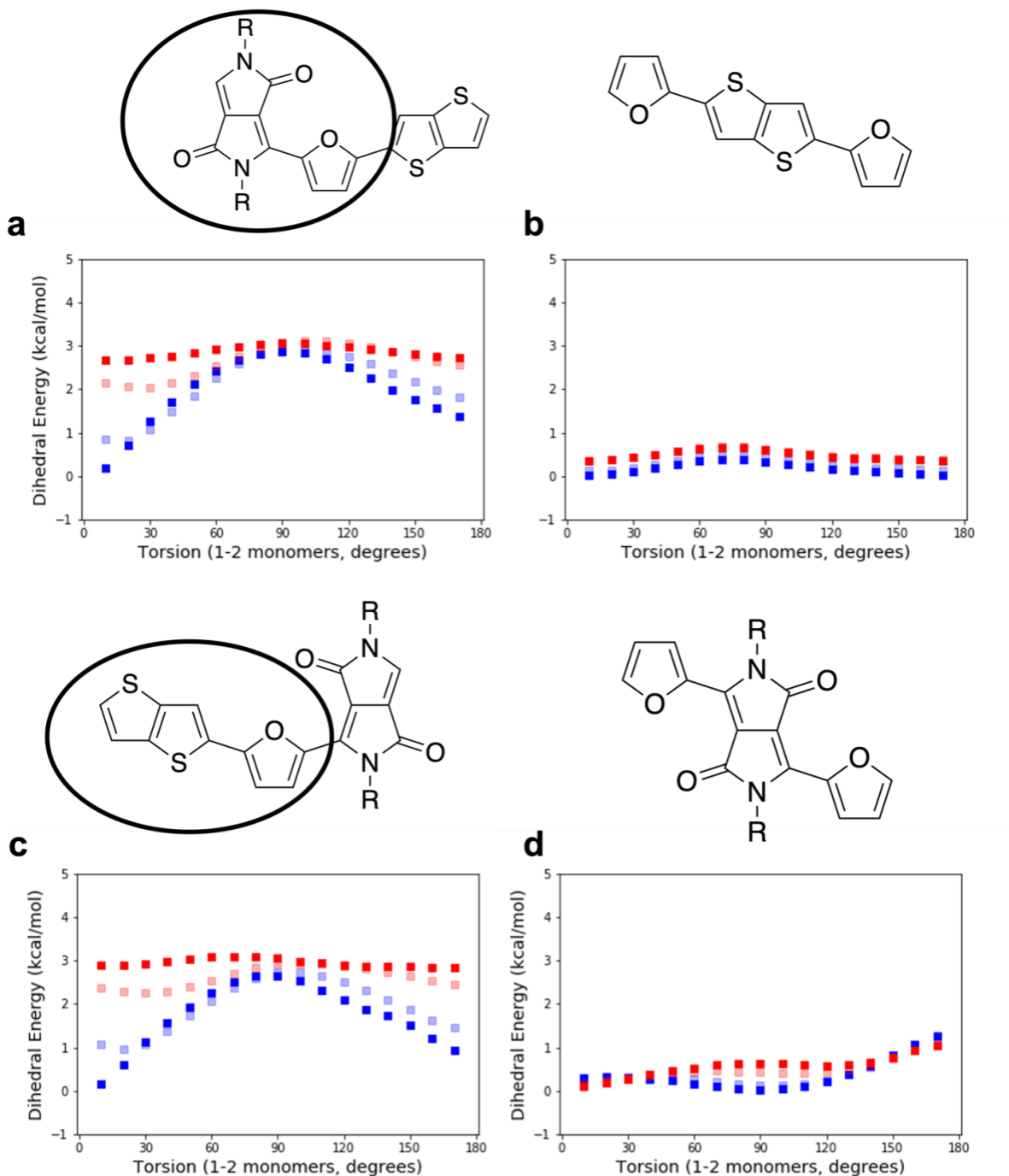
Figure 5.5: The estimated total energy of interaction between the terminal (1 and 3) monomers in the trimer system. Each color denotes the energy for a particular torsion between the rightmost (2 and 3) monomers shown, with dark blue showing a 0° torsion, light blue showing a 30° torsion, light red showing a 60° torsion, and dark red showing 90° torsion.
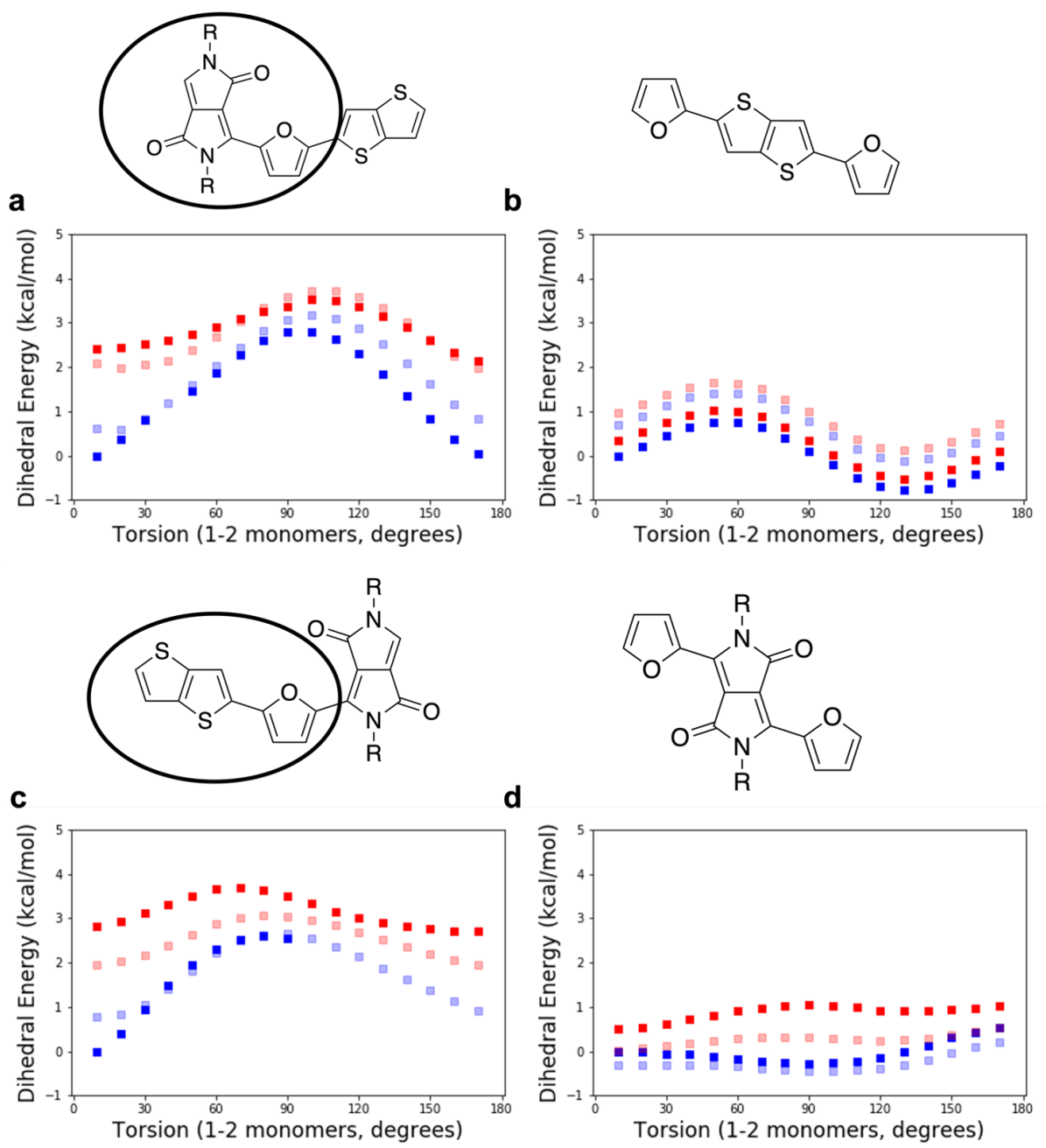
Figure 5.6: Estimation of the pure energy of interaction due to charge carrier delocalization between the terminal monomers in the trimer system. Each color denotes the energy for a particular torsion between the rightmost (2 and 3) monomers shown, with dark blue showing a 0° torsion, light blue showing a 30° torsion, light red showing a 60° torsion, and dark red showing 90° torsion
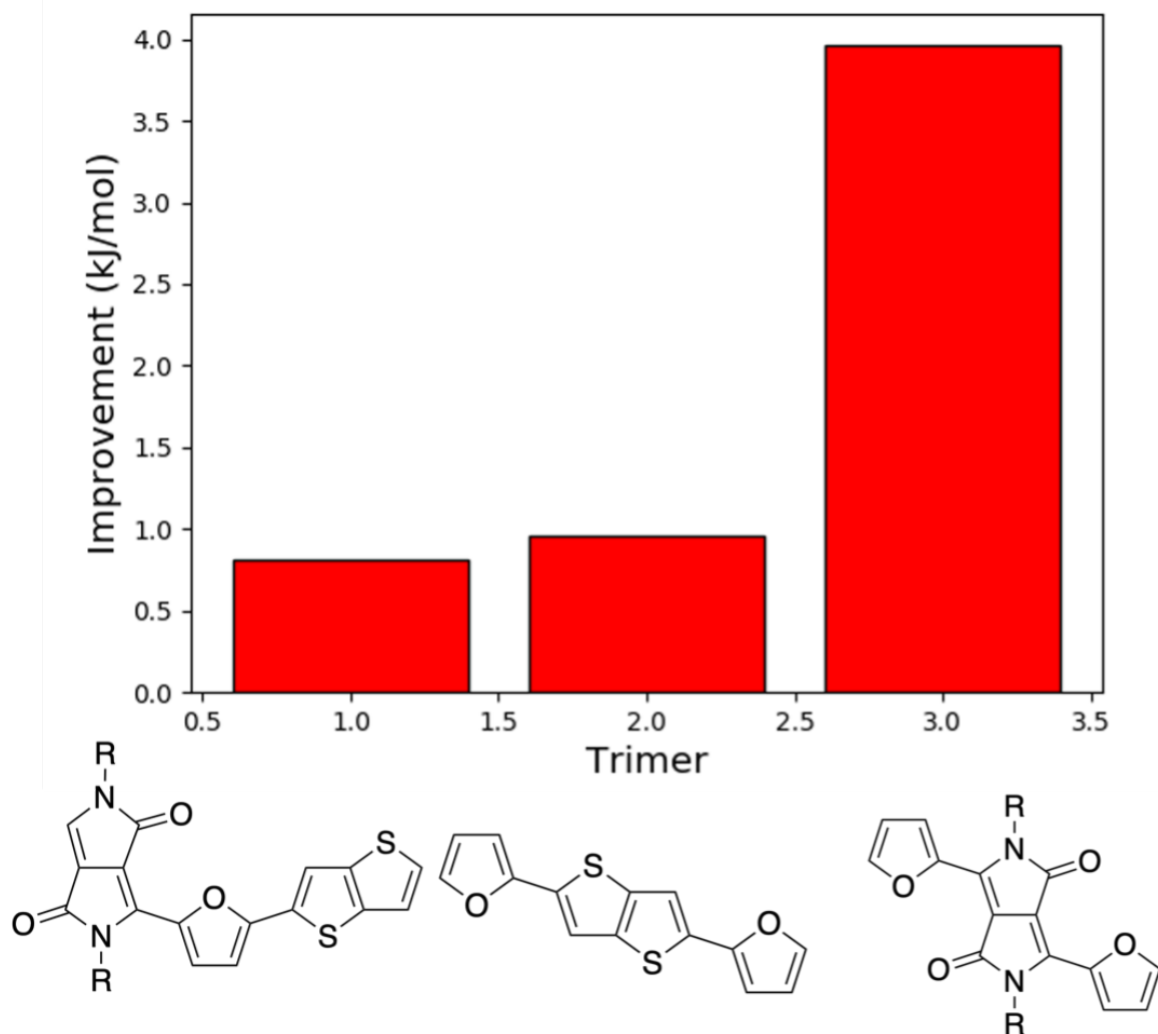
Figure 5.7: Relative accuracy of the pure delocalization energy compared to the total energy not using the method described in Figure 5-1. The method described in Figure 5-1 was more accurate for every trimer within DPP2F-TT. The greatest improvement in accuracy was seen for furan-DPP-furan, when steric effects appear highest.

Figure 5.8: Change in 1-2 torsional barrier as 2-3 torsion increases (x-axis).

Bibliography

(1)   de Pablo, J. J.; Jackson, N. E.; Webb, M. A.; Chen, L.-Q.; Moore, J. E.; Morgan, D.; Jacobs, R.; Pollock, T.; Schlom, D. G.; Toberer, E. S. New Frontiers for the Materials Genome Initiative. *npj Comput. Mater. 2019 51* **2019**, *5* (1), 1–23. https://doi.org/10.1038/s41524-019-0173-4.
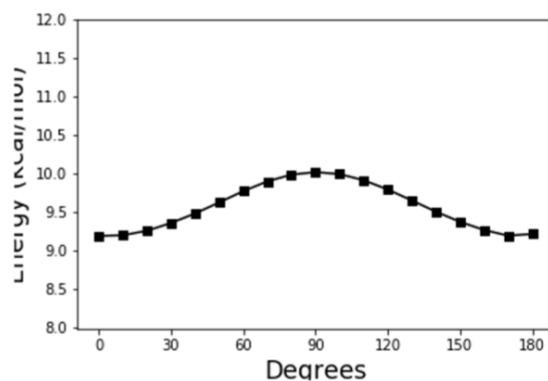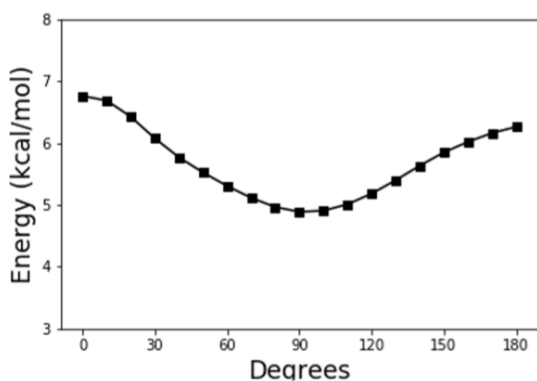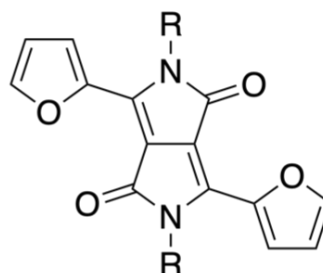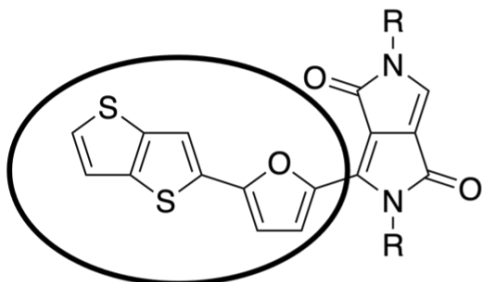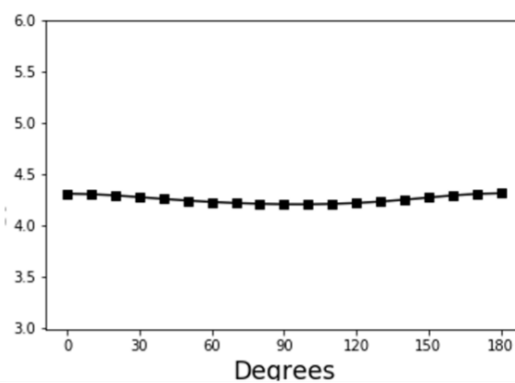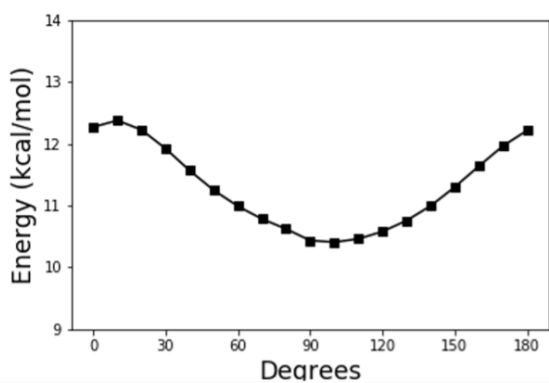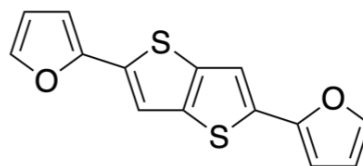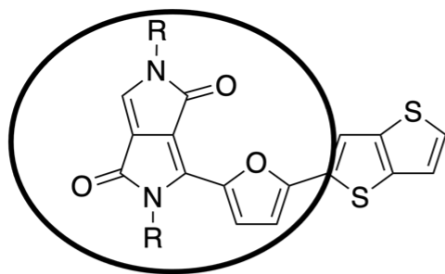
(2)   Ehrenberger, T.; Cantley, L.; Yaffe, M. Computational Prediction of Protein-Protein Interactions. *Methods Mol. Biol.* **2015**, *1278*, 57–75. https://doi.org/10.1007/978-1-4939-2425-7_4.

(3)   Gebhardt, J.; Kiesel, M.; Riniker, S.; Hansen, N. Combining Molecular Dynamics and Machine Learning to Predict Self-Solvation Free Energies and Limiting Activity Coefficients. *J. Chem. Inf. Model.* **2020**, *60* (11), 5319–5330. https://doi.org/10.1021/ACS.JCIM.0C00479.

(4)   Summers, A. Z.; Gilmer, J. B.; Iacovella, C. R.; Cummings, P. T.; McCabe, C. MoSDeF, a Python Framework Enabling Large-Scale Computational Screening of Soft Matter: Application to Chemistry-Property Relationships in Lubricating Monolayer Films. *J. Chem. Theory Comput.* **2020**, *16* (3), 1779–1793. https://doi.org/10.1021/ACS.JCTC.9B01183.

(5)   Shih, C. Y.; Wu, C.; Shugaev, M. V.; Zhigilei, L. V. Atomistic Modeling of Nanoparticle Generation in Short Pulse Laser Ablation of Thin Metal Films in Water. *J. Colloid Interface Sci.* **2017**, *489*, 3–17. https://doi.org/10.1016/J.JCIS.2016.10.029.

(6)   Hollingsworth, S. A.; Dror, R. O. Molecular Dynamics Simulation for All. *Neuron* **2018**, *99* (6), 1129–1143. https://doi.org/10.1016/j.neuron.2018.08.011.

(7)   Harrison, R. L. Introduction to Monte Carlo Simulation. *AIP Conf. Proc.* **2009**, *1204*, 17–21. https://doi.org/10.1063/1.3295638.

(8)   Noé, F.; Tkatchenko, A.; Müller, K.-R.; Clementi, C. Machine Learning for Molecular Simulation. *Annu. Rev. Phys. Chem* **2020**, *71*, 361–390. https://doi.org/10.1146/ANNUREV-PHYSCHEM-042018-052331.

(9)   Argaman, N.; Makov, G. Density Functional Theory-an Introduction. **1999**.

(10)   Wang, K. F.; Wang, B. L.; Kitamura, T. A Review on the Application of Modified Continuum Models in Modeling and Simulation of Nanostructures. *Acta Mech. Sin. 2015 321* **2015**, *32* (1), 83–100. https://doi.org/10.1007/S10409-015-0508-4.

(11)   Ducharne, B.; Juuti, J.; Bai, Y. A Simulation Model for Narrow Band Gap Ferroelectric Materials. *Adv. Theory Simulations* **2020**, *3* (9), 2000052. https://doi.org/10.1002/ADTS.202000052.

(12)   Nasir, S. N. F. M.; Ullah, H.; Ebadi, M.; Tahir, A. A.; Sagu, J. S.; Teridi, M. A. M.

New Insights into Se/BiVO4 Heterostructure for Photoelectrochemical Water Splitting: A Combined Experimental and DFT Study. *J. Phys. Chem. C* **2017**, *121* (11). https://doi.org/10.1021/ACS.JPCC.7B01149.

(13)   Li, H.; Henkelman, G. Dehydrogenation Selectivity of Ethanol on Close-Packed Transition Metal Surfaces: A Computational Study of Monometallic, Pd/Au, and Rh/Au Catalysts. *J. Phys. Chem. C* **2017**, *121* (49), 27504–27510. https://doi.org/10.1021/ACS.JPCC.7B09953.

(14)   Falek, W.; Benali-Cherif, R.; Golea, L.; Samai, S.; Benali-Cherif, N.; Bendeif, E. E.; Daoud, I. A Structural Comparative Study of Charge Transfer Compounds: Synthesis, Crystal Structure, IR, Raman-Spectroscopy, DFT Computation and Hirshfeld Surface Analysis. *J. Mol. Struct.* **2019**, *1192*, 132–144. https://doi.org/10.1016/J.MOLSTRUC.2019.04.084.

(15)   Michaels, W.; Zhao, Y.; Qin, J. Atomistic Modeling of PEDOT:PSS Complexes I: DFT Benchmarking. *Macromolecules* **2021**, *54* (8), 3634–3646. https://doi.org/10.1021/ACS.MACROMOL.1C00351.

(16)   Naserifar, S.; Brooks, D. J.; Goddard, W. A.; Cvicek, V. Polarizable Charge Equilibration Model for Predicting Accurate Electrostatic Interactions in Molecules and Solids. *J. Chem. Phys.* **2017**, *146* (12), 124117. https://doi.org/10.1063/1.4978891.

(17)   Lamoureux, G.; Roux, B. Modeling Induced Polarization with Classical Drude Oscillators: Theory and Molecular Dynamics Simulation Algorithm. *J. Chem. Phys.* **2003**, *119* (6), 3025. https://doi.org/10.1063/1.1589749.

(18)   Pastore, G.; Smargiassi, E.; Buda, F. Theory of *Ab Initio* Molecular-Dynamics Calculations. *Phys. Rev. A* **1991**, *44* (10), 6334. https://doi.org/10.1103/PhysRevA.44.6334.

(19)   Iftimie, R.; Minary, P.; Tuckerman, M. E. Ab Initio Molecular Dynamics: Concepts, Recent Developments, and Future Trends. *Proc. Natl. Acad. Sci.* **2005**, *102* (19), 6654–6659. https://doi.org/10.1073/PNAS.0500193102.

(20)   Mann, A. Core Concept: Nascent Exascale Supercomputers Offer Promise, Present Challenges. *Proc. Natl. Acad. Sci.* **2020**, *117* (37), 22623–22625. https://doi.org/10.1073/PNAS.2015968117.

(21)   Rosenthal, J. S. Parallel Computing and Monte Carlo Algorithms. *Far East J. Theor. Stat.* **2000**, *4*, 207–236.

(22)   Pastor, R. W.; Brooks, B. R.; Szabo, A. An Analysis of the Accuracy of Langevin and Molecular Dynamics Algorithms. *http://dx.doi.org/10.1080/00268978800101881* **2006**, *65* (6), 1409–1419.

https://doi.org/10.1080/00268978800101881.

(23)   Rodger, P. M. On the Accuracy Of Some Common Molecular Dynamics Algorithms. *Mol. Simul.* **2006**, *3* (5–6), 263–269. https://doi.org/10.1080/08927028908031379.

(24)   Grubmüller, H.; Heller, H.; Windemuth, A.; Schulten, K. Generalized Verlet Algorithm for Efficient Molecular Dynamics Simulations with Long-Range Interactions. *http://dx.doi.org/10.1080/08927029108022142* **2006**, *6* (1–3), 121–142. https://doi.org/10.1080/08927029108022142.

(25)   Winger, M.; Trzesniak, D.; Baron, R.; Gunsteren, W. F. van. On Using a Too Large Integration Time Step in Molecular Dynamics Simulations of Coarse-Grained Molecular Models. *Phys. Chem. Chem. Phys.* **2009**, *11* (12), 1934–1941. https://doi.org/10.1039/B818713D.

(26)   Fincham, D. Choice of Timestep in Molecular Dynamics Simulation. *Comput. Phys. Commun.* **1986**, *40* (2–3), 263–269. https://doi.org/10.1016/0010-4655(86)90113-X.

(27)   Hafner, J. Atomic-Scale Computational Materials Science. *Acta Mater.* **2000**, *48* (1), 71–92. https://doi.org/10.1016/S1359-6454(99)00288-8.

(28)   Panagiotopoulos, A. Z.; Panagiotopoulos1-, A. Z. Direct Determination of Phase Coexistence Properties of Fluids by Monte Carlo Simulation in a New Ensemble. *https://doi.org/10.1080/00268978700101491* **2006**, *61* (4), 813–826. https://doi.org/10.1080/00268978700101491.

(29)   Panagiotopoulos, A. Z.; Quirke, N.; Stapleton, M.; Tildesley, D. J. Phase Equilibria by Simulation in the Gibbs Ensemble. *http://dx.doi.org/10.1080/00268978800100361* **2007**, *63* (4), 527–545. https://doi.org/10.1080/00268978800100361.

(30)   Comer, J.; Phillips, J. C.; Schulten, K.; Chipot, C. Multiple-Replica Strategies for Free-Energy Calculations in NAMD: Multiple-Walker Adaptive Biasing Force and Walker Selection Rules. *J. Chem. Theory Comput.* **2014**, *10* (12), 5276–5285. https://doi.org/10.1021/CT500874P.

(31)   Dehez, F.; Tarek, M.; Chipot*, C. Energetics of Ion Transport in a Peptide Nanotube. *J. Phys. Chem. B* **2007**, *111* (36), 10633–10635. https://doi.org/10.1021/JP075308S.

(32)   Romo, T. D.; Grossfield, A. Unknown Unknowns: The Challenge of Systematic and Statistical Error in Molecular Dynamics Simulations. *Biophys. J.* **2014**, *106* (8), 1553. https://doi.org/10.1016/J.BPJ.2014.03.007.

(33)   Nijmeijer, M. J. P.; Bruin, C.; Bakker, A. F.; van Leeuwen, J. M. J. Wetting and Drying of an Inert Wall by a Fluid in a Molecular-Dynamics Simulation. *Phys. Rev. A* **1990**, *42* (10), 6052. https://doi.org/10.1103/PhysRevA.42.6052.

(34)   Plimpton, S. Fast Parallel Algorithms for Short-Range Molecular Dynamics. *J. Comput. Phys.* **1995**, *117* (1), 1–19. https://doi.org/10.1006/JCPH.1995.1039.

(35)   Case, D.; Cheatham, T.; Darden, T.; Gohlke, H.; Luo, R.; Merz, K.; Onufriev, A.; Simmerling, C.; Wang, B.; Woods, R. The Amber Biomolecular Simulation Programs. *J. Comput. Chem.* **2005**, *26* (16), 1668–1688. https://doi.org/10.1002/JCC.20290.

(36)   Brooks, B.; Brooks, C.; Mackerell, A.; Nilsson, L.; Petrella, R.; Roux, B.; Won, Y.; Archontis, G.; Bartels, C.; Boresch, S. CHARMM: The Biomolecular Simulation Program. *J. Comput. Chem.* **2009**, *30* (10), 1545–1614. https://doi.org/10.1002/JCC.21287.

(37)   Christen, M.; Hünenberger, P.; Bakowies, D.; Baron, R.; Bürgi, R.; Geerke, D.; Heinz, T.; Kastenholz, M.; Kräutler, V.; Oostenbrink, C. The GROMOS Software for Biomolecular Simulation: GROMOS05. *J. Comput. Chem.* **2005**, *26* (16), 1719–1751. https://doi.org/10.1002/JCC.20303.

(38)   Abraham, M. J.; Murtola, T.; Schulz, R.; Páll, S.; Smith, J. C.; Hess, B.; Lindah, E. GROMACS: High Performance Molecular Simulations through Multi-Level Parallelism from Laptops to Supercomputers. *SoftwareX* **2015**, *1–2*, 19–25. https://doi.org/10.1016/J.SOFTX.2015.06.001.

(39)   Chow, E.; Rendleman, C. A.; Bowers, K. J.; Dror, R. O.; Hughes, D. H.; Gullingsrud, J.; Sacerdoti, F. D.; Shaw, D. E. Desmond Performance on a Cluster of Multicore Processors Hardware and Operating Environment Benchmark Systems and Simulation Parameters. **2008**.

(40)   Watts, K. S.; Dalal, P.; Tebben, A. J.; Cheney, D. L.; Shelley, J. C. Macrocycle Conformational Sampling with MacroModel. *J. Chem. Inf. Model.* **2014**, *54* (10), 2680–2696. https://doi.org/10.1021/CI5001696.

(41)   Phillips, J. C.; Braun, R.; Wang, W.; Gumbart, J.; Tajkhorshid, E.; Villa, E.; Chipot, C.; Skeel, R. D.; Kalé, L.; Schulten, K. Scalable Molecular Dynamics with NAMD. *J. Comput. Chem.* **2005**, *26* (16), 1781–1802. https://doi.org/10.1002/JCC.20289.

(42)   Lagardère, L.; Jolly, L.-H.; Lipparini, F.; Aviat, F.; Stamm, B.; Zhifeng, F.; Harger, M.; Torabifard, H.; Cisneros, A.; Schnieders, M. J. Tinker-HP: A Massively Parallel Molecular Dynamics Package for Multiscale Simulations of Large Complex Systems with Advanced Point Dipole Polarizable Force Fields. *Chem. Sci.* **2018**, *9* (4), 956–972. https://doi.org/10.1039/C7SC04531J.

(43) Hanwell, M. D.; Curtis, D. E.; Lonie, D. C.; Vandermeersch, T.; Zurek, E.; Hutchison, G. R. Avogadro: An Advanced Semantic Chemical Editor, Visualization, and Analysis Platform. *J. Cheminform.* **2012**, *4* (8), 17. https://doi.org/10.1186/1758-2946-4-17.

(44) Martínez, L.; Andrade, R.; Birgin, E. G.; Martínez, J. M. PACKMOL: A Package for Building Initial Configurations for Molecular Dynamics Simulations. *J. Comput. Chem.* **2009**, *30* (13), 2157–2164. https://doi.org/10.1002/JCC.21224.

(45) Meunier, M.; Robertson, S. Materials Studio 20th Anniversary. *Mol. Simul.* **2021**, *47* (7), 537–539. https://doi.org/10.1080/08927022.2021.1892093.

(46) Yang, S.; Banavali, N. K.; Roux, B. Mapping the Conformational Transition in Src Activation by Cumulating the Information from Multiple Molecular Dynamics Trajectories. *Proc. Natl. Acad. Sci.* **2009**, *106* (10), 3776–3781. https://doi.org/10.1073/PNAS.0808261106.

(47) Mirjalili, V.; Noyes, K.; Feig, M. Physics-Based Protein Structure Refinement through Multiple Molecular Dynamics Trajectories and Structure Averaging. *Proteins Struct. Funct. Bioinforma.* **2014**, *82* (SUPPL.2), 196–207. https://doi.org/10.1002/PROT.24336.

(48) Cornell, W. D.; Cieplak, P.; Bayly, C. I.; Gould, I. R.; Merz, K. M.; Ferguson, D. M.; Spellmeyer, D. C.; Fox, T.; Caldwell, J. W.; Kollman, P. A. A Second Generation Force Field for the Simulation of Proteins, Nucleic Acids, and Organic Molecules. *J. Am. Chem. Soc.* **2002**, *117* (19), 5179–5197. https://doi.org/10.1021/JA00124A002.

(49) Rappe, A. K.; Casewit, C. J.; Colwell, K. S.; III, W. A. G.; Skiff, W. M. UFF, a Full Periodic Table Force Field for Molecular Mechanics and Molecular Dynamics Simulations. *J. Am. Chem. Soc.* **2002**, *114* (25), 10024–10035. https://doi.org/10.1021/JA00051A040.

(50) van Duin, A. C. T.; Dasgupta, S.; Lorant, F.; Goddard III, W. A. ReaxFF: A Reactive Force Field for Hydrocarbons. **2001**. https://doi.org/10.1021/JP004368U.

(51) Mayo, S. L.; Olafson, B. D.; Goddard, W. A. DREIDING: A Generic Force Field for Molecular Simulations. *J. Phys. Chem.* **2002**, *94* (26), 8897–8909. https://doi.org/10.1021/J100389A010.

(52) Shi, S.; Yan, L.; Yang, Y.; Fisher-Shaulsky, J.; Thacher, T. An Extensible and Systematic Force Field, ESFF, for Molecular Modeling of Organic, Inorganic, and Organometallic Systems. *J. Comput. Chem.* **2003**, *24* (9), 1059–1076. https://doi.org/10.1002/JCC.10171.

(53) Comba, P.; Remenyi, R. Inorganic and Bioinorganic Molecular Mechanics

Modeling—the Problem of the Force Field Parameterization. *Coord. Chem. Rev.* **2003**, *238–239*, 9–20. https://doi.org/10.1016/S0010-8545(02)00286-2.

(54) Daw, M. S.; Foiles, S. M.; Baskes, M. I. The Embedded-Atom Method: A Review of Theory and Applications. *Mater. Sci. Reports* **1993**, *9* (7–8), 251–310. https://doi.org/10.1016/0920-2307(93)90001-U.

(55) Lee, B.-J.; Baskes, M. I. Second Nearest-Neighbor Modified Embedded-Atom-Method Potential. *Phys. Rev. B* **2000**, *62* (13), 8564. https://doi.org/10.1103/PhysRevB.62.8564.

(56) Wei, J.; Zhou, W.; Li, S.; Shen, P.; Ren, S.; Hu, A.; Zhou, W. Modified Embedded Atom Method Potential for Modeling the Thermodynamic Properties of High Thermal Conductivity Beryllium Oxide. *ACS Omega* **2019**, *4* (4), 6339–6346. https://doi.org/10.1021/ACSOMEGA.9B00174.

(57) Stuart, S. J.; Tutein, A. B.; Harrison, J. A. A Reactive Potential for Hydrocarbons with Intermolecular Interactions. *J. Chem. Phys.* **2000**, *112* (14), 6472. https://doi.org/10.1063/1.481208.

(58) Tersoff, J. Modeling Solid-State Chemistry: Interatomic Potentials for Multicomponent Systems. *Phys. Rev. B* **1989**, *39* (8), 5566. https://doi.org/10.1103/PhysRevB.39.5566.

(59) MacKerell Jr., A. D.; Bashford, D.; Bellott, M.; Dunbrack Jr., R. L.; Evanseck, J. D.; Field, M. J.; Fischer, S.; Gao, J.; Guo, H.; Ha, S. All-Atom Empirical Potential for Molecular Modeling and Dynamics Studies of Proteins †. *J. Phys. Chem. B* **1998**, *102* (18), 3586–3616. https://doi.org/10.1021/JP973084F.

(60) Jorgensen, W. L.; Maxwell, D. S.; Tirado-Rives, J. Development and Testing of the OPLS All-Atom Force Field on Conformational Energetics and Properties of Organic Liquids. *J. Am. Chem. Soc.* **1996**, *118* (45), 11225–11236. https://doi.org/10.1021/ja9621760.

(61) Schmid, N.; Eichenberger, A. P.; Choutko, A.; Riniker, S.; Winger, M.; Mark, A. E.; van Gunsteren, W. F. Definition and Testing of the GROMOS Force-Field Versions 54A7 and 54B7. *Eur. Biophys. J. 2011 407* **2011**, *40* (7), 843–856. https://doi.org/10.1007/S00249-011-0700-9.

(62) Lins, R. D.; Hünenberger, P. H. A New GROMOS Force Field for Hexopyranose-Based Carbohydrates. *J. Comput. Chem.* **2005**, *26* (13), 1400–1412. https://doi.org/10.1002/JCC.20275.

(63) Kaminski, G. A.; Friesner*, R. A.; Tirado-Rives, J.; Jorgensen, W. L. Evaluation and Reparametrization of the OPLS-AA Force Field for Proteins via Comparison with Accurate Quantum Chemical Calculations on Peptides. *J. Phys. Chem. B*

2001, *105* (28), 6474–6487. https://doi.org/10.1021/JP003919D.

(64)   Siu, S. W. I.; Pluhackova, K.; Böckmann, R. A. Optimization of the OPLS-AA
Force Field for Long Hydrocarbons. *J. Chem. Theory Comput.* **2012**, *8* (4), 1459–
1470. https://doi.org/10.1021/CT200908R.

(65)   Dickson, C. J.; Rosso, L.; Betz, R. M.; Walker, R. C.; Gould, I. R. GAFFlipid: A
General Amber Force Field for the Accurate Molecular Dynamics Simulation of
Phospholipid. *Soft Matter* **2012**, *8* (37), 9617–9627.
https://doi.org/10.1039/C2SM26007G.

(66)   Seabra, G. de M.; Walker, R. C.; Elstner, M.; Case, D. A.; Roitberg, A. E.
Implementation of the SCC-DFTB Method for Hybrid QM/MM Simulations within
the Amber Molecular Dynamics Package†. *J. Phys. Chem. A* **2007**, *111* (26),
5655–5664. https://doi.org/10.1021/JP070071L.

(67)   Vanommeslaeghe, K.; Hatcher, E.; Acharya, C.; Kundu, S.; Zhong, S.; Shim, J.;
Darian, E.; Guvench, O.; Lopes, P.; Vorobyov, I. CHARMM General Force Field
(CGenFF): A Force Field for Drug-like Molecules Compatible with the CHARMM
All-Atom Additive Biological Force Fields. *J. Comput. Chem.* **2010**, *31* (4), 671.
https://doi.org/10.1002/JCC.21367.

(68)   Naserifar, S.; Brooks, D.; Goddard, W.; Cvicek, V. Polarizable Charge
Equilibration Model for Predicting Accurate Electrostatic Interactions in Molecules
and Solids. *J. Chem. Phys.* **2017**, *146* (12). https://doi.org/10.1063/1.4978891.

(69)   Wang, A.; Ferguson, D.; Wang, J.; Wolf, R. M.; Caldwell, J. W.; Kollman, P. A.;
Case, D. A. Development and Testing of a General Amber Force Field. **2004**.

(70)   Ponder, J. W.; Case, D. A. FORCE FIELDS FOR PROTEIN SIMULATIONS.
2003.

(71)   Tian, C.; Kasavajhala, K.; Belfon, K. A. A.; Raguette, L.; Huang, H.; Migues, A. N.;
Bickel, J.; Wang, Y.; Pincay, J.; Wu, Q. Ff19SB: Amino-Acid-Specific Protein
Backbone Parameters Trained against Quantum Mechanics Energy Surfaces in
Solution. *J. Chem. Theory Comput.* **2020**, *16* (1), 528–552.
https://doi.org/10.1021/ACS.JCTC.9B00591/SUPPL_FILE/CT9B00591_SI_002.ZI
P.

(72)   Cheatham, T. E.; Case, D. A. Twenty-Five Years of Nucleic Acid Simulations.
Biopolymers **2013**, *99* (12), 969–977. https://doi.org/10.1002/BIP.22331.

(73)   Mackerell, A. D.; Banavali, N. K. All-Atom Empirical Force Field for Nucleic Acids:
II. Application to Molecular Dynamics Simulations of DNA and RNA in Solution
MACKERELL AND BANAVALI. *J. Comput. Chem.* **2000**, *21* (2), 105–120.
https://doi.org/10.1002/(SICI)1096-987X(20000130)21:2.

(74)   Feller, S. E.; Gawrisch, K.; MacKerell, A. D. Polyunsaturated Fatty Acids in Lipid
        Bilayers: Intrinsic and Environmental Contributions to Their Unique Physical
        Properties. *J. Am. Chem. Soc.* **2002**, *124* (2), 318–326.
        https://doi.org/10.1021/JA0118340.

(75)   Jorgensen, W. L.; Maxwell, D. S.; Tirado-Rives, J. Development and Testing of
        the OPLS All-Atom Force Field on Conformational Energetics and Properties of
        Organic Liquids. *J. Am. Chem. Soc.* **1996**, *118* (45), 11225–11236.
        https://doi.org/10.1021/JA9621760/SUPPL_FILE/JA11225.PDF.

(76)   Sambasivarao, S. V.; Acevedo, O. Development of OPLS-AA Force Field
        Parameters for 68 Unique Ionic Liquids. *J. Chem. Theory Comput.* **2009**, *5* (4),
        1038–1050.
        https://doi.org/10.1021/CT900009A/SUPPL_FILE/CT900009A_SI_001.PDF.

(77)   Roos, K.; Wu, C.; Damm, W.; Reboul, M.; Stevenson, J. M.; Lu, C.; Dahlgren, M.
        K.; Mondal, S.; Chen, W.; Wang, L. OPLS3e: Extending Force Field Coverage for
        Drug-Like Small Molecules. *J. Chem. Theory Comput.* **2019**, *15* (3), 1863–1874.
        https://doi.org/10.1021/ACS.JCTC.8B01026/SUPPL_FILE/CT8B01026_SI_002.ZI
        P.

(78)   Nielson, K. D.; Van Duin, A. C. T.; Oxgaard, J.; Deng, W. Q.; Goddard, W. A.
        Development of the ReaxFF Reactive Force Field for Describing Transition Metal
        Catalyzed Reactions, with Application to the Initial Stages of the Catalytic
        Formation of Carbon Nanotubes. *J. Phys. Chem. A* **2005**, *109* (3), 493–499.
        https://doi.org/10.1021/JP046244D/SUPPL_FILE/JP046244DSI20041110_07243
        6.TXT.

(79)   Senftle, T. P.; Hong, S.; Islam, M. M.; Kylasa, S. B.; Zheng, Y.; Shin, Y. K.;
        Junkermeier, C.; Engel-Herbert, R.; Janik, M. J.; Aktulga, H. M. The ReaxFF
        Reactive Force-Field: Development, Applications and Future Directions. *npj
        Comput. Mater. 2016 21* **2016**, *2* (1), 1–14.
        https://doi.org/10.1038/npjcompumats.2015.11

(80)   Lopes, P. E. M.; Huang, J.; Shim, J.; Luo, Y.; Li, H.; Roux, B.; Mackerell, A. D.
        Polarizable Force Field for Peptides and Proteins Based on the Classical Drude
        Oscillator. *J. Chem. Theory Comput.* **2013**, *9* (12), 5430–5449.
        https://doi.org/10.1021/CT400781B/SUPPL_FILE/CT400781B_SI_001.PDF.

(81)   Jiang, W.; Hardy, D. J.; Phillips, J. C.; MacKerell, A. D.; Schulten, K.; Roux, B.
        High-Performance Scalable Molecular Dynamics Simulations of a Polarizable
        Force Field Based on Classical Drude Oscillators in NAMD. *J. Phys. Chem. Lett.*
        2011, *2* (2), 87–92.
        https://doi.org/10.1021/JZ101461D/SUPPL_FILE/JZ101461D_SI_001.PDF.

(82) Lemkul, J. A.; Huang, J.; Roux, B.; Mackerell, A. D. An Empirical Polarizable Force Field Based on the Classical Drude Oscillator Model: Development History and Recent Applications. *Chem. Rev.* **2016**, *116* (9), 4983–5013. https://doi.org/10.1021/ACS.CHEMREV.5B00505.

(83) Christen, M.; Hünenberger, P. H.; Bakowies, D.; Baron, R.; Bürgi, R.; Geerke, D. P.; Heinz, T. N.; Kastenholz, M. A.; Kräutler, V.; Oostenbrink, C. The GROMOS Software for Biomolecular Simulation: GROMOS05. *J. Comput. Chem.* **2005**, *26* (16), 1719–1751. https://doi.org/10.1002/JCC.20303.

(84) Kunz, A. P. E.; Allison, J. R.; Geerke, D. P.; Horta, B. A. C.; Hünenberger, P. H.; Riniker, S.; Schmid, N.; Van Gunsteren, W. F. New Functionalities in the GROMOS Biomolecular Simulation Software. *J. Comput. Chem.* **2012**, *33* (3), 340–353. https://doi.org/10.1002/JCC.21954.

(85) Riniker, S.; Christ, C. D.; Hansen, H. S.; Hünenberger, P. H.; Oostenbrink, C.; Steiner, D.; Van Gunsteren, W. F. Calculation of Relative Free Energies for Ligand-Protein Binding, Solvation, and Conformational Transitions Using the GROMOS Software. *J. Phys. Chem. B* **2011**, *115* (46), 13570–13577. https://doi.org/10.1021/JP204303A.

(86) Leontyev, I. V.; Stuchebrukhov, A. A. Polarizable Mean-Field Model of Water for Biological Simulations with Amber and Charmm Force Fields. *J. Chem. Theory Comput.* **2012**, *8* (9), 3207. https://doi.org/10.1021/CT300011H.

(87) Ren, P.; Ponder, J. W. Consistent Treatment of Inter- and Intramolecular Polarization in Molecular Mechanics Calculations. *J. Comput. Chem.* **2002**, *23* (16), 1497–1506. https://doi.org/10.1002/JCC.10127.

(88) Ponder, J. W.; Wu, C.; Ren, P.; Pande, V. S.; Chodera, J. D.; Schnieders, M. J.; Haque, I.; Mobley, D. L.; Lambrecht, D. S.; Distasio, R. A. Current Status of the AMOEBA Polarizable Force Field. *J. Phys. Chem. B* **2010**, *114* (8), 2549–2564. https://doi.org/10.1021/JP910674D/SUPPL_FILE/JP910674D_SI_002.PDF.

(89) Zhang, C.; Lu, C.; Jing, Z.; Wu, C.; Piquemal, J. P.; Ponder, J. W.; Ren, P. AMOEBA Polarizable Atomic Multipole Force Field for Nucleic Acids. *J. Chem. Theory Comput.* **2018**, *14* (4), 2084–2108. https://doi.org/10.1021/ACS.JCTC.7B01169/SUPPL_FILE/CT7B01169_SI_002.PDF.

(90) Rathnayake, P. V. G. M.; Bernardi, S.; Widmer-Cooper, A. Evaluation of the AMOEBA Force Field for Simulating Metal Halide Perovskites in the Solid State and in Solution. *J. Chem. Phys.* **2020**, *152* (2), 024117. https://doi.org/10.1063/1.5131790.

(91) Narayanan, B.; Sasikumar, K.; Mei, Z. G.; Kinaci, A.; Sen, F. G.; Davis, M. J.;

Gray, S. K.; Chan, M. K. Y.; Sankaranarayanan, S. K. R. S. Development of a Modified Embedded Atom Force Field for Zirconium Nitride Using Multi-Objective Evolutionary Optimization. *J. Phys. Chem. C* **2016**, *120* (31), 17475–17483. https://doi.org/10.1021/ACS.JPCC.6B05296/SUPPL_FILE/JP6B05296_SI_001.PDF.

(92)   Boyd, P. G.; Moosavi, S. M.; Witman, M.; Smit, B. Force-Field Prediction of Materials Properties in Metal-Organic Frameworks. *J. Phys. Chem. Lett.* **2017**, *8* (2), 357–363. https://doi.org/10.1021/ACS.JPCLETT.6B02532/SUPPL_FILE/JZ6B02532_SI_002.ZIP.

(93)   Sasaki, K.; Yamashita, T. Modification and Validation of the DREIDING Force Field for Molecular Liquid Simulations (DREIDING-UT). *J. Chem. Inf. Model.* **2021**, *61* (3), 1172–1179. https://doi.org/10.1021/ACS.JCIM.0C01169.

(94)   Marrink, S. J.; Risselada, H. J.; Yefimov, S.; Tieleman, D. P.; De Vries, A. H. The MARTINI Force Field: Coarse Grained Model for Biomolecular Simulations. *J. Phys. Chem. B* **2007**, *111* (27), 7812–7824. https://doi.org/10.1021/JP071097F.

(95)   Yoo, A. B.; Jette, M. A.; Grondona, M. SLURM: Simple Linux Utility for Resource Management. *Lect. Notes Comput. Sci. (including Subser. Lect. Notes Artif. Intell. Lect. Notes Bioinformatics)* **2003**, *2862*, 44–60. https://doi.org/10.1007/10968987_3.

(96)   Jung, J.; Nishima, W.; Daniels, M.; Bascom, G.; Kobayashi, C.; Adedoyin, A.; Wall, M.; Lappala, A.; Phillips, D.; Fischer, W. Scaling Molecular Dynamics beyond 100,000 Processor Cores for Large-Scale Biophysical Simulations. *J. Comput. Chem.* **2019**, *40* (21), 1919–1930. https://doi.org/10.1002/JCC.25840.

(97)   Klein, M. L.; Shinoda, W. Large-Scale Molecular Dynamics Simulations of Self-Assembling Systems. *Science (80-.).* **2008**, *321* (5890), 798–800. https://doi.org/10.1126/SCIENCE.1157834.

(98)   Thompson, A. P.; Aktulga, H. M.; Berger, R.; Bolintineanu, D. S.; Brown, W. M.; Crozier, P. S.; in 't Veld, P. J.; Kohlmeyer, A.; Moore, S. G.; Nguyen, T. D. LAMMPS - a Flexible Simulation Tool for Particle-Based Materials Modeling at the Atomic, Meso, and Continuum Scales. *Comput. Phys. Commun.* **2022**, *271*, 108171. https://doi.org/10.1016/J.CPC.2021.108171.

(99)   Phillips, J. C.; Hardy, D. J.; Maia, J. D. C.; Stone, J. E.; Ribeiro, J. V.; Bernardi, R. C.; Buch, R.; Fiorin, G.; Hénin, J.; Jiang, W. Scalable Molecular Dynamics on CPU and GPU Architectures with   NAMD. *J. Chem. Phys.* **2020**, *153* (4), 044130. https://doi.org/10.1063/5.0014475.

(100) Berendsen, H. J. C.; van der Spoel, D.; van Drunen, R. GROMACS: A Message-

Passing Parallel Molecular Dynamics Implementation. *Comput. Phys. Commun.* **1995**, *91* (1–3), 43–56. https://doi.org/10.1016/0010-4655(95)00042-E.

(101) Brooks, B. R.; Brooks, C. L.; Mackerell, A. D.; Nilsson, L.; Petrella, R. J.; Roux, B.; Won, Y.; Archontis, G.; Bartels, C.; Boresch, S. CHARMM: The Biomolecular Simulation Program. *J. Comput. Chem.* **2009**, *30* (10), 1545. https://doi.org/10.1002/JCC.21287.

(102) Salomon-Ferrer, R.; Case, D. A.; Walker, R. C. An Overview of the Amber Biomolecular Simulation Package. *Wiley Interdiscip. Rev. Comput. Mol. Sci.* **2013**, *3* (2), 198–210. https://doi.org/10.1002/WCMS.1121.

(103) Case, D. A.; Cheatham, T. E.; Darden, T.; Gohlke, H.; Luo, R.; Merz, K. M.; Onufriev, A.; Simmerling, C.; Wang, B.; Woods, R. J. The Amber Biomolecular Simulation Programs. *J. Comput. Chem.* **2005**, *26* (16), 1668–1688. https://doi.org/10.1002/JCC.20290.

(104) Rackers, J. A.; Wang, Z.; Lu, C.; Laury, M. L.; Lagardère, L.; Schnieders, M. J.; Piquemal, J. P.; Ren, P.; Ponder, J. W. Tinker 8: Software Tools for Molecular Design. *J. Chem. Theory Comput.* **2018**, *14* (10), 5273–5289. https://doi.org/10.1021/ACS.JCTC.8B00529.

(105) Toukan, K.; Rahman, A. Molecular-Dynamics Study of Atomic Motions in Water. *Phys. Rev. B* **1985**, *31* (5), 2643. https://doi.org/10.1103/PhysRevB.31.2643.

(106) Clark Still, W.; Tempczyk, A.; Hawley, R. C.; Hendrickson, T. Semianalytical Treatment of Solvation for Molecular Mechanics and Dynamics. *J. Am. Chem. Soc.* **1990**, *112* (16), 6127–6129. https://doi.org/10.1021/JA00172A038/SUPPL_FILE/JA00172A038_SI_001.PDF.

(107) Jorgensen, W. L.; Tirado-Rives, J. Molecular Modeling of Organic and Biomolecular Systems Using BOSS and MCPRO. *J. Comput. Chem.* **2005**, *26* (16), 1689–1700. https://doi.org/10.1002/JCC.20297.

(108) Kühne, T. D.; Iannuzzi, M.; Del Ben, M.; Rybkin, V. V.; Seewald, P.; Stein, F.; Laino, T.; Khaliullin, R. Z.; Schütt, O.; Schiffmann, F. CP2K: An Electronic Structure and Molecular Dynamics Software Package - Quickstep: Efficient and Accurate Electronic Structure Calculations. *J. Chem. Phys.* **2020**, *152* (19), 194103. https://doi.org/10.1063/5.0007045.

(109) Marelius, J.; Kolmodin, K.; Feierberg, I.; Åqvist, J. Q: A Molecular Dynamics Program for Free Energy Calculations and Empirical Valence Bond Simulations in Biomolecular Systems. *J. Mol. Graph. Model.* **1998**, *16* (4–6), 213–225. https://doi.org/10.1016/S1093-3263(98)80006-5.

(110) Bowers, K. J.; Chow, E.; Xu, H.; Dror, R. O.; Eastwood, M. P.; Gregersen, B. A.;

Klepeis, J. L.; Kolossvary, I.; Moraes, M. A.; Sacerdoti, F. D. Scalable Algorithms for Molecular Dynamics Simulations on Commodity Clusters. *Proc. 2006 ACM/IEEE Conf. Supercomput. SC'06* **2006**. https://doi.org/10.1145/1188455.1188544.

(111) BIOVIA. Materials Studio. *San Diego Dassault Syst.*

(112) Anderson, J. A.; Eric Irrgang, M.; Glotzer, S. C. Scalable Metropolis Monte Carlo for Simulation of Hard Shapes. *Comput. Phys. Commun.* **2016**, *204*, 21–30. https://doi.org/10.1016/J.CPC.2016.02.024.

(113) Anderson, J. A.; Lorenz, C. D.; Travesset, A. General Purpose Molecular Dynamics Simulations Fully Implemented on Graphics Processing Units. *J. Comput. Phys.* **2008**, *227* (10), 5342–5359. https://doi.org/10.1016/J.JCP.2008.01.047.

(114) Franz, D. M.; Belof, J. L.; McLaughlin, K.; Cioce, C. R.; Tudor, B.; Hogan, A.; Laratelli, L.; Mulcair, M.; Mostrom, M.; Navas, A. MPMC and MCMD: Free High-Performance Simulation Software for Atomistic Systems. *Adv. Theory Simulations* **2019**, *2* (11), 1900113. https://doi.org/10.1002/ADTS.201900113.

(115) Laio, A.; Parrinello, M. Escaping Free-Energy Minima. *Proc. Natl. Acad. Sci. U. S. A.* **2002**, *99* (20), 12562. https://doi.org/10.1073/PNAS.202427399.

(116) Barducci, A.; Bussi, G.; Parrinello, M. Well-Tempered Metadynamics: A Smoothly-Converging and Tunable Free-Energy Method. **2008**.

(117) Torrie, G. M.; Valleau, J. P. Nonphysical Sampling Distributions in Monte Carlo Free-Energy Estimation: Umbrella Sampling. *J. Comput. Phys.* **1977**, *23* (2), 187–199. https://doi.org/10.1016/0021-9991(77)90121-8.

(118) Shen, J.; Fujita, K.; Matsumoto, T.; Hongo, C.; Misaki, M.; Ishida, K.; Mori, A.; Nishino, T. Mechanical, Thermal, and Electrical Properties of Flexible Polythiophene with Disiloxane Side Chains. *Macromol. Chem. Phys.* **2017**, *218* (19), 1700197. https://doi.org/10.1002/macp.201700197.

(119) Zwanzig, R. W. High-Temperature Equation of State by a Perturbation Method. I. Nonpolar Gases. *J. Chem. Phys.* **2004**, *22* (8), 1420. https://doi.org/10.1063/1.1740409.

(120) Bolhuis, P. G.; Chandler, D.; Dellago, C.; Geissler, P. L. TRANSITION PATH SAMPLING: Throwing Ropes Over Rough Mountain Passes, in the Dark. *Annu. Rev. Phys. Chem* **2003**, *53*, 291–318. https://doi.org/10.1146/ANNUREV.PHYSCHEM.53.082301.113146.

(121) Voter, A. F. Hyperdynamics: Accelerated Molecular Dynamics of Infrequent

Events. **1997**.

(122) Qi, R.; Wei, G.; Ma, B.; Nussinov, R. Replica Exchange Molecular Dynamics: A Practical Application Protocol with Solutions to Common Problems and a Peptide Aggregation and Self-Assembly Example. *Methods Mol. Biol.* **2018**, *1777*, 101. https://doi.org/10.1007/978-1-4939-7811-3_5.

(123) Minary, P.; Tuckerman, M. E.; Martyna, G. J. Long Time Molecular Dynamics for Enhanced Conformational Sampling in Biomolecular Systems. *Phys. Rev. Lett.* **2004**, *93* (15), 150201. https://doi.org/10.1103/PhysRevLett.93.150201.

(124) Hollingsworth, S. A.; Dror, R. O. Molecular Dynamics Simulation for All. *Neuron* **2018**, *99* (6), 1129. https://doi.org/10.1016/J.NEURON.2018.08.011.

(125) Hospital, A.; Goñi, J. R.; Orozco, M.; Gelpí, J. L. Molecular Dynamics Simulations: Advances and Applications. *Adv. Appl. Bioinforma. Chem.* **2015**, *8* (1), 37–47. https://doi.org/10.2147/AABC.S70333.

(126) Introduction to Monte Carlo Methods in Chemistry https://people.chem.ucsb.edu/kahn/kalju/MonteCarlo_4.html (accessed Jan 13, 2022).

(127) Cuppen, H. M.; Karssemeijer, L. J.; Lamberts, T. The Kinetic Monte Carlo Method as a Way To Solve the Master Equation for Interstellar Grain Chemistry. *Chem. Rev.* **2013**, *113* (12), 8840–8871. https://doi.org/10.1021/CR400234A.

(128) Lim, K. C.; Kapitulnik, A.; Zacher, R.; Casalnuovo, S.; Wudl, F.; Heeger, A. J. Polydiacetylene Macromolecules in Solution: Rods, Coils and Gels. *Polydiacetylenes* **1985**, 257–290. https://doi.org/10.1007/978-94-017-2713-6_20.

(129) Beaujuge, P. M.; Amb, C. M.; Reynolds, J. R. Spectral Engineering in π-Conjugated Polymers with Intramolecular Donor−Acceptor Interactions. *Acc. Chem. Res.* **2010**, *43* (11), 1396–1407. https://doi.org/10.1021/AR100043U.

(130) Fratini, S.; Nikolka, M.; Salleo, A.; Schweicher, G.; Sirringhaus, H. Charge Transport in High-Mobility Conjugated Polymers and Molecular Semiconductors. *Nat. Mater. 2020 195* **2020**, *19* (5), 491–502. https://doi.org/10.1038/s41563-020-0647-2.

(131) Yu, Z. Di; Lu, Y.; Wang, J. Y.; Pei, J. Conformation Control of Conjugated Polymers. *Chem. – A Eur. J.* **2020**, *26* (69), 16194–16205. https://doi.org/10.1002/CHEM.202000220.

(132) Tamai, Y. Delocalization Boosts Charge Separation in Organic Solar Cells. *Polym. J. 2020 527* **2020**, *52* (7), 691–700. https://doi.org/10.1038/s41428-020-0339-4.

(133) Noriega, R.; Rivnay, J.; Vandewal, K.; Koch, F. P. V.; Stingelin, N.; Smith, P.; Toney, M. F.; Salleo, A. A General Relationship between Disorder, Aggregation and Charge Transport in Conjugated Polymers. *Nat. Mater.* **2013**, *12* (11), 1038–1044. https://doi.org/10.1038/NMAT3722.

(134) Lin, J. B.; Jin, Y.; Lopez, S. A.; Druckerman, N.; Wheeler, S. E.; Houk, K. N. Torsional Barriers to Rotation and Planarization in Heterocyclic Oligomers of Value in Organic Electronics. *J. Chem. Theory Comput.* **2017**, *13* (11), 5624–5638. https://doi.org/10.1021/ACS.JCTC.7B00709/SUPPL_FILE/CT7B00709_SI_001.PDF.

(135) Hwang, H.; Kim, Y.; Kang, M.; Lee, M. H.; Heo, Y. J.; Kim, D. Y. A Conjugated Polymer with High Planarity and Extended π-Electron Delocalization: Via a Quinoid Structure Prepared by Short Synthetic Steps. *Polym. Chem.* **2017**, *8* (2), 361–365. https://doi.org/10.1039/c6py01729k.

(136) Cao, Z.; Leng, M.; Cao, Y.; Gu, X.; Fang, L. How Rigid Are Conjugated Non-Ladder and Ladder Polymers? *J. Polym. Sci.* **2022**, *60* (3), 298–310. https://doi.org/10.1002/POL.20210550.

(137) Tsumura, A.; Koezuka, H.; Ando, T. Macromolecular Electronic Device: Field-effect Transistor with a Polythiophene Thin Film. *Appl. Phys. Lett.* **1998**, *49* (18), 1210. https://doi.org/10.1063/1.97417.

(138) Chamberlain, G. A. Organic Solar Cells: A Review. *Sol. Cells* **1983**, *8* (1), 47–83. https://doi.org/10.1016/0379-6787(83)90039-X.

(139) Crone, B.; Dodabalapur, A.; Gelperin, A.; Torsi, L.; Katz, H. E.; Lovinger, A. J.; Bao, B. Electronic Sensing of Vapors with Organic Transistors. *Appl. Phys. Lett.* **2001**, *78* (15), 2229. https://doi.org/10.1063/1.1360785.

(140) Havinga, E. E.; ten Hoeve, W.; Wynberg, H. Alternate Donor-Acceptor Small-Band-Gap Semiconducting Polymers; Polysquaraines and Polycroconaines. *Synth. Met.* **1993**, *55* (1), 299–306. https://doi.org/10.1016/0379-6779(93)90949-W.

(141) Beaujuge, P. M.; Fréchet, J. M. J. Molecular Design and Ordering Effects in π-Functional Materials for Transistor and Solar Cell Applications. *J. Am. Chem. Soc.* **2011**, *133* (50), 20009–20029. https://doi.org/10.1021/JA2073643/SUPPL_FILE/JA2073643_SI_001.PDF.

(142) Zhang, X.; Bronstein, H.; Kronemeijer, A. J.; Smith, J.; Kim, Y.; Kline, R. J.; Richter, L. J.; Anthopoulos, T. D.; Sirringhaus, H.; Song, K. Molecular Origin of High Field-Effect Mobility in an Indacenodithiophene–Benzothiadiazole

Copolymer. *Nat. Commun. 2013 41* **2013**, *4* (1), 1–9.
https://doi.org/10.1038/ncomms3238.

(143) Northrup, J. E. Mobility Enhancement in Polymer Organic Semiconductors Arising from Increased Interconnectivity at the Level of Polymer Segments. *Appl. Phys. Lett.* **2015**, *106* (2), 023303. https://doi.org/10.1063/1.4906061.

(144) Marcon, V.; Raos, G. Free Energies of Molecular Crystal Surfaces by Computer Simulation: Application to Tetrathiophene. *J. Am. Chem. Soc.* **2006**, *128*, 1408–1409. https://doi.org/10.1021/ja056548t.

(145) Jackson, N. E.; Kohlstedt, K. L.; Savoie, B. M.; Olvera de la Cruz, M.; Schatz, G. C.; Chen, L. X.; Ratner, M. A. Conformational Order in Aggregates of Conjugated Polymers. *J. Am. Chem. Soc.* **2015**, *137* (19), 6254–6262. https://doi.org/10.1021/jacs.5b00493.

(146) Raos, G.; Famulari, A.; Marcon, V. Computational Reinvestigation of the Bithiophene Torsion Potential. *Chem. Phys. Lett.* **2003**, *379* (3–4), 364–372. https://doi.org/10.1016/J.CPLETT.2003.08.060.

(147) Jackson, N. E.; Savoie, B. M.; Kohlstedt, K. L.; Olvera de la Cruz, M.; Schatz, G. C.; Chen, L. X.; Ratner, M. A. Controlling Conformations of Conjugated Polymers and Small Molecules: The Role of Nonbonding Interactions. *J. Am. Chem. Soc.* **2013**, *135* (28), 10475–10483. https://doi.org/10.1021/ja403667s.

(148) Dubay, K. H.; Hall, M. L.; Hughes, T. F.; Wu, C.; Reichman, D. R.; Friesner, R. A. Accurate Force Field Development for Modeling Conjugated Polymers. *J. Chem. Theory Comput.* **2012**, *8*, 4556–4569. https://doi.org/10.1021/ct300175w.

(149) Fauvell, T. J.; Zheng, T.; Jackson, N. E.; Ratner, M. A.; Yu, L.; Chen, L. X. Photophysical and Morphological Implications of Single-Strand Conjugated Polymer Folding in Solution. *Chem. Mater.* **2016**, *28* (8), 2814–2822. https://doi.org/10.1021/acs.chemmater.6b00734.

(150) Root, S. E.; Jackson, N. E.; Savagatrup, S.; Arya, G.; Lipomi, D. J. Modelling the Morphology and Thermomechanical Behaviour of Low-Bandgap Conjugated Polymers and Bulk Heterojunction Films. *Energy Environ. Sci. Energy Environ. Sci* **2017**, *558* (10), 558–569. https://doi.org/10.1039/c6ee03456j.

(151) Marcon, V.; Raos, G. Molecular Modeling of Crystalline Oligothiophenes: Testing and Development of Improved Force Fields. *J. Phys. Chem. B* **2004**, *108* (46), 18053–18064.
https://doi.org/10.1021/JP047128D/SUPPL_FILE/JP047128DSI20040903_10401 1.TXT.

(152) Xu, Y.; Sun, H.; Li, W.; Lin, Y.-F.; Balestra, F.; Ghibaudo, G.; Noh, Y.-Y.; Xu, Y.;

Sun, B.; Noh, Y.-Y. Exploring the Charge Transport in Conjugated Polymers. *Adv. Mater.* **2017**, *29* (41), 1702729. https://doi.org/10.1002/ADMA.201702729.

(153) Roth, B.; Savagatrup, S.; De Los Santos, N. V.; Hagemann, O.; Carlé, J. E.; Helgesen, M.; Livi, F.; Bundgaard, E.; Søndergaard, R. R.; Krebs, F. C. Mechanical Properties of a Library of Low-Band-Gap Polymers. *Chem. Mater.* **2016**, *28* (7), 2363–2373. https://doi.org/10.1021/acs.chemmater.6b00525.

(154) Galuska, L. A.; McNutt, W. W.; Qian, Z.; Zhang, S.; Weller, D. W.; Dhakal, S.; King, E. R.; Morgan, S. E.; Azoulay, J. D.; Mei, J. Impact of Backbone Rigidity on the Thermomechanical Properties of Semiconducting Polymers with Conjugation Break Spacers. *Macromolecules* **2020**, *53* (14), 6032–6042. https://doi.org/10.1021/ACS.MACROMOL.0C00889/SUPPL_FILE/MA0C00889_SI_001.PDF.

(155) Ding, Z.; Liu, D.; Zhao, K.; Han, Y. Optimizing Morphology to Trade Off Charge Transport and Mechanical Properties of Stretchable Conjugated Polymer Films. *Macromolecules* **2021**, *54* (9), 3907–3926. https://doi.org/10.1021/ACS.MACROMOL.1C00268.

(156) Kleinschmidt, A. T.; Root, S. E.; Lipomi, D. J. Poly(3-Hexylthiophene) (P3HT): Fruit Fly or Outlier in Organic Solar Cell Research? https://doi.org/10.1039/c6ta08317j.

(157) Kim, M.; Un Ryu, S.; Ah Park, S.; Choi, K.; Kim, T.; Chung, D.; Park, T.; Kim, M.; Ryu, S. U.; Park, S. A. Donor–Acceptor-Conjugated Polymer for High-Performance Organic Field-Effect Transistors: A Progress Report. *Adv. Funct. Mater.* **2020**, *30* (20), 1904545. https://doi.org/10.1002/ADFM.201904545.

(158) Bao, W. W.; Li, R.; Dai, Z. C.; Tang, J.; Shi, X.; Geng, J. T.; Deng, Z. F.; Hua, J. Diketopyrrolopyrrole (DPP)-Based Materials and Its Applications: A Review. *Front. Chem.* **2020**, *8*, 679. https://doi.org/10.3389/FCHEM.2020.00679/BIBTEX.

(159) Zhou, N.; Facchetti, A. Naphthalenediimide (NDI) Polymers for All-Polymer Photovoltaics. *Mater. Today* **2018**, *21* (4), 377–390. https://doi.org/10.1016/J.MATTOD.2018.02.003.

(160) Liang, C.; Wang, H. Indacenodithiophene-Based D-A Conjugated Polymers for Application in Polymer Solar Cells. *Org. Electron.* **2017**, *50*, 443–457. https://doi.org/10.1016/J.ORGEL.2017.06.059.

(161) Gao, C.; Wang, L.; Li, X.; Wang, H. Rational Design on D–A Conjugated P(BDT–DTBT) Polymers for Polymer Solar Cells. *Polym. Chem.* **2014**, *5* (18), 5200–5210. https://doi.org/10.1039/C4PY00389F.

(162) Cheng, P.; Li, G.; Zhan, X.; Yang, Y. Next-Generation Organic Photovoltaics

Based on Non-Fullerene Acceptors. *Nat. Photonics 2018 123* **2018**, *12* (3), 131–142. https://doi.org/10.1038/s41566-018-0104-9.

(163) Wolf, C. M.; Guio, L.; Scheiwiller, S.; Pakhnyuk, V.; Luscombe, C.; Pozzo, L. D. Strategies for the Development of Conjugated Polymer Molecular Dynamics Force Fields Validated with Neutron and X-Ray Scattering. *ACS Polym. Au* **2021**, *1* (3), 134–152. https://doi.org/10.1021/ACSPOLYMERSAU.1C00027.

(164) Grimme, S. Accurate Description of van Der Waals Complexes by Density Functional Theory Including Empirical Corrections. *J. Comput. Chem.* **2004**, *25* (12), 1463–1473. https://doi.org/10.1002/JCC.20078.

(165) Klimeš, J.; Michaelides, A. Perspective: Advances and Challenges in Treating van Der Waals Dispersion Forces in Density Functional Theory. *J. Chem. Phys.* **2012**, *137* (12), 120901. https://doi.org/10.1063/1.4754130.

(166) Jackson, N. E.; Kohlstedt, K. L.; Savoie, B. M.; Olvera de la Cruz, M.; Schatz, G. C.; Chen, L. X.; Ratner, M. A. Conformational Order in Aggregates of Conjugated Polymers. *J. Am. Chem. Soc.* **2015**, *137*, 6254–6262. https://doi.org/10.1021/jacs.5b00493.

(167) Hoover, W. G. Canonical Dynamics: Equilibrium Phase-Space Distributions. *Phys. Rev. A* **1985**, *31* (3), 1695. https://doi.org/10.1103/PhysRevA.31.1695.

(168) Gedefaw, D.; Tessarolo, M.; Zhuang, W.; Kroon, R.; Wang, E.; Bolognesi, M.; Seri, M.; Muccini, M.; Andersson, M. R. Conjugated Polymers Based on Benzodithiophene and Fluorinated Quinoxaline for Bulk Heterojunction Solar Cells: Thiophene versus Thieno[3,2- b]Thiophene as π-Conjugated Spacers. *Polym. Chem.* **2014**, *5* (6), 2083–2093. https://doi.org/10.1039/C3PY01519J.

(169) Kofranek, M.; Kovář, T.; Lischka, H.; Karpfen, A. Ab Initio Studies on Heterocyclic Conjugated Polymers: Structure and Vibrational Spectra of Thiophene, Oligothiophenes and Polythiophene. *J. Mol. Struct. THEOCHEM* **1992**, *259* (C), 181–198. https://doi.org/10.1016/0166-1280(92)87013-P.

(170) Grozema, F. C.; Van Duijnen, P. T.; Berlin, Y. A.; Ratner, M. A.; Siebbeles, L. D. A. Intramolecular Charge Transport along Isolated Chains of Conjugated Polymers: Effect of Torsional Disorder and Polymerization Defects. *J. Phys. Chem. B* **2002**, *106* (32), 7791–7795. https://doi.org/10.1021/JP021114V.

(171) Ning, L.; Han, G.; Yi, Y. Intra-Chain and Inter-Chain Synergistic Effect Gives Rise to High Electron Mobilities for Naphthalenediimide Based Copolymers. *J. Mater. Chem. C* **2020**, *8* (46), 16527–16532. https://doi.org/10.1039/D0TC03715J.

(172) Guo, X.; Kim, F. S.; Seger, M. J.; Jenekhe, S. A.; Watson, M. D. Naphthalene Diimide-Based Polymer Semiconductors: Synthesis, Structure-Property

Correlations, and n-Channel and Ambipolar Field-Effect Transistors. *Chem. Mater.* **2012**, *24* (8), 1434–1442. https://doi.org/10.1021/CM2034273/SUPPL_FILE/CM2034273_SI_001.PDF.

(173) Brédas, J. L.; Street, G. B.; Thémans, B.; André, J. M. Organic Polymers Based on Aromatic Rings (Polyparaphenylene, Polypyrrole, Polythiophene): Evolution of the Electronic Properties as a Function of the Torsion Angle between Adjacent Rings. *J. Chem. Phys.* **1998**, *83* (3), 1323. https://doi.org/10.1063/1.449450.

(174) Gao, Y.; Grey, J. K. Resonance Chemical Imaging of Polythiophene/Fullerene Photovoltaic Thin Films: Mapping Morphology-Dependent Aggregated and Unaggregated C=C Species. *J. Am. Chem. Soc.* **2009**, *131* (28), 9654–9662. https://doi.org/10.1021/JA900636Z/SUPPL_FILE/JA900636Z_SI_001.PDF.

(175) Michaels, W.; Zhao, Y.; Qin, J. Atomistic Modeling of PEDOT:PSS Complexes II: Force Field Parameterization. *Macromolecules* **2021**, *54* (12), 5354–5365. https://doi.org/10.1021/ACS.MACROMOL.1C00860/SUPPL_FILE/MA1C00860_SI_001.ZIP.

(176) Savagatrup, S.; Printz, A. D.; Wu, H.; Rajan, K. M.; Sawyer, E. J.; Zaretski, A. V; Bettinger, C. J.; Lipomi, D. J. Viability of Stretchable Poly(3-Heptylthiophene) (P3HpT) for Organic Solar Cells and Field-Effect Transistors. *Synth. Met.* **2015**, *203*, 208–214. https://doi.org/10.1016/j.synthmet.2015.02.031.

(177) Ashizawa, M.; Zheng, Y.; Tran, H.; Bao, Z. Intrinsically Stretchable Conjugated Polymer Semiconductors in Field Effect Transistors. *Prog. Polym. Sci.* **2020**, *100*, 101181. https://doi.org/10.1016/J.PROGPOLYMSCI.2019.101181.

(178) Hernandez, V.; Da Vinci, P. L.; Castiglioni, I. C.; Zoppo, M. Del; Zerbi, G. *Confinement Potential and N-Electron Delocalization in Polyconjngated Organic Materials*; Vol. 50.

(179) Lupton, J. M. Chromophores in Conjugated Polymers—All Straight? *ChemPhysChem* **2012**, *13* (4), 901–907. https://doi.org/10.1002/CPHC.201100770.

(180) Galuska, L. A.; McNutt, W. W.; Qian, Z.; Zhang, S.; Weller, D. W.; Dhakal, S.; King, E. R.; Morgan, S. E.; Azoulay, J. D.; Mei, J. Impact of Backbone Rigidity on the Thermomechanical Properties of Semiconducting Polymers with Conjugation Break Spacers. *Macromolecules* **2020**, *53* (14), 6032–6042. https://doi.org/10.1021/acs.macromol.0c00889.

(181) Hu, Z.; Liu, J.; Simón-Bower, L.; Zhai, L.; Gesquiere, A. J. Influence of Backbone Rigidness on Single Chain Conformation of Thiophene-Based Conjugated Polymers. *J. Phys. Chem. B* **2013**, *117* (16), 4461–4467. https://doi.org/10.1021/jp308497k.

(182) Jackson, N. E.; Kohlstedt, K. L.; Savoie, B. M.; Olvera de la Cruz, M.; Schatz, G. C.; Chen, L. X.; Ratner, M. A. Conformational Order in Aggregates of Conjugated Polymers. *J. Am. Chem. Soc 137*, 6254–6262.

(183) Oh, J. T.; Ha, Y. H.; Kwon, S. K.; Song, S.; Kim, J. Y.; Kim, Y. H.; Choi, H. Twisted Linker Effect on Naphthalene Diimide-Based Dimer Electron Acceptors for Non-Fullerene Organic Solar Cells. *Macromol. Rapid Commun.* **2018**, *39* (14). https://doi.org/10.1002/MARC.201800108.

(184) Huang, Q.; Chen, J.; Yan, S.; Shao, X.; Dong, Y.; Liu, J.; Li, W.; Zhang, C. New Donor-Acceptor-Donor Conjugated Polymer with Twisted Donor-Acceptor Configuration for High-Capacitance Electrochromic Supercapacitor Application. *ACS Sustain. Chem. Eng.* **2021**, *9* (41), 13807–13817. https://doi.org/10.1021/ACSSUSCHEMENG.1C04498/SUPPL_FILE/SC1C04498_ SI_001.PDF.

(185) William L. Jorgensen, *; David S. Maxwell, and; Tirado-Rives, J. Development and Testing of the OPLS All-Atom Force Field on Conformational Energetics and Properties of Organic Liquids. *J. Am. Chem. Soc.* **1996**, *118* (45), 11225–11236. https://doi.org/10.1021/JA9621760.

(186) Bonomi, M.; Bussi, G.; Camilloni, C.; Tribello, G. A.; Banáš, P.; Barducci, A.; Bernetti, M.; Bolhuis, P. G.; Bottaro, S.; Branduardi, D. Promoting Transparency and Reproducibility in Enhanced Molecular Simulations. *Nat. Methods 2019 168* **2019**, *16* (8), 670–673. https://doi.org/10.1038/s41592-019-0506-8.

(187) Kleinschmidt, A. T.; Root, S. E.; Lipomi, D. J. Poly(3-Hexylthiophene) (P3HT): Fruit Fly or Outlier in Organic Solar Cell Research? *J. Mater. Chem. A* **2017**, *5* (23). https://doi.org/10.1039/c6ta08317j.

(188) Reid, D. R.; Jackson, N. E.; Bourque, A. J.; Snyder, C. R.; Jones, R. L.; de Pablo, J. J. Aggregation and Solubility of a Model Conjugated Donor–Acceptor Polymer. *J. Phys. Chem. Lett.* **2018**, *9* (16), 4802–4807. https://doi.org/10.1021/acs.jpclett.8b01738.

(189) Zhang, Z.; Glotzer, S. C. Self-Assembly of Patchy Particles. *Nano Lett.* **2004**, *4* (8), 1407–1413. https://doi.org/10.1021/NL0493500/ASSET/IMAGES/MEDIUM/NL-2004- 093500_0001.GIF.

(190) Martinez, L.; Andrade, R.; Birgin, E. G.; Martínez, J. M. PACKMOL: A Package for Building Initial Configurations for Molecular Dynamics Simulations. *J. Comput. Chem.* **2009**, *30* (13), 2157–2164. https://doi.org/10.1002/JCC.21224.

(191) Jorgensen, W. L.; Tirado-Rives, J. Potential Energy Functions for Atomic-Level

Simulations of Water and Organic and Biomolecular Systems. **2005**.

(192) Dodda, L. S.; Vilseck, J. Z.; Tirado-Rives, J.; Jorgensen, W. L. 1.14∗CM1A-LBCC: Localized Bond-Charge Corrected CM1A Charges for Condensed-Phase Simulations. *J. Phys. Chem. B* **2017**, *121* (15), 3864–3870. https://doi.org/10.1021/ACS.JPCB.7B00272/SUPPL_FILE/JP7B00272_SI_002.XLS.

(193) Dodda, L. S.; De Vaca, I. C.; Tirado-Rives, J.; Jorgensen, W. L. LigParGen Web Server: An Automatic OPLS-AA Parameter Generator for Organic Ligands. *Nucleic Acids Res.* **2017**, *45* (W1), W331–W336. https://doi.org/10.1093/NAR/GKX312.

(194) Salleo, A.; Chen, T. W.; Völkel, A. R.; Wu, Y.; Liu, P.; Ong, B. S.; Street, R. A. Intrinsic Hole Mobility and Trapping in a Regioregular Poly(Thiophene). *Phys. Rev. B - Condens. Matter Mater. Phys.* **2004**, *70* (11), 115311. https://doi.org/10.1103/PHYSREVB.70.115311/FIGURES/8/MEDIUM.

(195) Kline, R. J.; McGehee, M. D. Morphology and Charge Transport in Conjugated Polymers. *https://doi.org/10.1080/15321790500471194* **2007**, *46* (1), 27–45. https://doi.org/10.1080/15321790500471194.

(196) Noriega, R.; Rivnay, J.; Vandewal, K.; Koch, F. P. V; Stingelin, N.; Smith, P.; Toney, M. F.; Salleo, A. A General Relationship between Disorder, Aggregation and Charge Transport in Conjugated Polymers. *Nat. Mater.* **2013**, *12*. https://doi.org/10.1038/NMAT3722.

(197) Bragg, A. E.; Yu, W.; Zhou, J.; Magnanelli, T. Ultrafast Raman Spectroscopy as a Probe of Local Structure and Dynamics in Photoexcited Conjugated Materials. *Journal of Physical Chemistry Letters*. American Chemical Society October 6, 2016, pp 3990–4000. https://doi.org/10.1021/acs.jpclett.6b01060.

(198) Tsoi, W. C.; James, D. T.; Kim, J. S.; Nicholson, P. G.; Murphy, C. E.; Bradley, D. D. C.; Nelson, J.; Kim, J. S. The Nature of In-Plane Skeleton Raman Modes of P3HT and Their Correlation to the Degree of Molecular Order in P3HT:PCBM Blend Thin Films. *J. Am. Chem. Soc.* **2011**, *133* (25), 9834–9843. https://doi.org/10.1021/ja2013104.

(199) Francis, C.; Fazzi, D.; Grimm, S. B.; Paulus, F.; Beck, S.; Hillebrandt, S.; Pucci, A.; Zaumseil, J. Raman Spectroscopy and Microscopy of Electrochemically and Chemically Doped High-Mobility Semiconducting Polymers. *J. Mater. Chem. C* **2017**, *5* (25), 6176–6184. https://doi.org/10.1039/c7tc01277b.

(200) McCulloch, B.; Ho, V.; Hoarfrost, M.; Stanley, C.; Do, C.; Heller, W. T.; Segalman, R. A. Polymer Chain Shape of Poly(3-Alkylthiophenes) in Solution Using Small-Angle Neutron Scattering. *Macromolecules* **2013**, *46* (5), 1899–1907.

https://doi.org/10.1021/ma302463d.

(201) Köhler, A.; Hoffmann, S. T.; Bässler, H. An Order–Disorder Transition in the Conjugated Polymer MEH-PPV. *J. Am. Chem. Soc.* **2012**, *134* (28), 11594–11601. https://doi.org/10.1021/ja302408a.

(202) MacKerell, A. D.; Bashford, D.; Bellott, M.; Dunbrack, R. L.; Evanseck, J. D.; Field, M. J.; Fischer, S.; Gao, J.; Guo, H.; Ha, S. All-Atom Empirical Potential for Molecular Modeling and Dynamics Studies of Proteins. *J. Phys. Chem. B* **1998**, *102* (18), 3586–3616. https://doi.org/10.1021/JP973084F.

(203) Fu, Y.; Bernasconi, L.; Liu, P. Ab Initio Molecular Dynamics Simulations of the SN1/SN2 Mechanistic Continuum in Glycosylation Reactions. *J. Am. Chem. Soc.* **2021**, *143* (3), 1577–1589. https://doi.org/10.1021/JACS.0C12096/SUPPL_FILE/JA0C12096_SI_008.MP4.

(204) Li, W.; Hendriks, K. H.; Wienk, M. M.; Janssen, R. A. J. Diketopyrrolopyrrole Polymers for Organic Solar Cells. *Acc. Chem. Res.* **2016**, *49* (1), 78–85. https://doi.org/10.1021/ACS.ACCOUNTS.5B00334/ASSET/IMAGES/LARGE/AR-2015-00334Q_0008.JPEG.

(205) Woo, C. H.; Beaujuge, P. M.; Holcombe, T. W.; Lee, O. P.; Fréchet, J. M. J. Incorporation of Furan into Low Band-Gap Polymers for Efficient Solar Cells. *J. Am. Chem. Soc.* **2010**, *132* (44), 15547–15549. https://doi.org/10.1021/ja108115y.

(206) Sugiyama, F.; Kleinschmidt, A. T.; Kayser, L. V.; Alkhadra, M. A.; Wan, J. M.-H.; Chiang, A. S.-C.; Rodriquez, D.; Root, S. E.; Savagatrup, S.; Lipomi, D. J. Stretchable and Degradable Semiconducting Block Copolymers. *Macromolecules* **2018**, *51* (15), 5944–5949. https://doi.org/10.1021/acs.macromol.8b00846.

(207) Fauvell, T. J.; Zheng, T.; Jackson, N. E.; Ratner, M. A.; Yu, L.; Chen, L. X. The Photophysical and Morphological Implications of Single-Strand Conjugated Polymer Folding in Solution. *Chem. Mater.* **2016**, *28* (8), 2814–2822. https://doi.org/10.1021/acs.chemmater.6b00734.

(208) Liu, C.; Hu, W.; Jiang, H.; Liu, G.; Han, C. C.; Sirringhaus, H.; Boué, F.; Wang, D. Chain Conformation and Aggregation Structure Formation of a High Charge Mobility DPP-Based Donor-Acceptor Conjugated Polymer. *Macromolecules* **2020**, *53* (19), 8255–8266. https://doi.org/10.1021/ACS.MACROMOL.0C01646/ASSET/IMAGES/LARGE/MA0C01646_0010.JPEG.